UNIVERSITY OF OKLAHOMA

GRADUATE COLLEGE

KINETICS AND SOLVENT EFFECTS ON SUPPORTED METAL CATALYSTS FOR BIOMASS CONVERSION

A DISSERTATION

SUBMITTED TO THE GRADUATE FACULTY

in partial fulfillment of the requirements for the

Degree of

DOCTOR OF PHILOSOPHY

By

ZHENG ZHAO
Norman, Oklahoma
2018

KINETICS AND SOLVENT EFFECTS ON SUPPORTED METAL CATALYSTS FOR BIOMASS CONVERSION

A DISSERTATION APPROVED FOR THE
SCHOOL OF CHEMICAL, BIOLOGICAL AND MATERIALS ENGINEERING

BY

Dr. Daniel E. Resasco, Chair

Dr. Steven P. Crossley

Dr. Lance L. Lobban

Dr. David A. Sabatini

Dr. Bin Wang

With love to my parents Caixia Chen, Chuanfu Zhao and my grandma Aixiang Zhou

Acknowledgements

I would like to express my deepest gratitude to my academic advisor Dr. Daniel Resasco, who has been a major source of inspiration and support, and who pushed me to my potential in achievements. He is someone whom I always wanted to aspire to be. It has been a fruitful adventure to have all my committee members with me, Dr. Resasco, Dr. Wang, Dr. Crossley, Dr. Lobban and Dr. Sabatini. Thank you for brainstorming with me in meetings and giving me advice on life and work.

I'm also grateful for the opportunity to work with excellent colleagues. Your collaboration and assistance deliver precise analysis for my experimental work. With special thanks to Dr. Dachuan Shi, Dr. Tu Pham, Dr. Miguel Gonzalez-Borja, Dr. Lu Zhang, Dr. Nicholas Briggs, Dr. Taiwo Omotoso, Dr. Abhishek Gumidyala for training me on lab equipment, as well as Mr. Gregory Strout at the Samuel Roberts Noble Electron Microscopy Laboratory, Ms. Lisa Whitworth and Mr. Brent Johnson at the Oklahoma State University Microscopy Laboratory who offered great insights on my catalyst samples. I feel extremely fortunate to work with some of the most diligent people I've met: Dr. Qiaohua Tan, Mr. Reda Bababrik and Ms. Tong Mou. Their contributions brought our projects to the next level.

Last but not the least, I would like to extend my gratitude to my friends and family. They are always with me via WeChat and FaceБФФЖ - two greatest social apps in the 2010s - and at Braum's, whose double dip hot fudge sundaes are delicious. Your support and encouragement bring out the best in me.

Table of Contents

Acknowledgements iv

List of Tables ix

List of Figures x

Abstract xv

Chapter 1: Introduction 1

1.1 Biomass Conversion 1

1.2 Liquid Phase Hydrogenation and Aqueous Phase Reforming 5

Chapter 2: Kinetics and Transition State Theory 9

2.1 Langmuir-Hinshelwood Kinetic Model 9

2.2 Statistical Thermodynamics 10

2.3 Transition State Theory 12

2.4 Reactions in Solutions and in Thermodynamically Non-ideal Systems 14

Chapter 3: Solvent Effect 16

3.1 Solvent Effects in Homogeneous and Heterogeneous Catalysis 17

3.2 Solvent Effect on Hydrogenation 21

3.2.1 Solvent effects related to electrical properties 22

3.2.2 Solvent effects related to thermodynamic non-ideality 25

3.2.3 Solvent effects related to solvent hydrogen solubility 26

3.2.4 Solvent effects related to competitive adsorption 31

3.2.5 Solvent effects related to intrinsic kinetics: alcohols and water 35

Chapter 4: Non-ideal Solvent Effect on Kinetics of Cyclohexene Hydrogenation over Pd/α-Al_2O_3 43

4.1 Introduction 43
4.2 Experimental 46
4.2.1 Catalyst synthesis 46
4.2.2 Characterization 46
4.2.3 Catalytic reaction 47
4.3 Results and discussion 49
4.3.1 Pd particle distribution and surface structure 49
4.3.2 Catalyst deactivation and kinetic regime 51
4.3.3 Kinetic models 54
4.3.4 True kinetic model and DFT studies 58
4.3.5 Solvent effect and solvent non-ideality 64
4.3.6 Kinetic and thermodynamic parameters 69
4.4 Conclusion 80
Acknowledgements 82
Chapter 5: Mechanistic Role of Water in Aqueous Phase Furfural Hydrogenation on Pd Catalysts 83
5.1 Introduction 83
5.2 Experimental 86
5.2.1 Catalyst preparation 86
5.2.2 Catalyst characterization 86
5.2.3 Catalyst test 87
5.3 Results and discussion 88
5.3.1 Catalyst characterization 88

5.3.2 Kinetic regime and deactivation test 90
5.3.3 Solvent effect 92
5.3.4 Reaction order and rate determining step 96
5.4 Conclusion 100
Acknowledgements 101
Chapter 6: Aqueous Phase Reforming of Ethanol on Synergistic Bimetallic Ru-Pt Catalysts 102
6.1 Introduction 102
6.2 Experimental 103
6.2.1 Catalyst preparation 103
6.2.2 Catalyst characterization 105
6.2.3 Reaction procedure 105
6.3 Results and discussion 107
6.3.1 Catalysts characterization 107
6.3.2 Reaction pathways 111
6.3.3 Ru particle size effects 116
6.3.4 Pt particle size effects 119
6.3.5 Effect of the support 121
6.3.6 Bimetallic Ru-Pt catalysts 122
6.4 Conclusion 127
Acknowledgements 128
Chapter 7: Summary 129
7.1 Kinetics in hydrogenation 129

7.2 Solvent effect 130

References 132

Appendix 149

A. DFT calculations in Chapter 4 149

A1. DFT calculations 149

A2. Adsorption geometries 150

B. Kinetic fitting effectiveness in Chapter 4 151

C. DFT calculations in Chapter 5 152

D. Isotope study in Chapter 5 153

Appendix References 156

List of Tables

Table 1. Partition functions for different types of motion. (Adapted from [24, 27]).....11

Table 2. Effect of solvent on rate of hydrogenation (N)[a]. (Adapted from [37]).....22

Table 3. Initial rates of AP hydrogenation in solvents and its dielectric constants and electric dipole moments[a]. (Adapted from [39]) 24

Table 4. Turnover frequency (TOF) for hydrogenation of cyclohexene in different solvents over Pt/SiO_2 and Pd/SiO_2. (Adapted from [35, 36]).....27

Table 5. Activity coefficient at infinite dilution. 56

Table 6. Kinetic models and reaction orders. 57

Table 7. Kinetic model fitting parameters. 64

Table 8. DFT calculated adsorption energies of cyclohexene, decalin, methylcyclohexane and heptane without vdw interactions.....64

Table 9. Surface coverage in different solvents[a].....67

Table 10. Kinetic and thermodynamic parameters from experimental fittings. 71

Table 11. Adsorption energy over Pd (111) surface. 96

Table 12. Characterization of Ru series catalysts. 107

Table 13. Liquid phase and gas phase product distribution of APR of ethanol.....112

List of Figures

Figure 1. Diagram of approximate reaction conditions for the catalytic processing of petroleum versus biomass-derived carbohydrates. (Adapted from [22]).....5

Figure 2. Gibbs free energy of reactants in solvent O and solvent S at initial/reactant states and transition states. (Adapted from [31]) 18

Figure 3. Free energy diagram of ionic reactions and effect of solvent when medium was changed from protic to dipolar aprotic. (Adapted from [31]).....19

Figure 4. Initial rate of AP hydrogenation as a function of dielectric constants ($\boldsymbol{\varepsilon}$) and electric dipole moments ($\boldsymbol{\mu}$) in (a) protic solvents, (b) aprotic polar solvents, and (c) apolar solvents. Reaction conditions: initial concentration of AP, 0.168 M; 7.6% Ni/SiO2, 0.5 g; solvent, 150 mL, H_2 pressure, 8.7 bar; temperature, 363 K. (Adapted from [39]).....24

Figure 5. Relationship of surface adsorbed hydrogen and concentration of dissolved hydrogen in solvents. (Adapted from [56, 57]).....30

Figure 6. Acetone hydrogenation of Raney nickel catalyst at 10 °C. ●, in n-hexane; ◓, in cyclohexane; ○, in methyl alcohol; ◑, in isopropyl alcohol; - - -, in water. (Adapted from [51]).....33

Figure 7. Hydrogenation rate as a function of heat of adsorption of solvents. Reaction conditions: T=363 K, P=10 bar, W_{cat}=0.5 g, C_{AP}=0.168 M, $V_{solvent}$=150 mL, stirring speed=700 rpm). (Adapted from [39]) 35

Figure 8. Adsorption geometry of acetone on Ru (0001). (a) without water, (b) water is co-adsorbed. (Adapted from [62]) 37

Figure 9. Reaction coordinate diagrams for CO activation mechanisms over Ru. Intrinsic activation barriers are in italics and effective barriers are in bold. (a) in vacuum, (b) in the presence of water. (Adapted from [53]) 41

Figure 10. DFT-derived structures for water-mediated hydroxymethylidyne route. H atom is highlighted in yellow and distances are in nm. (Adapted from [53]) 42

Figure 11. Parr reactor equipped with ATR-IR probe and the IR spectra of cyclohexene. (Adapted from [76]) 47

Figure 12. (a) TEM image of 0.25 wt.% Pd/a-Al_2O_3. (b) Histogram of Pd particles size distribution. (c) HRTEM image of Pd particles. 50

Figure 13. Deactivation study on 0.25 wt.% Pd/a-Al_2O_3. Reaction conditions: solvent heptane, H_2 pressure 560 psi, temperature 70 °C, cyclohexene initial concentration 0.42 M. 52

Figure 14. External mass transfer test. Reaction conditions: solvent heptane, H_2 pressure 560 psi, temperature 70 °C, cyclohexene initial concentration 0.42 M. 53

Figure 15. Hydrogenation as a function of H_2 pressure in three solvents fitted with the third scenario where hydrogen and reactant adsorb on different sites and the RDS is the first hydrogenation. Reaction conditions: temperature 70 °C, cyclohexene initial concentration 0.42 M. 59

Figure 16. Hydrogenation as a function of cyclohexene concentration in three solvents fitted with the third scenario where hydrogen and reactant adsorb on different sites and the RDS is the first hydrogenation. Reaction conditions: temperature 70 °C, H_2 pressure 560 psi. 59

Figure 17. DFT calculated potential energy diagram for the hydrogenation of cyclohexene on clean Pd (111). 63

Figure 18. Hydrogenation in co-solvent mixtures. Reaction conditions: temperature 70 °C, H_2 pressure 560 psi, cyclohexene initial concentration 0.42 M. 65

Figure 19. (a) Entropy of cyclohexene in liquid phase and on surface combined with scenarios at different translational lengths and rotational DOF, with experimental data. (b) Entropy of adsorption as a function of translational length and rotational DOF. The solid line is the value from kinetic fitting. 75

Figure 20. Entropy of hydrogen in gas phase and on surface combined with scenarios at possible translational lengths with experimental data. 77

Figure 21. EDX images and elements spectra of (A) 1% Pd/α-Al_2O_3. (B) 3% Pd/α-Al_2O_3 89

Figure 22. (A) TEM images of 3% Pd/α-Al_2O_3. (B) Pd particle diameter histogram. ... 89

Figure 23. External mass transport test at different stirring rate in water. Reaction conditions: initial concentration of FAL is 0.1M, T=40°C, P=800psi, catalyst amount=100mg 3%Pd/α-Al2O3, reaction time=0.8h. 90

Figure 24. Catalyst deactivation test with different reaction times in water. Reaction conditions: initial concentration of FAL is 0.1M T = 40°C, P = 5.52 MPa, catalyst amount = 250 mg 3%Pd/α-Al_2O_3. 92

Figure 25. FAL hydrogenation conversion and products yields in different solvents. Reaction conditions: initial concentration of FAL is 0.1M, T=40°C, P=800psi, catalyst amount=250mg 3%Pd/α-Al_2O_3, reaction time=0.8h 93

Figure 26. DFT calculations of hydrogenation of furfural. (A) Schematic reaction path in the vapor phase. (B) Reaction path in the liquid water with proton shuttling hydrogenation. (C) Calculated energy profile of the hydrogenation path on Pd in the gas phase and in liquid water. 95

Figure 27. Reaction order as respective of H_2 pressure in water and cyclohexane. Initial concentration of FAL is 0.1M, T=40°C. 99

Figure 28. TEM images (i) and particle diameter distribution (ii) of the different catalysts; (a) 5% Ru/C; (b) 0.5% Ru/C; c) 2.6% Ru/TiO_2 ; (d) 0.5% Ru/TiO_2; (e) 1% Pt/C; (f) 2% Pt/TiO_2 and (g) 1% Ru-2% Pt/TiO_2 110

Figure 29. Liquid product distribution of 0.5% Ru/TiO_2 catalysts as a function of reaction time. Reaction conditions: 200 mg of catalyst, 250 °C 200 psi of Ar; Feed: 15 vol.% ethanol aqueous solution with overall volume of 100 mL. 113

Figure 30. Gas phase product distribution over different Ru catalysts. Reaction conditions: 250 °C 200 psi of Ar; Feed: 15 vol% ethanol aqueous solution with overall volume of 100 mL 117

Figure 31. Gas phase product distribution over different Pt catalysts. Reaction conditions: 250 °C 200 psi of Ar; Feed: 15 vol% ethanol aqueous solution with overall volume of 100 mL. 120

Figure 32. XRD patterns for pre-reduced 2 %Pt-1 %Ru/TiO_2 as line ‘a’; 2 %Pt/TiO_2 as line ‘b’; 1 %Ru/TiO_2 as line ‘c’. The line ‘d’ shows the difference in intensity between 2 %Pt-1 %Ru/TiO_2 and 1 %Ru/TiO_2; the line ‘e’ shows the difference in intensity between 2%Pt/TiO_2 and 1%Ru/TiO_2; whereas the line ‘f’ shows the difference in intensity between 2 %Pt - 1 %Ru/TiO_2 and 2 %Pt/TiO_2 124

Figure 33. Gas phase product distribution over different Pt-Ru bimetallic catalysts. Reaction conditions: 250 °C 200 psi of Ar; Feed: 15 vol% ethanol aqueous solution with overall volume of 100 mL..... 125

Figure 34. Assessment of catalyst performances based on two desirable ratios: vertical: COx-to-C2 ratio, which indicates the catalyst efficiency for C-C cleavage; horizontal: overall H_2 production rate. The optimal catalysts should appear on the upper right corner of the diagram. 126

Abstract

Energy conversion using renewable biomass has significant environmental impact. To acquire high value products using preliminary processed biomass, considerable amount of upgrading reactions has been conducted in liquid-phase conditions. Addition of solvents could interact with all component within reaction system. In order to influence heterogeneous catalytic reactions, solvents have to affect the kinetically relevant steps such as adsorption, surface reaction, and desorption. The following chapters investigate kinetics and solvent effects for biomass conversion.

In Chapter 4, cyclohexene hydrogenation has been carried out over 0.25 wt.% Pd/α-Al_2O_3 in heptane, methylcyclohexane and decalin with a wide range of reaction conditions, from 30 psi to 600 psi of hydrogen pressure under 40 °C – 100 °C. Those inert solvents demonstrate competitive adsorption with reactants cyclohexene and lead to its decrease in surface coverage. Decalin competes the strongest and results the lowest hydrogenation rate followed by methylcyclohexane and then heptane. Heptane illustrates negligible surface competitive adsorption. Additionally, the non-ideality of reaction mixtures also alters the surface concentration of the solvent molecules compared to the bulk phase. Four kinetic models have been established based on different surface scenarios, and the cyclohexene hydrogenation has been found to be the first hydrogenation as the rate-determining step with cyclohexene and hydrogen absorbed on different Pd sites. Combined with statistical thermodynamic analysis, surface cyclohexene and hydrogen retain a certain amount of entropy based on their degree of freedom(DOF) of translation, rotation and vibration modes. ΔS_{ads} for cyclohexene is -143 ± 19 J/mol·K, which loses around 2/3 of total entropy of its liquid state. Hydrogen losses more entropy upon adsorption and ΔS_{ads} is -

108 ± 12 J/mol·K. Meanwhile, heat of adsorption decreases with surface coverage. ΔH_{ads} for cyclohexene on a clean Pd surface is -75 ± 14 kJ/mol, while the ΔH_{ads} for hydrogen is -41 ± 7 kJ/mol. On a fully covered Pd surface, ΔH_{ads} for cyclohexene becomes -53 kJ/mol, while ΔH_{ads} for hydrogen reduces to -33 kJ/mol.

In Chapter 5, the protic solvent, water, participates in the kinetically relevant step, surface reaction step, and influences the reaction rate and product distributions. Furfural hydrogenation in cyclohexane and water over 3% Pd/α-Al_2O_3 presents distinctive reactivity and product distribution. In the presence of water, hydrogenation of the carbonyl group of furfural is favored and therefore furfuryl alcohol is the main product. While the furanyl ring hydrogenation is favored in solvent cyclohexane and the reactivity in cyclohexane is much less. DFT calculations demonstrate that water stabilizes the intermediate and final product significantly by forming hydrogen bonds and provides an alternative hydrogenation pathway through water H-shuttling mechanism. Water-assist hydrogenation decreases the overall energy at the transition state from 46 kJ/mol to -7 kJ/mol. Kinetic studies in water and cyclohexane further unveil that reaction orders with respect of H_2 pressure also differ. 0.8^{th} order has been found when using water, which indicates the second hydrogenation step is the rate-determining step. 0.3^{th} order in cyclohexane manifests the first hydrogenation step is the rate-determining step. The kinetic results are consistent with DFT calculations. When water shuttles the surface H proton to the oxygen of the carbonyl group through the H-bonding networks, the energy at the transition state for this step decreases from 46 kJ/mol to -16 kJ/mol, making the second hydrogenation of the carbon the rate-determining step.

In Chapter 6, water serves as a solvent and the critical reactant that converts surface species to desired products. Aqueous phase reforming (APR) of ethanol over various Pt and Ru catalysts have been carried out in ethanol water mixture. Upon adsorption, ethanol decomposes by sequential dehydrogenation starting from Cα followed by dehydrogenation on Cβ until surface ketene CH_2CO species are achieved. The C-C cleavage happens afterwards and surface CO species then react with water to produce more H_2 and CO_2 through the water-gas-shift (WGS) reaction. The presence of water drives the equilibrium of WGS reaction and removes the surface CO species. Therefore, negligible amount of CO has been detected in products. Serious Ru catalysts with different particle sizes have also been explored. Ru tends to favor the C-C cleavage compared to Pt. However, smaller Ru particles present strong adsorption of surface CO species and cause site poisoning. Larger Ru particles greatly favors the methanation reaction that consumes H_2 in the product and CO, CO_2 to form CH_4. To optimize the catalyst, achieve desired product H_2 and inhibit CH_4 production, bimetallic Ru-Pt catalysts have been investigated. The co-impregnated 1%Ru-2%Pt/TiO_2 displays the synergistic performance, with increased reaction rate for H_2 production but lower rate for CH_4.

Chapter 1: Introduction

1.1 Biomass Conversion

Conversion from renewable biomass to fuel and chemicals has significant impact on productions that mainly rely on non-renewable carbon sources, petroleum and coal. Compared with petrochemical refinery, CO_2 emissions from biomass combustion are carbon (C) flux neutral since it can be captured by biomass regrowth[1, 2]. For energy production using biomass, feedstocks such as switchgrass, agricultural residues, municipal wastes and woody crops are widely employed for the reason that they contain lignocellulose, which is the most abundant class of biomass and is made up of hemicellulose, cellulose and lignin[3].

General strategies of converting lignocellulosic biomass are going through thermochemical and hydrolysis[3-6].

In thermochemical route, treatments including gasification and pyrolysis depolymerize lignocellulosic biomass in order to extract all carbon (C)-containing biomass components[7, 8]. Syngas, mainly H_2 and CO, is produced via gasification under temperatures over 727 °C and is brought into the production of gasoline or diesel under Fischer-Tropsch synthesis (FTS). Other crucial chemical processes are derived from syngas such as H_2 production through water gas shift reaction and methanol production from methanol synthesis. Pyrolysis is conducted at temperatures between 400 – 600 °C for few seconds in the absence of oxygen. The vapor generated during pyrolysis is then condensed to yield a liquid mixture known as bio-oil. However, the resulting bio-oil has a broad range of chemicals including water, acids, aldehydes, alcohols, sugars, ketones,

esters, etc.[4]. A staged thermal fractionation, torrefaction followed by pyrolysis, has been proposed to produce compositional purified and categorized intermediates based on different temperature ranges that each composition of lignocellulose decomposes[9-11]. Hemicellulose decomposes at low temperature, torrefaction conditions, ranging from 250 – 275 °C. The products from this stage are light oxygenates including acetic acid, furfural and water. About 58.5 wt.% liquid product is water[12, 13]. The second stage decomposes cellulose at 300 – 400 °C yielding sugar derived compounds. levoglucosan takes up the majority from this stage. Last but not the least, lignin derived compounds as phenolics are the products as the result of fast pyrolysis in between 500 - 600 °C. The staged thermal fractionation separates the major compounds within the lignocellulosic biomass.

Hydrolysis deconstructs solid biomass via aqueous phase acid-catalyzed reaction to isolate sugar monomers from the lignocellulose fibers, which are formed by hydrogen bonding[5]. Strong inorganic acid as HCl or H_2SO_4 are able to depolymerize hemicellulose and cellulose readily in aqueous environment. Cellulose hydrolysis to simple sugar glucose, which can be further degraded. 5-hydroxymethylfurfural and levulinic acid are the byproducts of cellulose hydrolysis and serve as important building blocks for fuel additives[4]. Combining with catalytic reactions, hydrogenation of sugar monomers produces polyols such as sorbitol, xylitol and dehydration of the monomers obtains furfural and hydroxymethylfurfural. Another approach followed by the hydrolysis utilizes fermentation to produce bio-ethanol, although this biological process takes much longer time compared with other processes mentioned above[3].

No matter applying thermochemical or hydrolysis route to extract all carbon (C)-containing biomass components, primary products produced are unstable, highly reactive

and oxygenated compounds. Therefore, catalytic upgrading is desired to produce value-added chemical intermediates or fuel additives[3, 14, 15].

Upgrading strategies have been investigated based on functionality of compounds. Carbon-carbon coupling takes place to couple species with light hydrocarbons with low carbon number into high carbon number that falls into the fuel-range products. Ketonization, aldol condensation, alkylation, hydroxyalkylation and acylation are the key reactions for carbon-carbon coupling. The general chemistries are presented in Scheme 1. Carboxylic acids are coupled through ketonization reaction[16]. However, CO_2 is released as the byproduct. Aldol condensation, on the other hand, couples two carbonyl compounds to form a ketone without losing any carbon sources[17]. Coupling aromatic and furan compounds with alcohols, carboxylic acids and ketones are alkylation, acylation and hydroxyl alkylation respectively.

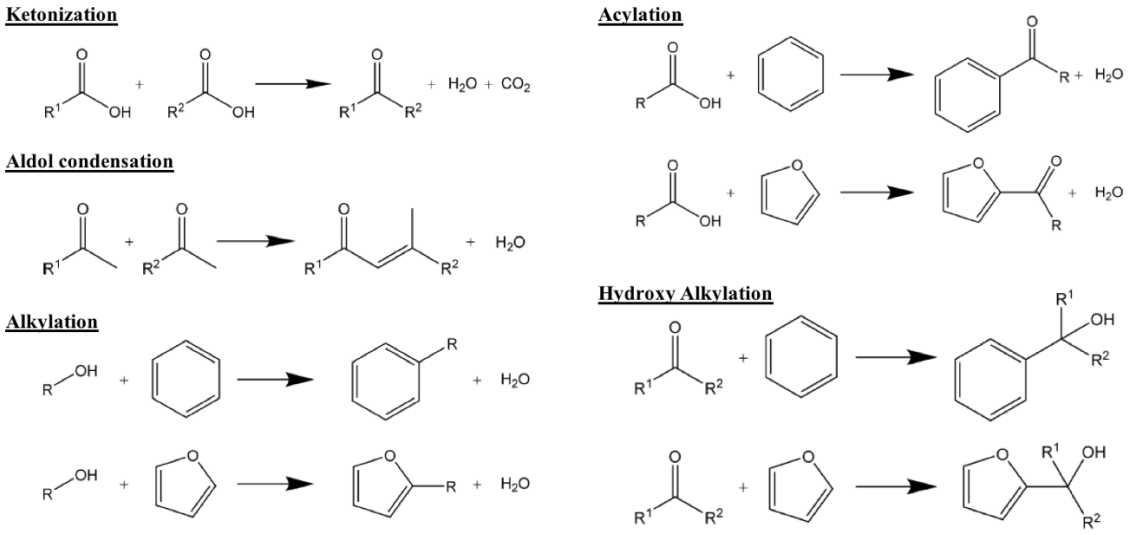

Scheme 1. General chemistries for carbon-carbon coupling (Adapted from [14])

Hydrodeoxygenation (HDO) is another important upgrading strategies for biomass conversion after carbon-carbon coupling. Oxygenated compounds lead to low thermal

stability, low energy content and highly corrosive. Removal of oxygen is necessary to stabilize bio oil. Typical HDO reactions usually contain: (1) hydrogenation of the unsaturated C=O bonds to C-OH, (2) dehydration of the hydroxyl groups, (3) cleavage of C-C bonds, and (4) hydrogenolysis of C-O-C bonds[18, 19].

Aqueous phase reforming (APR) of oxygenated hydrocarbons provide an alternative route for syngas production, which conventionally is carried out via gasification under high temperature over 727 °C. APR of oxygenated compounds produces H_2 and CO in a single-step catalytic processes at moderate temperatures ranging from 200 – 260 °C[20, 21]. Water not only serves as the solvent but more importantly reacts with CO through water gas shift reaction to produce CO_2 and H_2, driving the conversion forward. Tailoring the APR of sorbitol, longer carbon number alkanes consisting primarily of butane, pentane and hexane are achieved besides H_2 and CO_2.

Overall, due to various functionalities of primary biomass products such as low volatility and high reactivity, feeds are typically processed in liquid phase reactions[22]. As shown in Figure 1, most of biomass-derived carbohydrates go through reactions such as hydrogenation, hydrolysis, aldol condensation and reforming in an aqueous, an organic or biphasic condition at mild temperatures. For comparison, petrochemical processes usually require much higher temperature and are conducted in vapor phase. Similarly, thermochemical processes such as pyrolysis and gasification are also conducted in vapor phase. It’s crucial to understand kinetics of reactions along with the role of solvent during reactions.

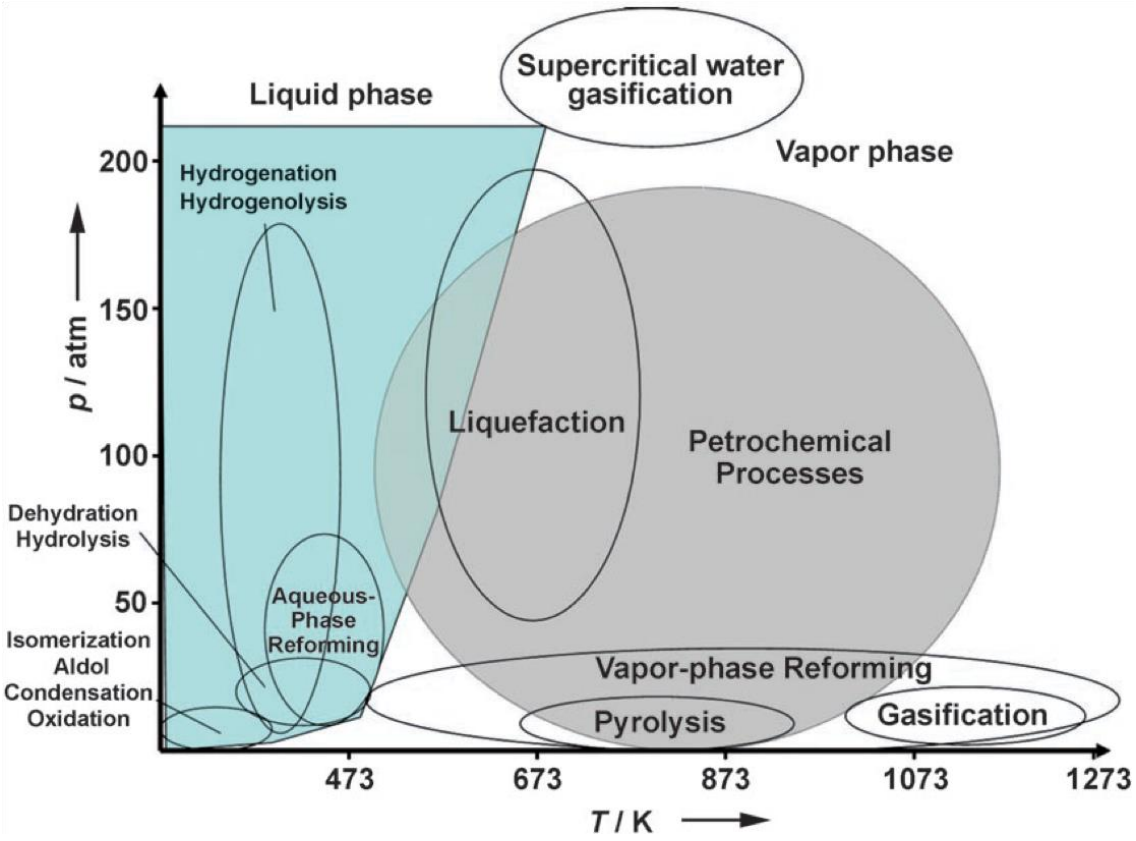

Figure 1. Diagram of approximate reaction conditions for the catalytic processing of petroleum versus biomass-derived carbohydrates. (Adapted from [22])

1.2 Liquid Phase Hydrogenation and Aqueous Phase Reforming

Heterogeneous catalytic conversion has been widely considered for processing of petroleum and biomass since they fulfill easy product separation and catalyst reusability over homogenous catalytic processes. Among upgrading strategies summarized in 1.1, hydrogenation reactions as an important type of reaction are required to saturate the alkene, carbonyl and ketone groups after carbon-carbon coupling and during HDO process. Besides being widely considered in biomass conversion, hydrogenation is crucial reactions in chemical, pharmaceutical and food industry.

Group VIII metals including iron Fe, cobalt Co, nickel Ni, platinum Pt, ruthenium Ru, rhodium Ph, palladium Pd, osmium Os and iridium Ir, as well as copper Cu, gold Au

and tungsten W have demonstrated hydrogenation ability towards unsaturated hydrocarbons[23]. The reaction mechanisms and kinetic models for hydrogenation are also well developed and are discussed in Chapter 2: Kinetics and Transition State Theory. Combining with theoretical calculations, the energy profiles within hydrogenation on a metal surface for each species are obtained with significant insights.

However, experimental data and first-principles predictions are not always consistent with each other. There are many aspects that attribute to the discrepancy. Therefore, one of objectives of the study is to present a large and diversified set of data to have a mechanistic understanding towards hydrogenation. Moreover, reliable theoretical and experimental methodologies are necessary to explore and provide reasonable boundaries for first-principle calculations. Performing microkientcs study is one approach to model surface reactions, derive parameters and attach physical meanings to it. By analyzing those parameters such as entropy of adsorption, enthalpy of adsorption, entropy of reaction and enthalpy of reaction, energy profiles of surface reacting species are constructed. Those parameters serve as core elements to predict reaction kinetics such as rate constants and equilibrium constants. Nevertheless, merely few systematic studies, especially for entropy change, are developed to correlate those parameters to metal surface properties through experiment approaches. The statistical thermodynamics analysis has been involved to provide reasonable estimations on entropy of adsorption for cyclohexene and hydrogen molecules presented in Chapter 4: Non-ideal Solvent Effect on Kinetics of Cyclohexene Hydrogenation over Pd/α-Al_2O_3. Incorporated with DFT calculations, the heat of adsorption is discussed as a function of surface coverage.

Meanwhile, when reactions are carried out in solutions, solvent molecules could add a degree of uncertainty towards reactivity, although liquid phase reaction delivers great benefits such as dissolve reactants and products, rapid heat transfer for exothermic reactions. The effect of solvent has been well studied in homogeneous catalysis. In heterogeneous catalysis, the solvent effect is starting to be understood. The proposed solvent effects are summarized in Chapter 3: Solvent Effect.

To gain more insights on liquid phase reactions, biomass derived compounds have been utilized since they reflect large variety of organic compounds such as alcohols, aldehydes, acids, aromatics, furanics, unsaturated hydrocarbons, etc. Liquid phase hydrogenation of cyclohexene, furfural and ethanol reforming were carried out as representations for biomass derived aromatics, furanics and alcohols. The corresponding discussions are in Chapter 4: Non-ideal Solvent Effect on Kinetics of Cyclohexene Hydrogenation over Pd/α-Al_2O_3, Chapter 5: Mechanistic Role of Water in Aqueous Phase Furfural Hydrogenation on Pd Catalysts and Chapter 6: Aqueous Phase Reforming of Ethanol on Synergistic Bimetallic Ru-Pt Catalysts. The effect of organic aprotic solvents has been investigated using Langmuir-Hinshelwood kinetic models in hydrogenation of cyclohexene. The competitive adsorption of solvents significantly affects the surface coverage of reactants and the non-ideality of reaction solution have been demonstrated to influence surface and reaction rate at the same time. Moreover, water plays a crucial role during reactions. The effect of water on reactions are carried out in hydrogenation of furfural and ethanol reforming. Water has been manifested to participate the reaction activation of furfural hydrogenation to furfuryl alcohol and decreases the activation energy barrier through H-shuttling. In the ethanol reforming, water reacts with surface species so

that the deactivation has been minimized, along with driving the reaction equilibrium to produce more H_2 through water gas shift reaction. The design of catalysts has been demonstrated to be essential for this reaction. Optimized catalysts have been illustrated to posse efficient C-C cleavage but also low activity towards methanation.

Chapter 2: Kinetics and Transition State Theory

Reaction kinetic relates the microscopic reactions to macroscopic measurables such as concentration, pressure and temperature. Reaction mechanisms demonstrate the interactions of reactants, intermediates and products on catalyst active sites and can be described using mathematical models. Heterogeneous catalysis involves elementary steps as reactant adsorption, surface reaction and product desorption.

2.1 Langmuir-Hinshelwood Kinetic Model

Langmuir-Hinshelwood mechanism combines associative/dissociative adsorption and surface reaction into one rate expression. A typical catalytic reaction between A and B according to Langmuir-Hinshelwood mechanism are[24]

1. $A + * \overset{K_A}{\Leftrightarrow} A*$ (1)

2. $B + * \overset{K_B}{\Leftrightarrow} B*$ (2)

3. $\mathrm{A}* + B* \overset{K_{AB*}}{\Longleftrightarrow} AB*$ (3)

4. $AB* \overset{K_{AB}}{\Longleftrightarrow} AB + *$ (4)

Where * is the active sites, K_i is the equilibrium constants. When each step is in equilibrium, the equilibrium constants are written as the surface coverage of surface species as

$$K_A = \frac{\theta_{A*}}{\theta_v P_A} \quad (5)$$

$$K_B = \frac{\theta_{B*}}{\theta_v P_B} \quad (6)$$

$$K_{AB*} = \frac{\theta_{AB*}}{\theta_{A*}\theta_{B*}} \quad (7)$$

$$K_{AB} = \frac{\theta_v P_{AB}}{\theta_{AB*}} \tag{8}$$

Where θ_v is the empty sites. The overall sites balance during catalytic reaction is constant and the sum of coverages is 1 as

$$\theta_v + \theta_{A*} + \theta_{B*} + \theta_{AB*} = 1 \tag{9}$$

Among these elementary steps, only one step serves as the irreversible rate-determining step (RDS) while others are quasi-equilibrated. If the surface reaction in Eq. (3) is the RDS with a rate constant k_{AB}, the rate can be expressed as

$$r = r_{AB*} = k_{AB}\theta_{A*}\theta_{B*} \tag{10}$$

Since the surface coverage of θ_{A*} and θ_{B*} are derived from Eq. (5) and (6), and θ_v are substituted with site balance in Eq. (9), the rate expression is obtained as

$$r = r_{AB*} = \frac{k_{AB}K_A P_A K_B P_B}{(1 + K_A P_A + K_B P_B + K_{AB}^{-1} P_{AB})^2} \tag{11}$$

The further simplification assumes initial reaction rate that product AB on the surface at the beginning of reaction is low so that the P_{AB} is approximate to 0:

$$r = r_{AB*} = \frac{k_{AB}K_A P_A K_B P_B}{(1 + K_A P_A + K_B P_B)^2} \tag{12}$$

2.2 Statistical Thermodynamics

Statistical thermodynamics links the microscopic properties of matter to its bulk properties such as chemical potential, internal energy, pressure and entropy[25]. Rate constants k_i and equilibrium constants K_i in elementary reaction steps are readily to be computed using partition functions. The partition function is a thermodynamic function of state which contains all properties of the system[24-26]. A particle, a molecule or atom, contains different degrees of freedom(DOF) and its energy is the sum of all energies

associated with these degrees of freedom. Therefore the partition function for molecules is written as

$$Q_i''' = q_t q_r q_v q_e q_n \tag{13}$$

Where q_t represents the partition function for translational degrees of freedom (DOF), and q_r, q_v are the partition functions for rotational and vibrational degrees of freedom (DOF) respectively. q_e and q_n describe electronic partition function and nuclear partition function, although the values are often unity. The partition function for atoms only contains q_t, q_e and q_n since atoms don't possess internal degrees of freedom (DOF) related to rotations and vibrations. The expressions for individual partition functions are listed in Table 1.

Table 1. Partition functions for different types of motion. (Adapted from [24, 27])

Motion	DOF	Partition function
Translation	3	$q_t = V\frac{(2\pi m k_B T)^{3/2}}{h^3}$
Rotation (linear molecule)	2	$q_r = \frac{8\pi^2 I k_B T}{\sigma h^2}$
Rotation (nonlinear molecule)	3	$q_r = \frac{1}{\sigma}(\frac{8\pi^2 k_B T}{h^2})^{3/2}\sqrt{\pi I_A I_B I_C}$
Vibration (per normal mode)	1	$q_v = \frac{1}{1-e^{-h\nu/k_B T}}$

Where m = mass of a particle

I = moment of inertia for linear molecule

I_A, I_B, and I_C = moments of inertia for a nonlinear molecule about three axes perpendicular to each other

ν = normal mode vibrational frequency

k_B = Boltzmann constant

h = Planck constant

T = absolute temperature

σ = symmetry number

The equilibrium constant is determined directly from partition functions of the species participating in a reaction as

$$aA + bB \leftrightarrow cC + dD \tag{14}$$

is given by

$$K = \left\{\prod (\frac{q}{N_A})^{c+d-a-b}\right\} e^{-\Delta_r E/k_B T} \tag{15}$$

Where $\Delta_r E$ is the difference in molar energies of the products and reactants. Meanwhile, the equilibrium constant of a reaction is related to the Gibbs energy of reaction by

$$\Delta_r G = -RTlnK \tag{16}$$

The reaction entropy, $\Delta_r S$, and enthalpy change, $\Delta_r H$, contribute to the reaction Gibbs energy change. Therefore, the partition function term in Eq. (15) is related to the entropy change of products and reactants as

$$\left\{\prod (\frac{q}{N_A})^{c+d-a-b}\right\} = e^{-\Delta_r S/k_B} \tag{17}$$

2.3 Transition State Theory

Reactions, such as when the RDS is Step. 3, proceed by forming an activation complex $AB^{\ddagger}$ at the transition state, which possesses the highest energy between reactants and products. However before product formation, the activated complex is in equilibrium with the initial species. The single vibration of the activated complex yields the product AB. Crossing the energy barrier is a forward only reaction, and the scheme is presented as follows[24, 26, 27]:

$$\mathrm{A} + B \overset{K_{AB^{\ddagger}}}{\Longleftrightarrow} AB^{\ddagger} \overset{k_{TST}}{\longrightarrow} AB \tag{18}$$

Where the equilibrium constant is

$$K_{AB^{\ddagger}} = \frac{n_{AB^{\ddagger}}}{n_A n_B} \tag{19}$$

Therefore, the transition state theory reaction rate is defined as

$$r = \frac{k_B T}{h} n_{AB^{\ddagger}} = \frac{k_B T}{h} K_{AB^{\ddagger}} n_A n_B \tag{20}$$

Where $\frac{k_B T}{h}$ is referred to as universal frequency factor. The macroscopic transition state theory is obtained by using standard entropy, $\Delta S^{0\ddagger}$, and enthalpy, $\Delta H^{0\ddagger}$, associated with the formation of activated complex $AB^{\ddagger}$ from reactant A and B as

$$r = \frac{k_B T}{h} \exp\left(\frac{\Delta S^{0\ddagger}}{k_B}\right) \exp\left(\frac{-\Delta H^{0\ddagger}}{k_B T}\right) n_A n_B \tag{21}$$

Meanwhile, the microscopic transition state theory is derived using molecular partition functions, Q_i''', which is the product of partition functions from translational (q_t), rotational (q_r) and vibrational (q_v) partition functions in Eq.(14). Therefore, the entropy term for the equilibrium between initial states and transition states, $\exp\left(\frac{\Delta S^{0\ddagger}}{k_B}\right)$, is expressed with partition functions. The expression turns into

$$r = \frac{k_B T}{h} \frac{Q'''_{AB^{\ddagger}}}{Q'''_A Q'''_B} \exp\left(\frac{-\Delta E^{0\ddagger}}{k_B T}\right) n_A n_B \tag{22}$$

Where $\Delta E^{0\ddagger}$ is the change in energy at absolute zero temperature associated with the formation of activated complex $AB^{\ddagger}$ from reactant A and B. The corresponding rate constant is

$$k_{TST} = \frac{k_B T}{h} \frac{Q'''_{AB^{\ddagger}}}{Q'''_A Q'''_B} \exp\left(\frac{-\Delta E^{0\ddagger}}{k_B T}\right) = A \exp\left(\frac{-\Delta E^{0\ddagger}}{k_B T}\right) \tag{23}$$

Where A is the pre-exponential factor when it is expressed in Arrhenius form.

2.4 Reactions in Solutions and in Thermodynamically Non-ideal Systems

When reactions are carried out in solutions, rate is proportional to concentration of transition states. Eq. (20) is rewritten in the form as

$$r = \frac{k_B T}{h} C_{AB^{\ddagger}} \tag{24}$$

Which the concentration of transition states is considered as a normal molecule except that all other degrees of freedom along the reaction coordinate including translations, rotations and most vibrations are omitted from the description of this molecule[28].

Solution mixture creates non-ideality so that the equilibrium constant in Eq. (19) should be expressed as

$$K_{AB^{\ddagger}} = \frac{a_{AB^{\ddagger}}}{a_A a_B} \tag{25}$$

Where a_i is the activity, and the activity coefficient γ_i is account for deviations from ideal solution. Therefore Eq. (25) turns into

$$K_{AB^{\ddagger}} = \frac{\gamma_{AB^{\ddagger}}}{\gamma_A \gamma_B} \frac{C_{AB^{\ddagger}}}{C_A C_B} \tag{26}$$

The transition state rate expression in Eq.(24) under non-ideality becomes

$$r = \frac{k_B T}{h} K_{AB^{\ddagger}} \frac{\gamma_A \gamma_B}{\gamma_{AB^{\ddagger}}} C_A C_B \tag{27}$$

The activity coefficients for reactants are readily to be obtained, however it is difficult to acquire a proper value for activity coefficients at transition states. The simplification has been made to neglect the non-ideality at the transition states, although this assumption would have led to drifts of rate constant as the extent of reaction increases[28]. Liquid phase reaction solubilizes reactants, transition states and products. The solvation of those species could affect the reaction kinetics by increasing concentration of surface reacting

species as well as influencing their activity coefficients. the corresponding discussions of the solvent effect are provided in 3.2.2 Solvent effects related to thermodynamic non-ideality and 3.2.3 Solvent effects related to solvent hydrogen solubility.

Chapter 3: Solvent Effect

Conducting catalytic reactions in liquid phase has great advantages including but not limited to dissolving chemicals and transferring heat. The observed differences in product distributions, rate enhancement when applying various solvents is solvent effect[29].

As media, solvents provide an additional degree of freedom to engineer reactions. Crossley et al.[30] achieved simultaneous reaction and product separation by carrying out reactions in Pd/CNT stabilized water-in-decalin emulsions. The schematic illustration of biomass derived vanillin (4-hydroxy-3-methoxybenzaldehyde) conversion is presented in Scheme 2. At 100 °C, water soluble vanillin was hydrogenated over Pd to form water soluble vanillin alcohol, which further hydrogenolysis product was *p*-creosol (2-methoxy-4-methylphenol). Since both vanillin and vanillin alcohol were water soluble, but *p*-creosol had low solubility in water. *p*-creosol migrated from aqueous phase into oil phase upon formation without being further converted. Guaiacol was a product formed at 250 °C through decarbonylation reaction and transferred to decalin phase due to its low solubility in aqueous phase.

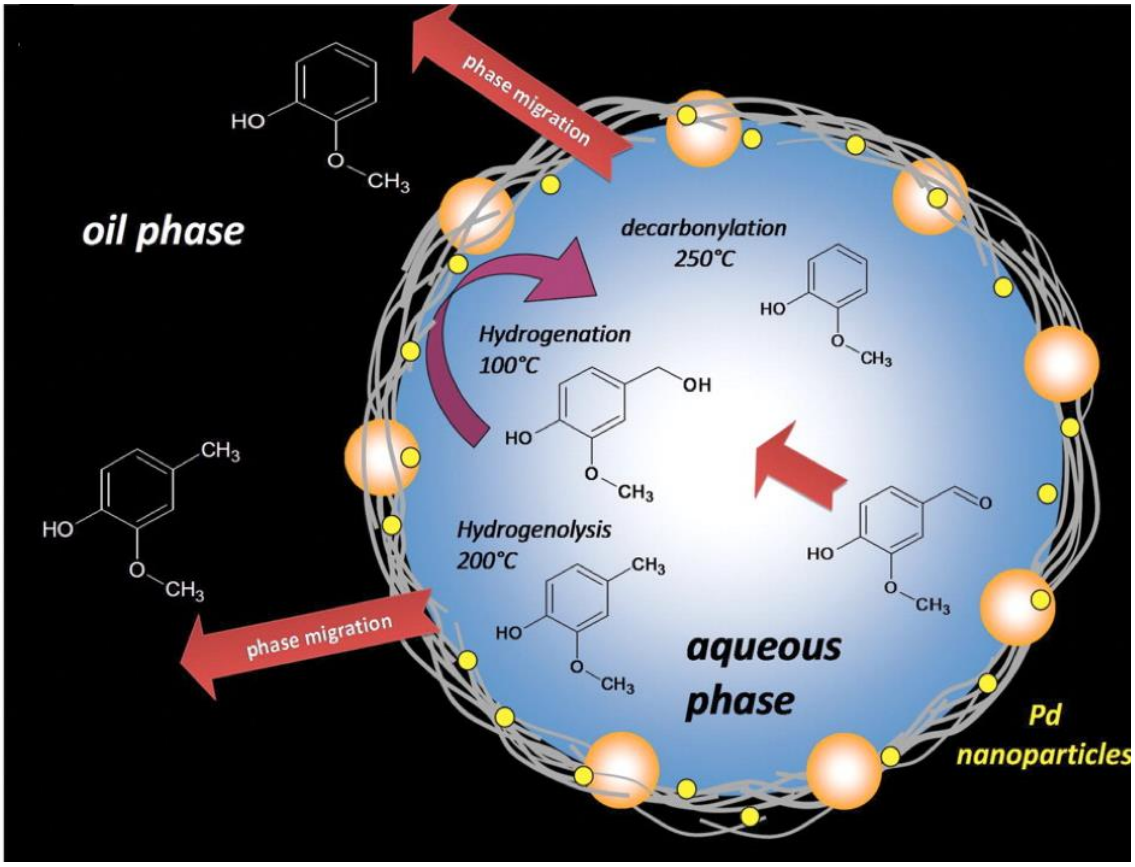

Scheme 2. Simultaneous reaction and product separation using water-oil emulsion. Depending on reaction temperatures, vanillin went through hydrogenation, hydrogenolysis and decarbonylation. Intermediates transferred to different media according to its solubility. (Adapted from [30])

3.1 Solvent Effects in Homogeneous and Heterogeneous Catalysis

To understand effect of solvents on hydrogenation reactions, interactions of solvents with solutes, catalyst surfaces and other solvents are to investigated.

In homogeneous catalysis, catalysts solvate in solvents and interact strongly with reactants and solvents inside the same phase. Buncel et al.[31] and Reichardt et al.[29] explained solvent effect by thermodynamic transfer functions. Solvents could affect initial states and transition states separately. As depicted in Figure 2, the energy diagram of

reactants in solvent O and solvent S at initial states and transition states may have different free energy.

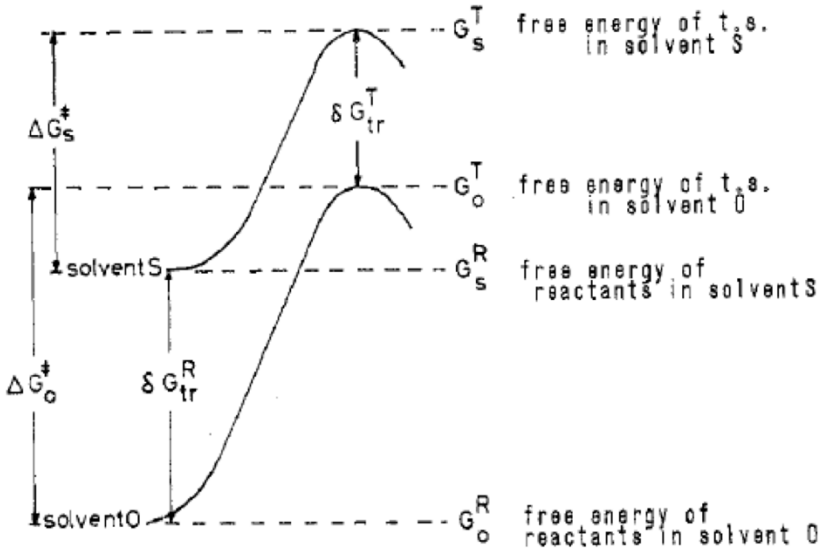

Figure 2. Gibbs free energy of reactants in solvent O and solvent S at initial/reactant states and transition states. (Adapted from [31])

The free energy of activation of *R* at initial/reactant states and *T* at transition states in solvent O and solvent S was expressed by thermodynamic transfer functions as follows:

$$\Delta G_O^{\ddagger} = G_O^T - G_O^R \tag{28}$$

$$\Delta G_S^{\ddagger} = G_S^T - G_S^R \tag{29}$$

The free energy difference at transition states in two solvents was defined as δG_{tr}^T:

$$\delta G_{tr}^T = \delta G_{tr}^R + \Delta G_S^{\ddagger} - \Delta G_O^{\ddagger} = \delta G_{tr}^R + \delta G^{\ddagger} \tag{30}$$

Where δG_{tr}^R was the transfer free energies, which represented the free energy difference at the initial/reactant states. $\delta G^{\ddagger}$ was the kinetic activation parameter. Both δG_{tr}^T, δG_{tr}^R terms can be positive, negative or zero. Given that δG_{tr}^T, δG_{tr}^R had the same sign, it was referred to a balancing situation where rate differences in two solvents were the smallest. On the other hand, when δG_{tr}^T, δG_{tr}^R showed opposite signs, it was referred to a reinforcing

situation and the rate differences were the largest. Some representative reactions are demonstrated in Figure 3. Changing from protic to dipolar aprotic solvent, ionic reactions showed balancing situation where rate didn't change much. In this case, that δG_{tr}^{T}, δG_{tr}^{R} had the same sign. However, when the transition states were stabilized in aprotic solvent, δG_{tr}^{T}, δG_{tr}^{R} had the opposite signs. The rate had been positively reinforced.

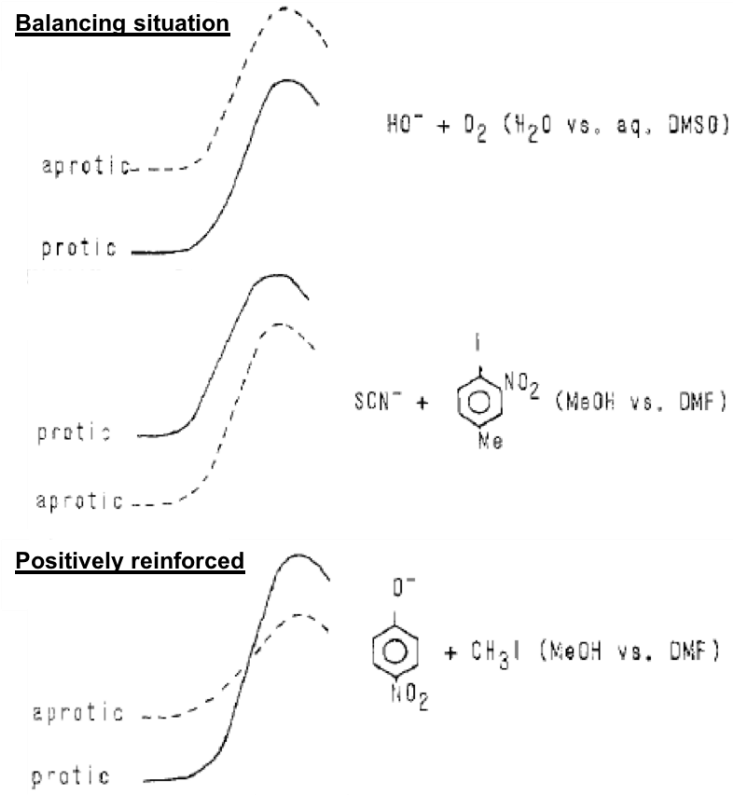

Figure 3. Free energy diagram of ionic reactions and effect of solvent when medium was changed from protic to dipolar aprotic. (Adapted from [31])

When a homogenous reaction is carried out in a solvent, both initial/reactant states and transition states are solvated. The participation of reaction ions and molecules are positively, negatively or neutrally charged by electrostatic interaction with solvents and catalyst. A useful way to visualize these solvation effect is by co-spheres introduced by Gurney[32, 33]. Reacting species are surrounded by an imaginary sphere which encloses

solvent molecules. When reactant co-sphere and catalyst co-sphere overlap with each other, the mutual destruction or construction of co-sphere leads to different disruption for two solvated molecules. One co-sphere may be disrupted by the other or get constructed together. The energy at transition state when using different solvents will be affected by the degree of disruption from both sides. Therefore, both initial/reactant states and transition states are solvated to different extents according to the solvating power of the solvent used. Therefore, a reaction can be promoted or retarded.

In heterogeneous catalysis, reactions happen over surfaces with elementary steps as adsorption, surface reaction and desorption. Rate determining step states the overall reaction rate while other steps are quasi-equilibrated.

Madon and Iglesia[34] discussed effect of solvents on kinetically relevant elementary steps. A typical heterogeneous catalytic reaction system is a gas-liquid-solid system where reactants and catalysts are dissolved in inert solvents. When bulk reactants are in equilibrium with gas phase, the chemical potential of the liquid phase and the gas phase should be the same. Reaction rates are identical in both phases no matter solvents are involved. Hereby, in order to change the rate of heterogeneous catalytic reactions, solvents must find a way to influence kinetic rate constants in rate expressions and activated complexes of the rate-determining step.

Two different scenarios were further explained combing with the solvent effects observed in cyclohexene hydrogenation over Pt[35] and Pd[36]. In the case of cyclohexene hydrogenation over Pt, the rate was found to increase with hydrogen solubility in solvents. When the rate determining step is adsorption step as an entry elementary step or desorption step as an exit elementary step as follow:

$$A + * \xrightarrow{k_{enty/adsorption}} A* \quad (31)$$

$$B* \xrightarrow{k_{exit/desorption}} B + * \quad (32)$$

where $*$ is surface active sites, A and B are reactant and product respectively, activated complexes may be affected to the same extent as reactants or products in the liquid phase. Because entry/adsorption step is usually an exothermic reaction with an early transition states yet exit/desorption step is an endothermic reaction with late transition states. The solvent solvation effect of bulk molecules and activated complexes are identical and therefore the effect is cancelled. Since the rate determining step over Pt is H_2 dissociation, an entry step, the solvation effect for initial states and transition states is identical, leaving the liquid phase H_2 concentration in the rate expression. On the other hand, when rate determining step involves surface adsorbed species,

$$A* + B* \xrightarrow{k} AB* \quad (33)$$

surface reacting species $A*$, $B*$ and the activated complexes $AB*^{\ddagger}$ are predominately influenced by strong chemical bonds to surface active sites. Solvation does not play a role to initial states and transition states. Therefore, rate of cyclohexene hydrogenation over Pd was found to be independent of solvents since the surface reaction of adsorbed hydrogen and adsorbed cyclohexene was the rate determining step.

3.2 Solvent Effect on Hydrogenation

Many aspects attributed to solvent effects on hydrogenation have been investigated such as solvent electrical properties[37-44], thermodynamic non-ideality[34, 44-47], solvent hydrogen solubility[34, 35, 42, 43, 48, 49], solvent competitive adsorption[39, 40, 44, 50, 51], intrinsic kinetics[52-55], and so forth.

3.2.1 Solvent effects related to electrical properties

Solvents are categorized as non-polar, aprotic, and protic solvents. Solvent electrical properties such as dielectric constant (ε) and electrical dipole moments (μ) determines the polarity of solvents. Dielectric constant ε measures ability to insulate charges between substances. Therefore higher ε represent higher polarity. Many studies have investigated solvent effects related to electrical properties. However, there are no clear correlation between solvent polarity on hydrogenation rate, although polar solvents may interact stronger with reactants than nonpolar solvents.

The catalytic hydrogenation of *p*-nitrophenol to *p*-aminophenol were studied over Pt/C in 5 polar solvents with different dielectric constants using a batch slurry reactor[37]. Dielectric constant ε measures ability to insulate charges between substances. Therefore higher ε represent higher polarity. As listed in Table 2, water has the highest dielectric constant and thus a highly polar solvent among all. The least polar solvent is n-butanol with the smallest dielectric constant. The hydrogenation rate in those 5 solvents increased with dielectric constants, solvent polarity, and was enhanced from 0.342 kmol/kg·h to 3.066 kmol/kg·h from switching n-butanol to water. The rate acceleration was considered to be the increase in interactions of nitro compounds in more polar solvents that increased the solution activity, a thermodynamic parameter, and the rate was enhanced.

Table 2. Effect of solvent on rate of hydrogenation (N)[a]. (Adapted from [37])

Solvent	ε	N (kmol/kg·h)
water	78.5	3.066
methanol	32.6	2.160
Ethanol	24.3	1.960
n-propanol	20.1	1.790
n-butanol	17.8	0.342

[a] Reaction conditions: initial concentration of *p*-nitrophenol, 0.479 kmol/m^3; 1% Pt/C, 0.266 kg/m^3; solvent, 3×10^{-5} m^3; H_2 pressure, 2.73 MPa; temperature, 353 K.

On the contrary, hydrogenation of acetophenone over Ni/SiO2 in polar solvents demonstrated rate decrease with solvent polarity[39]. Liquid phase hydrogenation of acetophenone (AP) to 1-phenylethanol (PhE) was carried out in 10 solvents including protic solvents (C_1-C_3 alcohols), aprotic polar solvents (tetrahydrofuran, γ-butyrolactone, and acetonitrile) and apolar solvents (cyclohexeane, toluene, and benzene). The hydrogenation rate generally followed the order of protic solvents > apolar solvents > aprotic polar solvents, although there were exceptions. The initial rates and solvent polarities are presented in Table 3, and the data are plotted in Figure 4. Electric dipole moments, μ, are also used to evaluate solvent polarities. Molecules is more polar when μ is higher. In protic solvents, Figure 4 (a), the hydrogenation rate decreases with solvent polarities. Strong interactions between AP and alcohols hinders the adsorption of AP onto Ni surfaces. These solvent-solute interactions are mainly through dipole-dipole and H-bonding. As the results, AP molecules are solvated in alcohols instead of going to the Ni surface due to strong polarities of protic solvents. For aprotic solvents, Figure 4 (b), and apolar solvents, Figure 4 (c), there are no clear trends in hydrogenation rate as a function of solvent polarities. Similar non-consistent results were also seen in selective hydrogenation of 2-methyl-3-butyn-2-ol by Nikoshivili et al[42]. The hydrogenation rate decreased with dielectric constants in polar solvents yet increased in non-polar solvents.

Table 3. Initial rates of AP hydrogenation in solvents and its dielectric constants and electric dipole moments[a]. (Adapted from [39])

Solvent	ε	μ (Debye)	r_{AP}^{0} (mol/min·g)
2-propanol (2-PrOH)	19.9	1.66	1.09×10^{-3}
1-pronanol (1-PrOH)	20.1	1.68	5.20×10^{-4}
ethanol (EtOH)	24.6	1.69	3.91×10^{-4}
cyclohexane (CHX)	2.02	0.00	2.91×10^{-4}
toluene (TOL)	2.38	0.37	2.03×10^{-4}
tetrahydrofuran(THF)	7.58	1.63	4.44×10^{-5}
γ-butyrolactone(GBL)	39.0	1.43	3.35×10^{-5}
methanol (MeOH)	32.7	1.70	2.75×10^{-5}
benzene (BZN)	2.28	0.00	0
acetonitrile (ACN)	37.5	3.92	0

[a] Reaction conditions: initial concentration of AP, 0.168 M; 7.6% Ni/SiO2, 0.5 g; solvent, 150 mL, H2 pressure, 8.7 bar; temperature, 363 K.

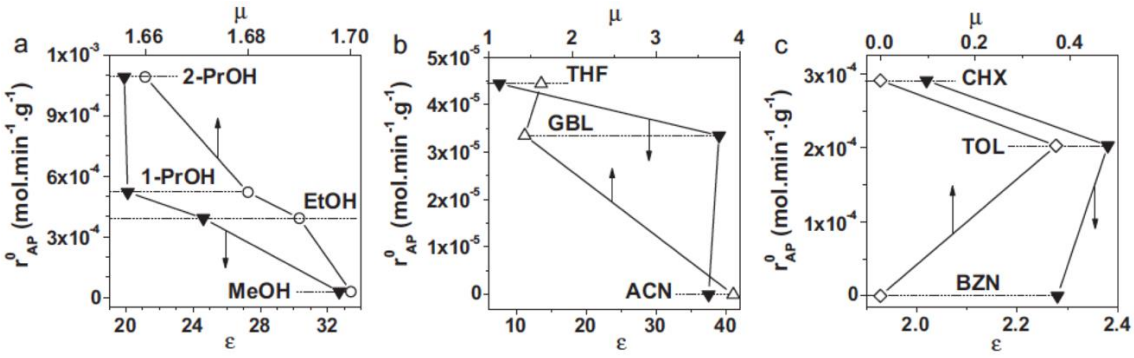

Figure 4. Initial rate of AP hydrogenation as a function of dielectric constants (ε) and electric dipole moments (μ) in (a) protic solvents, (b) aprotic polar solvents, and (c) apolar solvents. Reaction conditions: initial concentration of AP, 0.168 M; 7.6% Ni/SiO2, 0.5 g; solvent, 150 mL, H_2 pressure, 8.7 bar; temperature, 363 K. (Adapted from [39])

Solvent polarities on hydrogenation rates have been investigated, however a consistent conclusion with a respect with solvent electronic properties are unsettled. Dielectric constant is widely considered as the macroscopic parameter to evaluate molecule electrostatic continuum. Unfortunately, it fails to distinguish between truly nonpolar solvents (e.g., cyclohexane), which chemical bonds are identical and nonpolar, and non-dipolar solvents such as benzene, which chemical bonds are polarized although the

macroscopic electrostatic measurement indicates nonpolar as the result of electron delocalization. The higher-order multipole moments including quadrupole and octupole of those non-dipolar solvents can interact with surface adsorbed species and change the magnetic relaxation rate of the nucleus. The kinetic of rate may be influenced correspondingly[40].

3.2.2 Solvent effects related to thermodynamic non-ideality

An inevitable issue arises in liquid phase reaction when reaction mixture becomes non-ideal mixture. The interactions within the reaction system, quantified by activity coefficient, affect the thermodynamic tendency towards equilibrium so that the number of surface species alters[34, 47]. Strong interactions of solvent and reactant results a low activity coefficient, representing that reactant prefers to be solvated within solvent. As a result, adsorption may be hindered on catalysts. On the contrary, weak interactions indicates a high activity coefficient and repels reactants to catalyst surface to facilitate adsorption. In another word, the adsorption of a non-polar reactant can be greatly favored in a polar solvent while a polar reactant can be promoted in a non-polar solvent[56].

Rajadhyaksha and Karwa[46] compared activity coefficients of the reactant o-nitrotoluene in different solvents with its hydrogenation rate. The hydrogenation rate was found to increase with activity coefficient. When methanol was used as the solvent, the activity coefficient for reactant o-nitrotoluene evaluated by UNIFAC method was 5.1. In cyclohexanol, activity coefficient was 2.6, the lowest among all the solvents investigated at the same composition. The UNIFAC method had presented a better experimental agreement in highly polar solvents by Lo and Paulaitis[45]. The rate of o-nitrotuluene hydrogenation indicated the highest in methanol, followed by in 2-propanol, 2-butanol and

the lowest in cyclohexanol. The rate was in line with the activity coefficient. Therefore, a higher activity in a solution could result in an increased concentration of adsorption species on catalyst surface at a given concentration in the bulk phase. This resulted a better adsorption compared to those with low activity.

3.2.3 Solvent effects related to solvent hydrogen solubility

Liquid phase hydrogenation involves reactant adsorption on catalyst surfaces as the entry elementary step. Gas phase H_2 firstly dissolves in solvents and then goes to the surface. It's reasonable to relate solvent effect to hydrogen solubility. Thermodynamic analysis has indicated that hydrogen could influence the overall hydrogenation rate. Nevertheless, compare to other attributes such as competitive adsorption and intrinsic kinetics, the influence of hydrogen solubility is insignificant.

Rautanen et al[49] carried out in hydrogenation of toluene in isooctane, n-heptane and cyclohexane over Ni/Al_2O_3. Kinetic modeling over a broad range of reaction conditions at 100 – 200 °C and 20 – 40 bar revealed that solvents didn't compete with toluene adsorption and there were no other solvent effects. The difference between hydrogenation rates in solvents were attributed to the differences in H_2 solubility, which had the same trend as the hydrogenation rate.

Boudart et al. inspected solvent effect of cyclohexene hydrogenation over Pt/SiO_2[35] and Pd/SiO_2[36]. The comparison in Table 4 indicates that the effect of hydrogenation rate on H_2 solubility depends on nature of catalysts. The turnover frequency (TOF) of cyclohexene hydrogenation over Pt/SiO_2 increased with H_2 solubility in different types of solvents. The highest TOF was found in solvent n-heptane. Over Pd/SiO_2, TOF stayed relatively constant in non-aromatic solvents. H_2 solubility didn't increase nor

decrease hydrogenation rate. Although reactivity in benzene was inhibited, it was explained to be strong competitive adsorption of benzene on Pd/SiO_2.

Table 4. Turnover frequency (TOF) for hydrogenation of cyclohexene in different solvents over Pt/SiO_2 and Pd/SiO_2. (Adapted from [35, 36])

Solvent	H_2 solubility $\times 10^6$ (mol/cm^3)	TOF over Pt/SiO_2[a] (/s)	TOF over Pd/SiO_2[b] (/s)
cyclohexane	3.97	8.67	7.80
n-heptane	4.85	12.57	7.95
p-dioxane	1.90	4.84	/
ethyl acetate	3.77	10.15	7.93
methanol	3.40	7.92	7.85
benzene	3.07	6.86	0.58
cyclohexene	3.57	8.40	/

[a] Reaction conditions: temperature 307 K; H_2 pressure, 101.3 kPa; solvent, 20 cm^3.
[b] Reaction conditions: temperature 308 K; H_2 pressure, 101.3 kPa; initial concentration, 0.24 M.

The surface elementary steps for cyclohexene (R) hydrogenation on Pt [34, 35]are

$$H_2^g \Leftrightarrow H_2^l \tag{34}$$

$$H_2^l \Leftrightarrow H_2^p \tag{35}$$

$$H_2^p + ** \overset{k_3}{\rightarrow} 2H* \tag{36}$$

$$R + ** \Leftrightarrow *R* \tag{37}$$

$$*R* + H* \Leftrightarrow RH* + ** \tag{38}$$

$$RH* + H* \Leftrightarrow RH_2 + ** \tag{39}$$

Gas phase H_2 is in equilibrium with liquid dissolved H_2, which equilibrate with precursor states H_2. Dissociative adsorption of precursor state H_2 in Eq. (36) over Pt is irreversible and becomes the rate determining step while other steps are all quasi-equilibrated. Therefore, the rate expression derived from transition state theory for non-ideal solution Eq.(27) is

$$r = \frac{k_B T}{h} K^{\ddagger} \frac{\gamma_{H_2^p} C_{H_2^p}}{\gamma^{\ddagger}} \tag{40}$$

Where $K^{\ddagger}$ is the reaction equilibrium between H_2^p to the activated complex before forming surface adsorbed $H*$. Combining the equilibrium with the liquid phase H_2 in Eq. (35),

$$K_H = \frac{a_{H_2^P}}{a_{H_2^l}} \tag{41}$$

activity of precursor H_2 is expressed into liquid phase H_2 as follows

$$r = \frac{k_B T}{h} K^{\ddagger} K_H \frac{\gamma_{H_2^l} C_{H_2^l}}{\gamma^{\ddagger}} \tag{42}$$

Since the rate determining step is an exothermic entry elementary step with a low activation energy, it's considered as an early transition state. Therefore, activated complex in Eq. (36) closely assembles solvated H_2 in liquid phase. Solvent solvation effect on $\gamma_{H_2^l}$ and $\gamma^{\ddagger}$ are identical[35]. Hereby, the cancellation of both terms leads to

$$r = \frac{k_B T}{h} K^{\ddagger} K_H C_{H_2^l} \tag{43}$$

Where hydrogenation rate is dependent on H_2 solubility.

On the contrary, cyclohexene hydrogenation in non-aromatic solvents over Pd/SiO_2 was demonstrated that surface reaction of adsorbed H and cyclohexene in Eq. (38) was the rate determining step. Surface reacting species $H*$, $*R*$ and the activated complexes $*RH*^{\ddagger}$ are predominately influenced by strong chemical bonds to surface active sites[34]. Solvation does not play a role to initial states and transition states. The activities for both terms stayed in the rate expression, which was found to be independent of solvents.

However, Singh and Vannice[48] suggested that solvent effect could also appear if the H_2 adsorption process was a quasi-equilibrium. The Langmuir-Hinshelwood model was

applied as the surface rate expression and the solvent competitive adsorption was assumed negligible. The overall chemical potential of H_2 adsorption on surface is 0. Integrating standard chemical potential (μ^0) for gas phase H_2 ($\mu^0_{H_2}|_{no\ solv}$), liquid phase H_2($\mu^0_{H_2}|_{solv}$),, surface adsorbed H (μ^0_{HS}) and vacant sites (μ^0_S) in the presence of a solvent(solv) or without a solvent(no solv), surface coverage θ_{HS} was derived as functions of H_2 adsorption solvent-independent equilibrium constant K_H, partial pressure P_{H_2}, and a constant α, which was a measure of the non-ideality imposed by the solvent. The expression is represented as

$$\theta_{HS} = \frac{\alpha K_H^{1/2} P_{H_2}^{1/2}}{1 + H^{-1/2} K_H^{1/2} P_{H_2}^{1/2}} \tag{44}$$

Where

$$\alpha = \exp\left(\frac{\mu^0_S|_{solv} - \mu^0_S|_{no\ solv}}{RT} - \frac{\mu^0_{HS}|_{solv} - \mu^0_{HS}|_{no\ solv}}{RT}\right) \tag{45}$$

α accounted for solvent effect on vacant sites and adsorbed H such as solvent polarity. Given that no solvent effect took place in the system, α would be 1. The surface coverage was therefore only a function of partial pressure and solvent in-dependent equilibrium constant, and the value would be constant in any solvents. The role of solvent was a transparent barrier for H_2 availability to the surface, although it was presumed to be rare. The further expanding of the chemical potential of the μ^0_S and μ^0_{HS} yielded

$$\alpha = \exp\left(\frac{\mu^0_{H_2}|_{non\ solv} - \mu^0_{H_2}|_{solv}}{2RT}\right) \tag{46}$$

In this case, α related to Henry's constant:

$$\alpha = H^{-1/2} \tag{47}$$

Therefore, surface coverage adsorbed H in Eq. (44) can increase with increasing H_2 solubility under a given partial pressure depending on solvents used. Henry's law describes that the amount of gas dissolved in liquid phase is proportional to its partial pressure in gas phase. It's an equilibrium that connects concentration and pressure. The relationship between surface adsorbed hydrogen and liquid phase hydrogen concentration was examined by Cerveny et al.[57] on 5% Pt/C at 300 K. As shown in Figure 5, the concentration of surface adsorbed H increased with solvent hydrogen solubility.

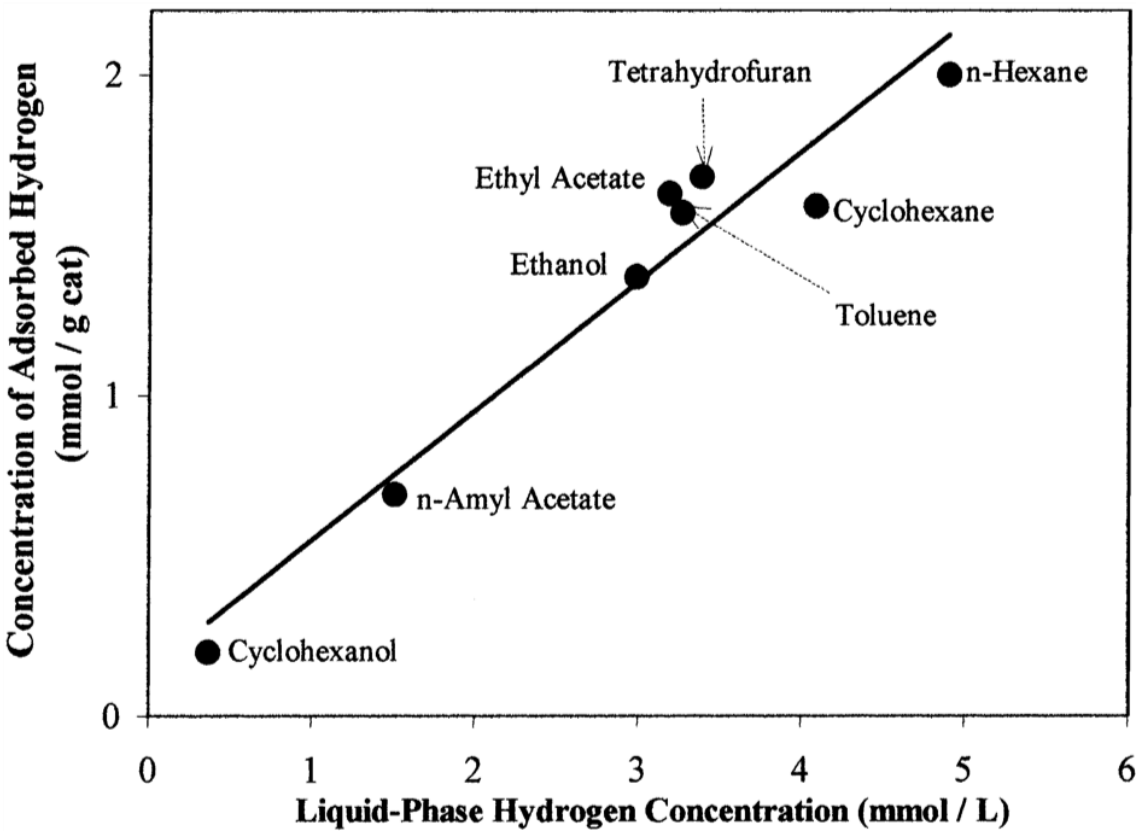

Figure 5. Relationship of surface adsorbed hydrogen and concentration of dissolved hydrogen in solvents. (Adapted from [56, 57])

The effect of H_2 solubility on hydrogenation rates has been routinely investigated as an aspect of solvent effect. Nevertheless, no consistent correlation has been observed in wider range of solvents[39, 41-43]. Solubility does influence hydrogenation rate, although

it is never a dominant effect that attributes to observed solvent effect compared to other solvent effects.

3.2.4 Solvent effects related to competitive adsorption

The interactions of solvent-catalyst usually manifest the solvent co-adsorption on catalyst surfaces. Since the reaction rate is a function of surface coverage of reactants, solvents partially block active sites and may decrease the surface coverage of reactants and therefore decrease the overall rate of hydrogenation. Therefore, hydrogenation kinetics using Langmuir-Hinshelwood model consider the solvent adsorption term.

Kishida and Teranishi modeled the hydrogenation of acetone over Raney Ni catalyst and investigated the solvent effect in n-hexane, cyclohexane, methyl alcohol and isopropyl alcohol[51]. Langmuir-Hinshelwood kinetic model was derived incorporating solvent surface coverage θ_S in the site balance along with acetone surface coverage θ_A and hydrogen surface coverage θ_H as,

$$\theta_A + \theta_H + \theta_S = 1 \tag{48}$$

The reaction rate υ was written as

$$\upsilon = k\theta_A\theta_H = \frac{k a_A C_A}{(1 + a_A C_A + a_s C_S)^2} \tag{49}$$

Where a_A and a_s are correlated to the difference in free energies of adsorption between acetone/solvents and hydrogen, $\delta\Delta G_A/\delta\Delta G_s$. The expression for a_A and a_s were defined as

$$a_A = \frac{1}{C_H} e^{-\frac{\delta\Delta G_A}{RT}} \tag{50}$$

$$a_S = \frac{1}{C_H} e^{-\frac{\delta\Delta G_S}{RT}} \tag{51}$$

As a matter of fact, a_A and a_s are modified equilibrium constants that represent adsorption of acetone and solvents. The mathematical kinetic model was able to capture the experimental data in Figure 6 and a typical L-H behavior was observed. The hydrogenation rate was the highest in n-hexane, followed by in cyclohexane, methyl alcohol and isopropyl alcohol. The effect of solvents on the reaction can be explained by difference of adsorption strength. The fitting parameters of a_s was 0 L/mol, 0.084 L/mol, 0.123 L/mol and 0.389 L/mol respectively to n-hexane, cyclohexane, methyl alcohol and isopropyl alcohol. a_A was 1.45 L/mol. Those modified equilibrium constants were in line with the solvent adsorption strength. However, the model didn't describe the acetone hydrogenation in water represented in Figure 6, dash line, indicating that k and a_A changed in water. This discrepancy was speculated to be that interactions between water molecules and catalysts not only participated competitive adsorption, but also interacted with adsorbed acetone and hydrogen so that the intrinsic kinetic parameters was no longer the same as in other solvents.

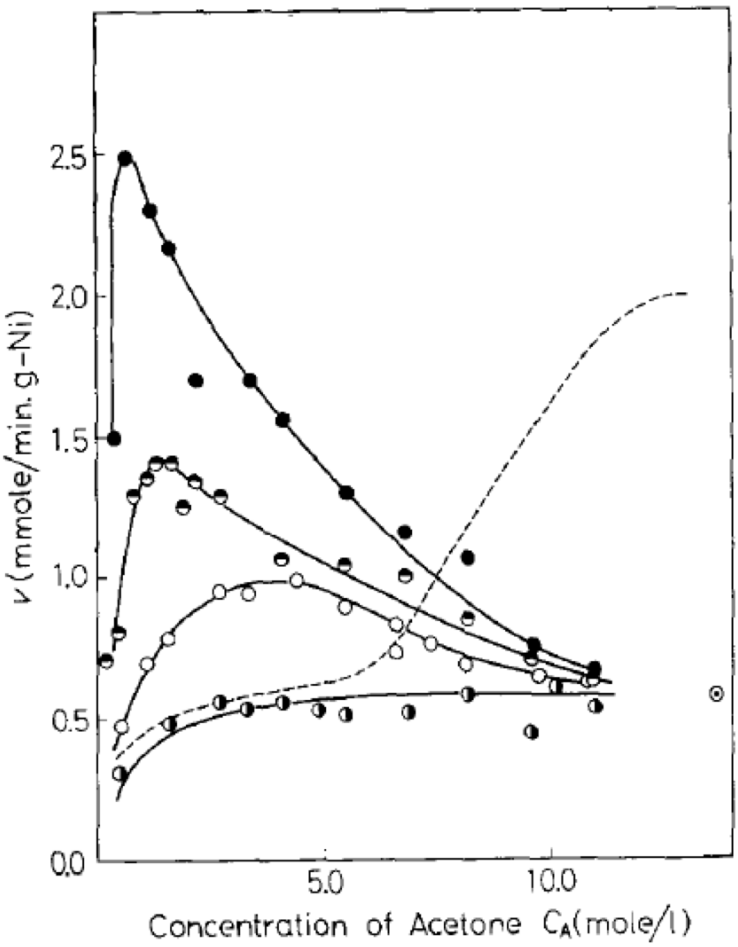

Figure 6. Acetone hydrogenation of Raney nickel catalyst at 10 °C. ●, in n-hexane; ◓, in cyclohexane; ○, in methyl alcohol; ◑, in isopropyl alcohol; - - -, in water. (Adapted from [51])

One way to justify the solvent competitive adsorption with reactant is heat of adsorption. In acetophenone(AP) hydrogenation over Ni/SiO_2 by Bertero el al.[39], heat of adsorption of AP and 10 solvents, listed in Table 3, were measured by calorimetry. The initial hydrogenation rate as a function of solvent heat of adsorption are presented in Figure 7. AP heat of adsorption of was around 19 kcal/mol, which was comparable to those of toluene(TOL), terahydrofuran (THF) and γ-butyrolactone (GBL); lower than those of benzene (BZN) and acetonitrile (ACN); higher than those of cyclohexane(CHX) and

alcohols. In non-polar solvents, rates decreased with the strength of adsorption, indicating TOL and BZN interacted stronger with Ni than AP. The reason for the rate inhibiting was caused by sites blocking. On the other hand, CHX with lower heat of adsorption had weaker interactions compared to AP, and rates were higher than those of BZN. Therefore, competitive adsorption of solvents was valid and it was the key parameter that generated solvent effect on AP hydrogenation when non-polar solvents were used. Similar phenomena were observed in aprotic polar solvents, THF, GBL and ACN. Although hydrogenation rates in aprotic solvents were much lower than that of non-polar solvents. This was due to the solvent-AP interaction discussed in 3.2.1Solvent effects related to electrical properties. Increased AP solvation in aprotic polar solvents hindered the adsorption. Last not the least, rates in protic solvents, alcohols, were much higher yet the enthalpies of adsorption were lower than that of AP. Solvent competitive adsorption failed to explain the observed solvent effect in protic solvents.

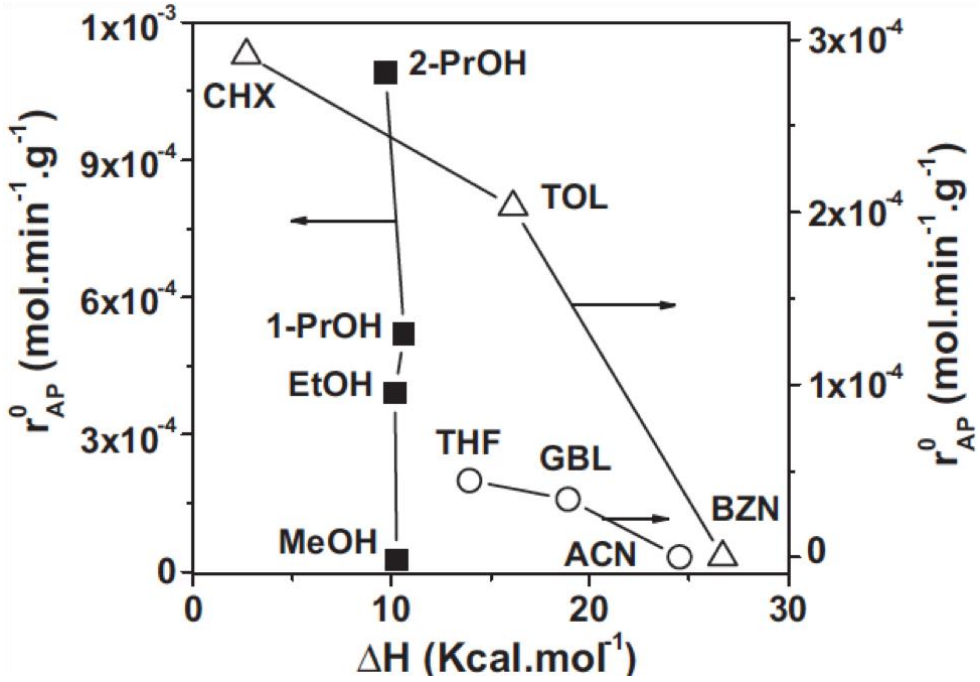

Figure 7. Hydrogenation rate as a function of heat of adsorption of solvents. Reaction conditions: T=363 K, P=10 bar, W_{cat}=0.5 g, C_{AP}=0.168 M, $V_{solvent}$=150 mL, stirring speed=700 rpm). (Adapted from [39])

3.2.5 Solvent effects related to intrinsic kinetics: alcohols and water

In many studies, hydrogenation rates exhibit higher or enhanced activity in protic solvents such as alcohols and water[39, 41, 42, 58, 59]. From previous review on solvent effect, protic polar solvents demonstrate interactions with reactants through dipole-dipole and H-bonding. Those interactions assist protic solvents take part in the kinetically relevant steps that influence intrinsic kinetics.

Alcohols acted as an additional H source to hydrogenate acetophenone to 1-phenylethanol through H-transfer reaction[39]. Dissociative adsorption of alcohols formed alkoxides and atomic hydrogen through O-H bond scission. The atomic H participated AP hydrogenation and increased the rate. The further tests were carried out in the absence of gaseous H_2 in 2-propanol, 1-propanol, ethanol and cyclohexane at reaction conditions with

N_2. After 5 hours, acetophenone hydrogenation product 1-phenylethanol was detected in all alcohols, but there was no conversion in cyclohexane. As the result of H-transfer reaction, acetone was detected in 2-pronanol. The hydrogenation activity through H-transfer reaction was the much higher in 2-propanol, followed by 1-propanol and slowest in ethanol. The reason was considered as secondary alcohols were better hydrogen donors than primary alcohols and atomic hydrogen were abundant on Ni surface when 2-propanol was used. Although primary alcohols as 1-propanol and ethanol were not good hydrogen donor solvents, the C=O bond in acetophenone could have been polarized through H-bonding so that the overall reaction barrier was lowered.

Generally, H-transfer is the mechanism that facilitates the hydrogenation reaction. Alcohols go through MPV (Meerwein-Ponndrof-Verley) reduction to provide extra H needed for ketone and aldehyde reduction to their corresponding alcohols on Lewis acid catalysts[60, 61]. Not only surface dissociated H atoms from gaseous H_2 but also H atoms in alcohols involve in reactions.

The similar interactions are discovered in the protic solvent water. Water participates hydrogenation reactions by involving in kinetically relevant steps during activation and changes the intrinsic kinetics.

The presence of water may modify the local adsorption geometry and favor chemisorption of reacting species. Michel et al. investigated the effect of water on ketone hydrogenation over Ru using model compound acetone[62]. Ru has a poor activity towards acetone hydrogenation in gas phase compared to Pt. However, it's more active in aqueous environment. The hydrogenation ability of 2-butanone over Ru/SiO_2 was 30 times faster in water than in heptane[52]. The DFT calculations demonstrated that the adsorption

geometry of acetone over Ru (0001) changed in the presence of a water molecule co-adsorbed. In the absence of water, as illustrated in Figure 8 (a), acetone adsorbed with C=O perpendicular to the surface with O bound on the surface. When a water molecule was co-adsorbed, the oxygen in acetone formed a H-bond with water and the adsorption geometry became parallel to the surface as illustrated in Figure 8 (b). The influence of water stabilized the adsorption of acetone by 0.18 eV. Eventually, the effective activation barrier was decreased by 35%, promoting the hydrogenation rate in aqueous environment over Ru.

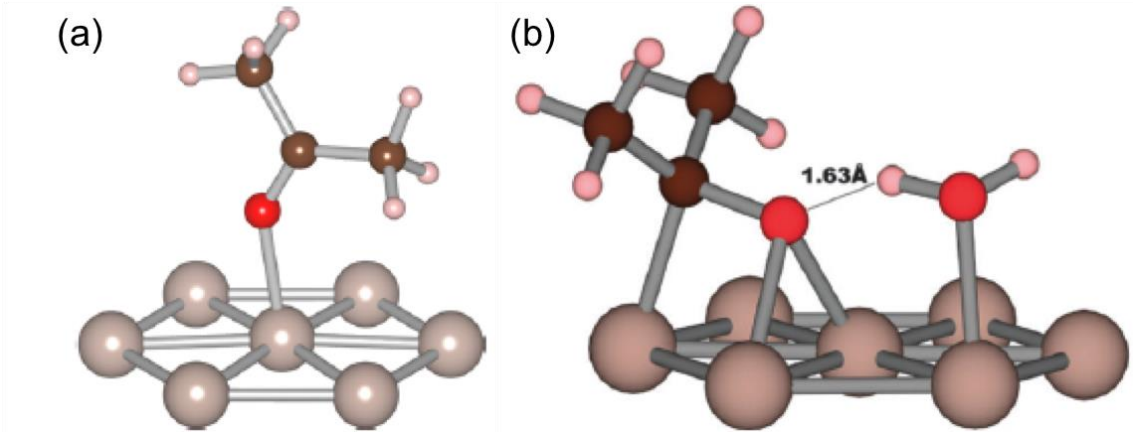

Figure 8. Adsorption geometry of acetone on Ru (0001). (a) without water, (b) water is co-adsorbed. (Adapted from [62])

Moreover, bulk water molecules could solvate both metal and reactant species at the same time during reaction. The adsorption of reactants has been calculated to be a combination of solvent effects to both metal and reactant. Yoon et al. [63] investigated phenol hydrogenation on Pt and Ni in the presence of water. The comparison of metal work function W in vapor and in water molecules indicated that W was reduced by 1.2 eV and 1.0 eV in Pt and Ni respectively in the aqueous solution. The decrease in W represents an induced surface dipole layer in which the net electron density transfers from water molecules to metal and thus metal is partially reduced. The higher reduction strength of

metal in the presence of water lead to a weaker adsorption of phenol, where the adsorption was referred to liquid solvated phenol constrained within the center of the water bulk slab. In Scheme 3, the heat of adsorption was -172 kJ/mol in vapor, however the adsorption energy in aqueous phase was lowered to -151 kJ/mol on Pt due to the water modification on metal surface electron density. Nevertheless, the reference state is all in vapor. The solvation energy of gas phase phenol to aqueous phase phenol, -58 kJ/mol, had been accounted for. The overall phenol adsorption energy was -209 kJ/mol, which was the combination of solvation energy and the adsorption. The difference of surface adsorbed phenol in vapor and in aqueous phase was -37 kJ/mol, smaller than that of the solvation of gas free phenol to aqueous phase. Because the surface-bound species were partially solvated.

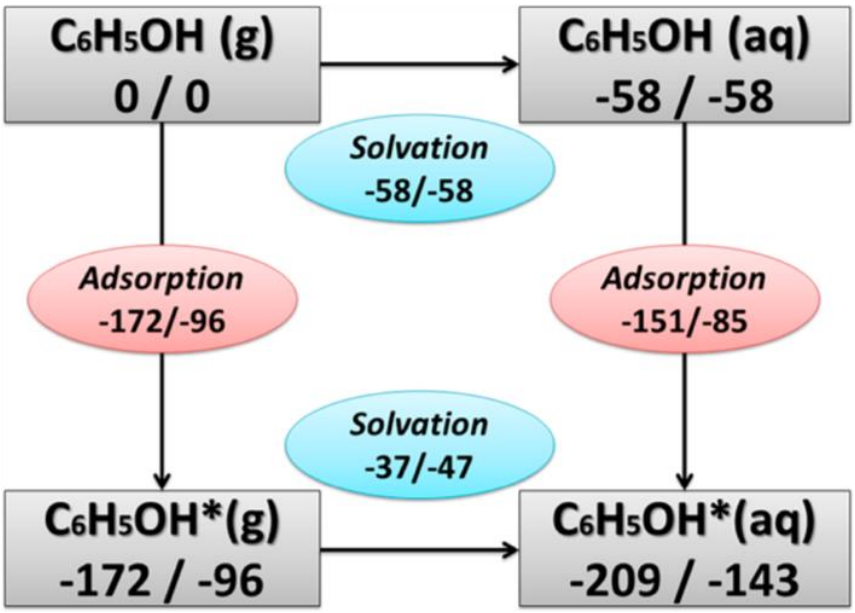

Scheme 3. Thermodynamic cycle for phenol adsorption on Pt (111)/Ni (111) in vapor and liquid phases. Unit is kJ/mol. (Adapted from [63])

Bulk water molecules can also take part in reaction activation and solvate charged reactive states and stabilize hydrogenation intermediates through water H-bonding

network[52, 53, 55, 63, 64]. The H-bonding stabilization effect on hydrogenation of 2-butanone has been investigated over Ru/SiO_2 by Akpa et al.[52]. In the presence of water or 2-propanol, the hydroxyl route, which the oxygen hydrogenation was the first step, had been found to more favorable than alkoxy route, which the carbon hydrogenation was first step. Both hydrogen and the oxygen in the transition state forming the hydroxybutyl intermediate, the first hydrogenation intermediate, interact with water molecules within the local solvation sphere via H-bonding, which decreased the activation barrier from 64 kJ/mol, in vapor, to 20 kJ/mol, in water. When 2-propanol was used as the solvent, the activation barrier was lowered from 64 kJ/mol to 32 kJ/mol, although the relative stabilization of the same transition states was not as strong as in the case of water. The second hydrogenation step, hydrogenation of the carbon, was slightly favored by the H-bonding interactions, yielding less activation barrier in water and 2-propanol than in vapor and they were 68 kJ/mol, 70 kJ/mol and 72 kJ/mol respectively.

Apart from water changes reactant adsorption geometer, modifies metal surface electron density and stabilizes surface adsorbed species, water mediated H-shuttling serves as a co-catalyst that provides an alternative hydrogenation pathway, which lowers reaction activation energy[53].

Fischer-Tropsch Synthesis (FTS) was greatly enhanced by co-feeding water with CO and H_2 over ruthenium[53]. Kinetically relevant steps of CO activation had been facilitated via water H-shuttling effect. There are routes for surface CO activation. Formyl route involves hydrogenation of the carbon followed by the hydrogenation of the oxygen. However, hydroxymethylidyne route inclues hydrogenation of the oxygen first and then the carbon. The energy diagram for both routes in vacuum, Figure 9 (a), had high energy

barrier for both routes. In the presence of water, Figure 9 (b), the transition state energy for the first hydrogenation of the oxygen in hydroxymethylidyne route had been decreased from 186 kJ/mol to 111 kJ/mol, and the second hydrogenation of the carbon was slightly favored by water. The energy was reduced from 123 kJ/mol to 111 kJ/mol. The significant activation energy reduction appeared during the formation of COH* via water H-shuttling effect in Figure 10, where the water molecule picked up a surface H atom and shuttled it to the oxygen of surface CO*. The H-shuttling process reduced the transition state energy of first hydrogenation step to 111 kJ/mol, resulting a rate increase since the energy barrier for CO activation was 109 kJ/mol, while the overall energy barrier was 152 kJ/mol without the effect of water.

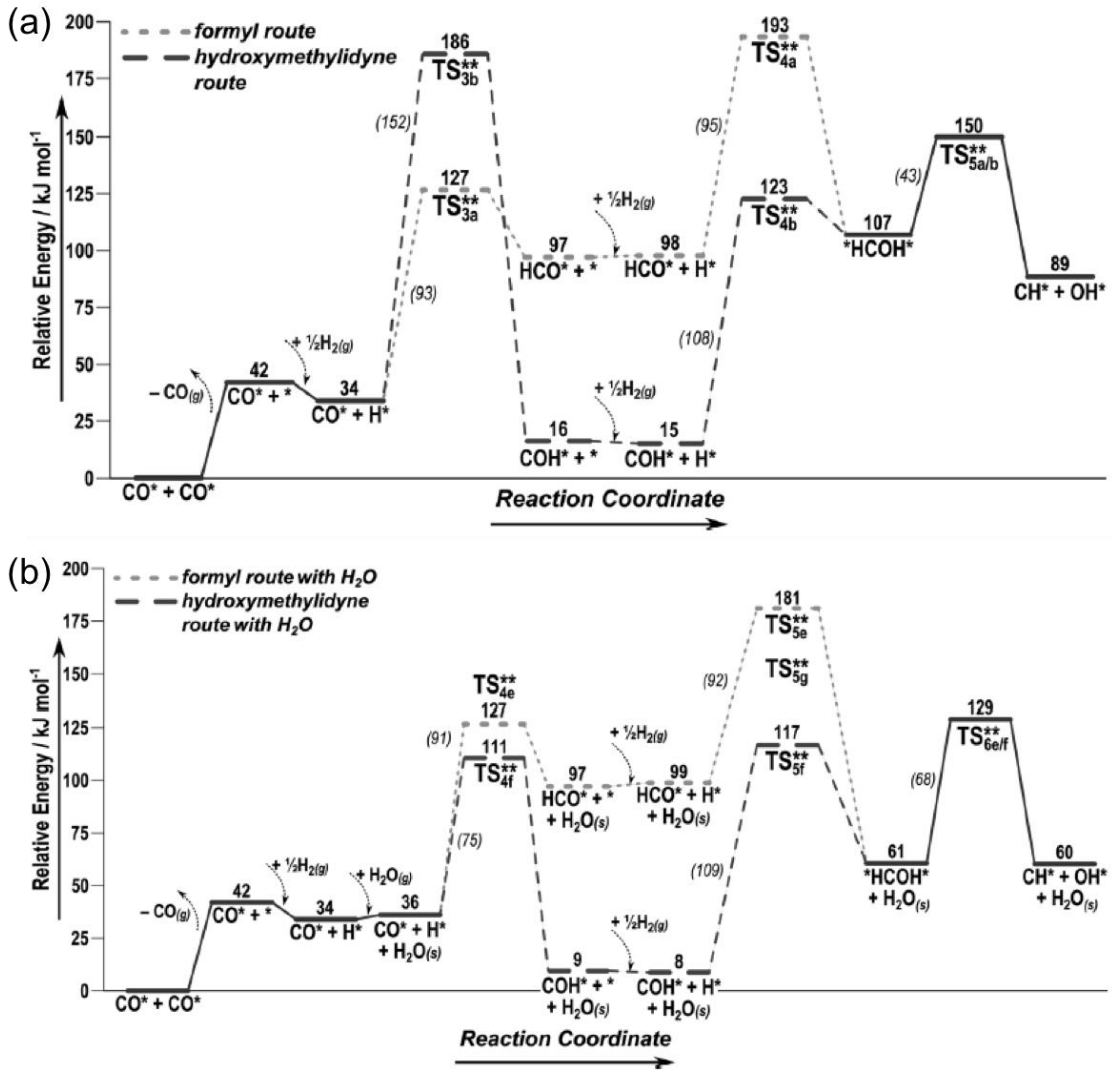

Figure 9. Reaction coordinate diagrams for CO activation mechanisms over Ru. Intrinsic activation barriers are in italics and effective barriers are in bold. (a) in vacuum, (b) in the presence of water. (Adapted from [53])

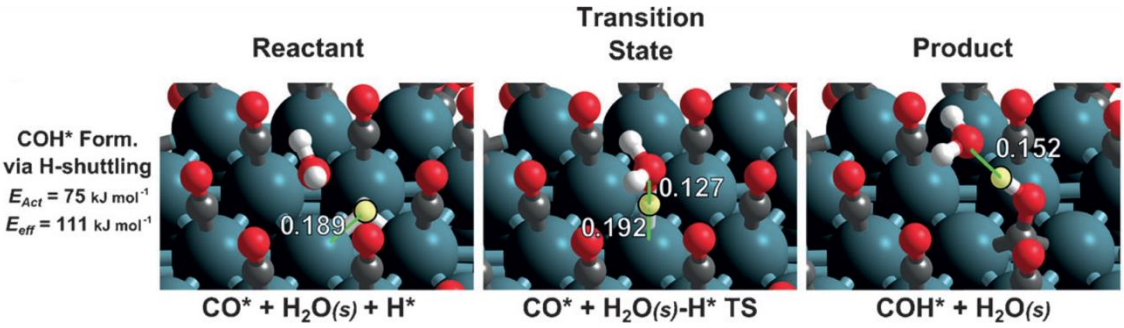

Figure 10. DFT-derived structures for water-mediated hydroxymethylidyne route. H atom is highlighted in yellow and distances are in nm. (Adapted from [53])

In addition, solvent is capable of transporting charged reaction species. Especially in water, long-range proton hopping, known as the Grotthuss mechanism, transfers protons through the H-bonding network with a low activation barrier of around 10 kJ/mol[65], making the H sources more accessible. Grotthuss-like mechanism mediates the diffusion of surface H atoms over heterogeneous catalyst surface, activating the fast and long-range proton diffusion at the catalyst interface. Merte el al. conducted the STM (high-resolution, high-speed scanning tunneling microscopy) of the diffusion of H atoms on FeO/Pt and demonstrated a rapid H diffusion in the presence of a water molecule[66]. The DFT calculation further indicated that partition of a water molecule during proton hopping implements the formation of an H_3O^+-like transition state, which lowered the activation barrier from 1.02 eV to 0.21 eV.

Chapter 4: Non-ideal Solvent Effect on Kinetics of Cyclohexene Hydrogenation over Pd/α-Al_2O_3[*]

4.1 Introduction

Considerable amount of biomass conversions to high value products has been conducted in liquid-phase conditions. Bio-oil, produced by fast pyrolysis, is highly viscous and oxygenated liquid with a large portion of water[67]. Biomass upgrading in liquid environment is a superior strategy since the application of solvents could not only lower the energy consumption with mild reaction conditions, dissolve reactants, products and transfer heat but also provide an additional degree of freedom to engineer reactions[30]. The observed rate change when applying different solvents to a chemical reaction is solvent effect[29]. In heterogeneous catalysis, studies have investigated the phenomena based on solvent interactions in the liquid-phase system such as solvent-reactant, solvent-catalyst and solvent-solvent interactions. Many aspects attributed to solvent effects on hydrogenation have been investigated such as solvent electrical properties[37-43], thermodynamic non-ideality[34, 45-47], solvent hydrogen solubility[34, 35, 42, 43, 48, 49], solvent competitive adsorption[39, 40, 50, 51], intrinsic kinetics[52-55], and so forth. The detailed discussions are presented in Chapter 3: Solvent Effect Due to the diversity and complexity of biomass-derived compounds, solvent effects could be initiated by multiple aspects all combined together[39].

Kinetic modeling and surface science studies have been employed to give insights on surface reactions. An accurate kinetic model not only describes experimental

[*] DFT calculations were performed by Dr. Qiaohua Tan and Tong Mou;
TEM images were taken by Brent Johnson and Lisa Whitworth at Oklahoma State University.

phenomena mathematically, fulfills predictions for wider range of process conditions, but also provides valuable information for theoretical calculations. Hereby, kinetic fittings for equilibrium and rate constants are inevitable in order to develop systematic theories. Constructed from fundamental kinetics of elementary reaction steps, microkinetic models cover a broader range of reaction conditions with improved accuracy by taking into account of molecular transformation on catalyst surfaces[68]. Therefore, thermodynamic properties such as entropy change and enthalpy change during adsorption and reaction can be interpreted. Moreover, the theoretical calculations on surface reactions have demonstrated significant insights on analyzing energy profiles such as heat of adsorption and reaction activation. The prediction from theoretical calculation can then be validated by parameters obtained experimentally from kinetic studies.

In order to achieve fundamental understandings on solvent effect and reaction mechanisms, kinetic studies on a cleaner and simpler reaction in inert solvents are much preferred.

Hydrogenation of cyclohexene has been studied in both gas phase and liquid phase over supported metal catalysts[35, 36, 69-74]. The effect of solvent over supported Pd[36] has been revealed that the reaction rate is independent of inert solvents under 264-308 K reaction temperature, as well as 4-89 kPa hydrogen partial pressure with atmospheric total pressure. The reaction orders under these reaction conditions have been found to be 0.5^{th} order with respect of hydrogen and 0^{th} order based on cyclohexene. However, the reaction kinetic and the possible solvent effect in much wider range of H_2 pressure at higher temperature has not been investigated. Meanwhile, an inevitable issue arises in liquid phase reaction when reaction mixture becomes non-ideal mixture. The interactions within the

reaction system, quantified by activity coefficient, affect the thermodynamic tendency towards equilibrium[34, 47] so that the number of surface species alters. A higher activity in a solution can result in an increased concentration of adsorption species on catalyst surface at a given concentration in the bulk phase[46]. On the contrary, a lower activity can result in an decrease concentration of desorption species on catalyst to achieve higher product solubility in a solution[34, 75]. Therefore, the reaction rates and product distributions may be changed accordingly. It is necessary to incorporate activity coefficient into kinetic models to represent the non-ideality of liquid phase reactions.

In this chapter, three inert nonpolar solvents, heptane, methylcyclohexane and decalin have been used in cyclohexene hydrogenation. Wider reaction conditions ranging from 30 psi to 600 psi of hydrogen under 40 °C – 100 °C have been utilized. The kinetic reveals that H_2 dissociative adsorption happens on different sites that don't compete with cyclohexene and solvent. Moreover, benchmarked by DFT calculation on the reaction energy barrier, the first hydrogenation step of surface cyclohexene species is the rate determining step. The solvent effect is due to solvent competitive adsorption and has been quantified as different surface coverages of reactant cyclohexene and solvents. The effect of solvent competitive adsorption on surface coverage has been further demonstrated in co-solvent mixture in which non-ideality of solution mixture could have great impacts on reaction rates. Last not the least, combined with the statistical thermodynamic analysis, the kinetic fittings on entropy of adsorption ΔS unveil that surface cyclohexene and hydrogen retain a certain amount of entropy based on their degree of freedom. The corresponding enthalpies of adsorption ΔH acquired are comparable with DFT studies, which simulate the experimental conditions. The enthalpy of adsorption is also coverage dependent.

Cyclohexene and hydrogen release more heat, more negative value of heat of adsorption, when absorbed on a clean surface. As coverage increases, the heat of adsorption decreases linearly and its value becomes less negative.

4.2 Experimental

4.2.1 Catalyst synthesis

The catalyst used in this study was synthesized by conventional incipient wetness impregnation. 0.25 wt.% Pd/α-Al_2O_3 was considered to potentially minimize the effect of mass transfer. Non-porous material α-Al_2O_3 had been applied to eliminate the internal mass transfer and the low metal loading had been applied so that the measured rates are within kinetic regimes. Since alpha phase Al_2O_3 is acquired by calcination in between 1000 °C – 1200 °C[76], support acidity is therefore negligible. The aqueous solution of catalyst precursor palladium(II) nitrate dihydrate (Sigma-Aldrich) was added drop by drop onto the catalyst support α-Al_2O_3 (Sigma-Aldrich) followed by drying at 70°C overnight. The sample was then calcined in air for 6 h at 300°C.

4.2.2 Characterization

Supported 0.25 wt.% Pd catalysts were characterized in a transmission electron microscope JEOL JEM-2100, operating with an accelerating voltage of 200 kV, equipped with LaB6 gun. The TEM sample was prepared by drop-casting a solution, which pre-reduced 0.25 wt.% Pd/α-Al_2O_3 was well dispersed in propanol by sonication, onto a holey carbon film mounted on a copper TEM grid. The Pd particles were analyzed using ImageJ to acquire particle size distribution and surface structure.

4.2.3 Catalytic reaction

The liquid-phase catalytic reactions of cyclohexene hydrogenation were carried out in the 300 mL high temperature and high pressure Parr batch reactor equipped with IR probe (Mettler Toledo ReactIR iC 10) for in-situ spectroscopic investigations[77]. The reactor setups are illustrated in Figure 11.

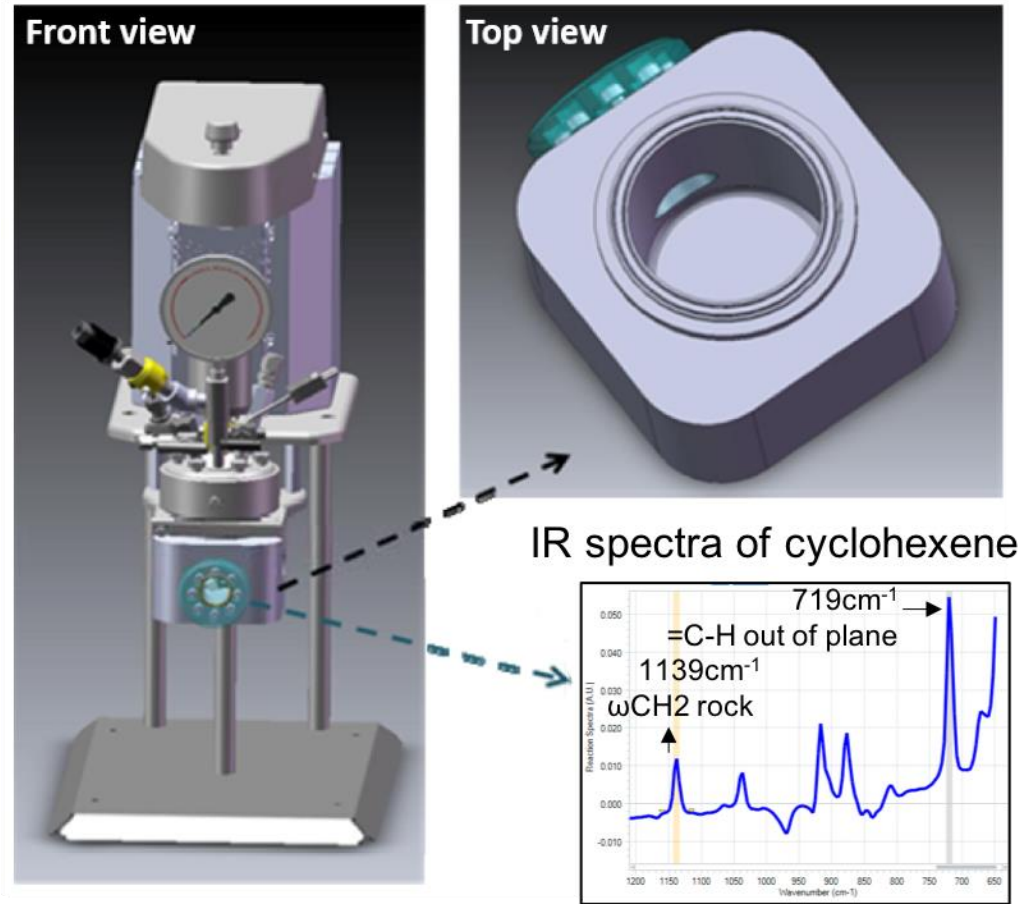

Figure 11. Parr reactor equipped with ATR-IR probe and the IR spectra of cyclohexene. (Adapted from [77])

Aprotic inert solvents used in the study were heptane (Sigma-Aldrich, anhydrous, 99%) methylcyclohexane (Sigma-Aldrich, anhydrous, ≥99%), decalin (Sigma-Aldrich, anhydrous, ≥99%). The reactant cyclohexene (Sigma-Aldrich, BHT as inhibitor, ≥99%)

was first distillated in N_2 flow at 50°C to separate the inhibitor BHT. The distillated cyclohexene was then filtered through a column packed with γ-Al_2O_3 (Alfa Aesar) to remove trace amount of other impurities that may cause serious catalyst deactivation during reaction. The purified cyclohexene was stored in a freezer when not being used.

Certain amount of catalyst 0.25 wt.% Pd/α-Al_2O_3 and 100 mL solvent were initially charged into the reactor vessel. Catalyst was reduced in excess hydrogen at 100°C[78] for an hour. 20 mL of reactant feed containing cyclohexene was pressurized in the reactor vessel to the desired pressure at the reaction temperature ranging from 40°C to 100°C. The reaction pressure had been varied widely from 35 psi to 600 psi. For co-solvent mixture, the second solvent was added along with the catalyst at the beginning of the reduction.

The IR probe allows the in-situ quantification of liquid phase cyclohexene hydrogenation. Before the reactant injection, the probe scanned and subtracted the background. When the reactant feed was purged in the vessel, the reaction started. The scan took place every minute. The characteristic IR absorption frequencies of 1139 cm^{-1} (ωCH_2 rock) and 719 cm^{-1} (C-H out-of-plane bending)[79] on the acquired IR spectrum were utilized for quantifications due to the uniqueness that they only appeared in cyclohexene (Figure 11) . By plotting the cyclohexene concentration change as the function of time, hydrogenation reaction rate was achieved by measuring the slope of the reaction IR profile.

After reaction, the liquid phase was analyzed by 7890B Agilent GC-FID equipped with ZB-5 GC column. The conversion calculated from GC results were compared with IR results for consistency. Meanwhile, the carbon balance was verified to validate the IR results.

Conversion is defined by the following equation:

$$x\% = \frac{mole\ of\ reactant\ reacted}{mole\ of\ reactant\ fed} \times 100\% \quad (52)$$

4.3 Results and discussion

4.3.1 Pd particle distribution and surface structure

The TEM images of 0.25 wt.% Pd/α-Al_2O_3 is presented in Figure 12. Pd particles are homogenously dispersed on the support α-Al_2O_3. More than hundreds of Pd particles have been measured using ImageJ and the histogram of particle size distribution is plotted in Figure 12 (b). The surface-weighted average diameter is calculated to be 3.13 nm. The corresponding surface Pd dispersion is then determined to be 36%[80]. Therefore, the total number of surface Pd, catalyst site densities for reaction, can be calculated.

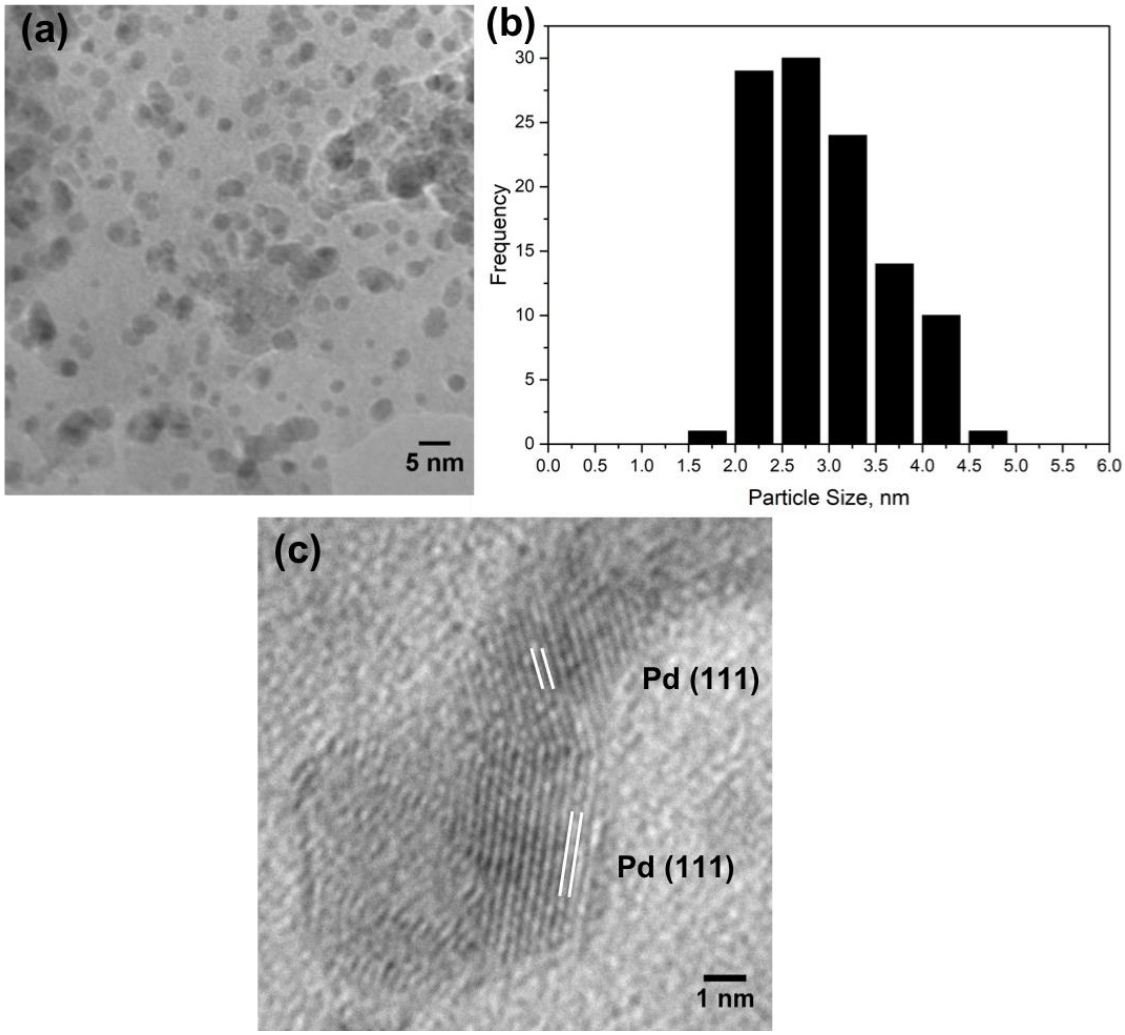

Figure 12. (a) TEM image of 0.25 wt.% Pd/a-Al_2O_3. (b) Histogram of Pd particles size distribution. (c) HRTEM image of Pd particles.

HRTEM images on surface Pd clusters illustrate the crystal structure. The lattice fringes in in Figure 12 (c) indicate crystallographic planes of Pd. Since the distance between two adjacent parallel planes of atoms is a function of atomic radii and the Miller indices (h, k, and l)[81], the spacing can be acquired. The empirical Pd atomic radii is 1.40 Å[82], and therefore the spacing for {111}, {110}, {100}, are theoretically 2.29 Å, 2.80 Å and 3.96 Å respectively. The average distance measured from TEM images is 2.35 Å, which is closer to 2.29 Å. Therefore, the surface Pd clusters of 0.25 wt.% Pd/α-Al_2O_3 are

composed of mostly (111) planes. The theoretical calculations had utilized closed-packed Pd (111) to model the catalyst.

4.3.2 Catalyst deactivation and kinetic regime

Cyclohexene hydrogenation reactions were conducted in three aprotic inert solvent, heptane, methylcyclohexane and decalin. The catalyst deactivation was evaluated first before the kinetic measurement.

Two different amounts of catalysts, 100 mg and 200 mg, were used for the reaction at the conditions of 70°C and 560 psi of H_2 for 45 min. The IR probe provides the advantages that the reaction profile with different amount of catalysts can be investigated with high-time resolution. As shown in Figure 13, the reaction profile of cyclohexene hydrogenation in heptane is presented on a diagram that x-axis has been plotted as the reaction time multiplied by the catalyst mass. In this way, reactions with different amount of catalyst are able to be compared on the same scale. Provided there was no catalyst deactivate, the reaction time needed to achieve the same conversion should be inversely proportional to the amount of catalyst used. Therefore, the experimental data using different amount of catalyst would overlap on the conversion vs. time × mass plot. However, the reaction with 100 mg of catalyst shows a slight deactivation compared to reaction with 200 mg of catalysts as the conversion becomes less and less after 20 min of the reaction. The same experiments were conducted in other two solvents. Reactions in methylcyclohexane and decalin also expresses slight deactivation after 20 min of reaction time. Furthermore, the only product in all pressure range is cyclohexane, and neither benzene formation nor rapid deactivation is observed even under low H_2 pressure, 30 psi. The deactivation is minimized on 0.25wt. % Pd/α-Al_2O_3. The kinetic hydrogenation rate

has been measured only by applying the first 20 min IR profile when the catalyst hasn't been deactivated.

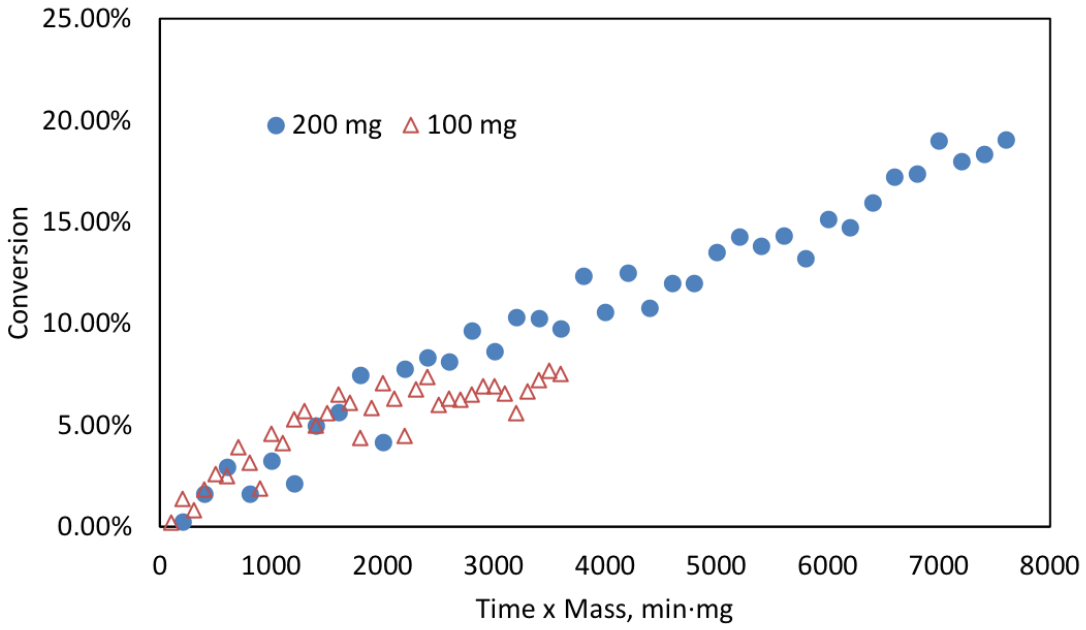

Figure 13. Deactivation study on 0.25 wt.% Pd/a-Al_2O_3. Reaction conditions: solvent heptane, H_2 pressure 560 psi, temperature 70 °C, cyclohexene initial concentration 0.42 M.

In order to acquire the true kinetic rate, mass transfer tests were carried out to assure the reaction conditions were free of transfer limitations. Since the reactions are conducted in liquid phase, heat transfer is not dominant due to the high heat capacities and good thermal conductivities of solvents[56]. The mass transfers in the liquid phase reaction can be categorized as gas to liquid, liquid bulk to catalyst surface and catalyst surface reactants diffusion to internal pores.

The catalyst support chosen in the study is non-porous α-Al_2O_3 with only 0.012 cm^3/g pore volumes measured by N_2 physisorption. Pd metal particles only covers the support surface, therefore the internal mass transfer can be excluded. The external mass

transfer tests were done by changing the stirring speed of the reaction. Additionally, H_2 transfer test from gas phase to liquid were carried out by changing the amount of catalysts. The mass transfer tests are concluded in Figure 14. The cyclohexene hydrogenation rate doesn't increase with the increasing stirring speed from 500 rpm to 600 rpm. Furthermore, the hydrogenation rate increases by two times as the catalyst amount doubles. Under the conditions of 70 °C 560 psi of H_2 and 500 rpm, cyclohexene hydrogenation is free from transfer limitations. The transport tests were also conducted under higher temperature, higher pressure of 100 °C, 600 psi of H_2 in heptane and the hydrogenation was free of external mass transfer.

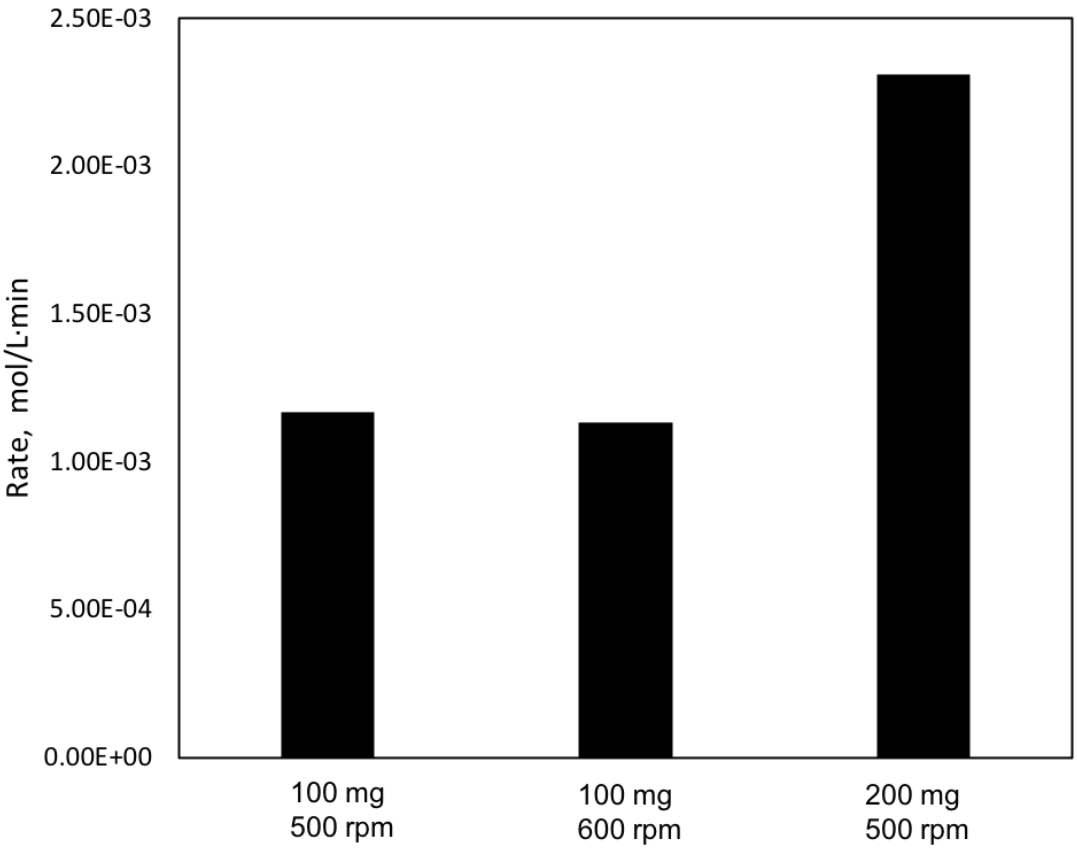

Figure 14. External mass transfer test. Reaction conditions: solvent heptane, H_2 pressure 560 psi, temperature 70 °C, cyclohexene initial concentration 0.42 M.

4.3.3 Kinetic models

The cyclohexene hydrogenation in three aprotic inert solvents were investigated. Under kinetic regime, the reaction rate differed when changing operating conditions. The Langmuir-Hinshelwood kinetic approach was utilized to model the solvent effect. The detailed discussions are presented in Chapter 2: 2.1 Langmuir-Hinshelwood Kinetic Model. The approach describes cyclohexene hydrogenation in the sequence which includes the crucial steps as surface adsorption, surface reaction and surface desorption. The mechanism is presented as follow:

$$H_2^g \leftrightarrow H_2^l \tag{53}$$

$$H_2^l + 2S \overset{K_{H_2}}{\longleftrightarrow} 2HS \tag{54}$$

$$E + S \overset{K_E}{\leftrightarrow} ES \tag{55}$$

$$ES + HS \overset{k_3}{\rightarrow} EHS + S \tag{56}$$

$$EHS + HS \overset{k_4}{\rightarrow} AS + S \tag{57}$$

$$AS \overset{K_A}{\leftrightarrow} A + S \tag{58}$$

$$Solvent + S \overset{K_S}{\leftrightarrow} SolventS \tag{59}$$

The sites balance could be derived using surface coverage, θ_i. There are two types site balance depending on the assumptions; one gives the site balance where all species adsorb on the same site as[40]

$$1 = \theta_v + \theta_{HS} + \theta_{ES} + \theta_{EHS} + \theta_{AS} + \theta_{SolventS} \tag{60}$$

The other separates the sites where reacting species and solvent adsorb on same site, yet H_2 adsorbs on different sites as[19, 83]

$$1 = \theta_{v1} + \theta_{HS1} \tag{61}$$

$$1 = \theta_{v2} + \theta_{ES2} + \theta_{EHS2} + \theta_{AS2} + \theta_{SolventS2} \tag{62}$$

The surface reaction is the rate determining step (RDS) and other steps are in quasi-equilibrium. However, depending on whichever step has the highest the activation energy, one of the two surface hydrogenation steps becomes irreversible rate determining step. Furthermore, much smaller H_2 atoms could alternatively be adsorbed on the high-coordinated three-fold fcc sites[84-87] without competing atop with other surface reacting species and solvents. Therefore, the possible kinetic models for the liquid-phase cyclohexene hydrogenation consist of four combinations. The scenarios are whether the first hydrogenation or the second hydrogenation is the rate determining step, H_2 is absorbed on the same sites or different sites as other surface species.

For liquid phase reaction, reactants are dissolved in solvents before reaching the catalyst surface. However, in non-ideal liquid phase reactions, the interactions between solvent-solute or solvent-solvent lead to the deviation from ideal solution mixture and could potentially affect the concentration of surface adsorbed species by influencing the tendency towards equilibrium. The thermodynamic activity, $a = \gamma C$, is needed to quantify the such interactions. Since liquid phase H_2 is in equilibrium with gas phase H_2 which activity coefficient is unity, only activity coefficients of cyclohexene and solvents are considered in the rate expression. In order to represent the non-ideal behaviors of the reaction system, the UNIQUAC estimation in ASPEN Plus was utilized for activity coefficient calculations due to the reliable application for wide range of mixtures[88]. The activity coefficients at infinite dilution for solutes in solvents are listed in Table 5. Reactant cyclohexene, as the solute, illustrated ideal mixture behaviors in methylcyclohexane and

decalin, because the activity coefficient $\gamma_E \approx 1$ at infinite dilution. Although cyclohexene in heptane showed non-ideality, the deviation from the ideal solution is much less comparing with the solvent mixture of decalin in heptane.

Table 5. Activity coefficient at infinite dilution.

Solute \ Solvent	Heptane	Methylcyclohexane	Decalin	Cyclohexene
Heptane	1	1.02	1.82	1.09
Methylcyclohexane	1.04	1	1.02	1.03
Decalin	1.51	1.03	1	0.97
Cyclohexene	1.06	1.02	0.97	1

The kinetic models of non-ideal liquid-phase cyclohexene hydrogenation are listed in Table 6. The reaction order with respect of H_2 and cyclohexene are analyzed. In the first scenario, H_2 adsorbs on the same sites as reactant cyclohexene and solvent, meanwhile the rate determining step is the first hydrogenation step. At very low H_2 partial pressure, the H_2 adsorption term $\sqrt{P_{H_2} K_{H_2}}$ in the denominator becomes much negligible than other adsorption terms yielding the rate expression to be 0.5^{th} order with respect of H_2 partial pressure. On the contrary, when the reaction is under high H_2 pressure, H_2 adsorption term becomes dominant so that other adsorption terms could be negligible. Therefore, the rate expression becomes -0.5 order with respect of H_2. The same approach is applied to cyclohexene concentration in the liquid phase to acquire the reaction order based on cyclohexene. Other scenarios are analyzed accordingly.

Table 6. Kinetic models and reaction orders.

	H_2 adsorption site	RDS	Rate expression	Reaction order			
				Low P_{H2}	High P_{H2}	Low a_E	High a_E
1	Same site	1st H	$r = \frac{k_3 K_E a_E \sqrt{P_{H_2} K_{H_2}}}{\left(1 + \sqrt{P_{H_2} K_{H_2}} + K_s a_s + K_E a_E\right)^2}$	0.5	-0.5	1	-1
2	Same site	2nd H	$r = \frac{k_4 K_{E*} K_E a_E \left(P_{H_2} K_{H_2}\right)}{\left(1 + K_E a_E + K_s a_s + \sqrt{P_{H_2} K_{H_2}} + K_{E*} K_E a_E \sqrt{P_{H_2} K_{H_2}}\right)^2}$	1	0	1	-1
3	Different site	1st H	$r = \frac{k_3 K_E a_E \sqrt{P_{H_2} K_{H_2}}}{(1 + K_E a_E + K_s a_s)\left(1 + \sqrt{P_{H_2} K_{H_2}}\right)}$	0.5	0	1	0
4	Different site	2nd H	$r = \frac{k_4 K_{E*2} K_E a_E \left(P_{H_2} K_{H_2}\right)}{\left(1 + K_E a_E + K_s a_s + K_{E*2} K_E a_E \sqrt{P_{H_2} K_{H_2}}\right)\left(1 + \sqrt{P_{H_2} K_{H_2}}\right)}$	1	0	1	0

4.3.4 True kinetic model and DFT studies

Among the four different scenarios in Table 6, there is only one circumstance that reflects the true kinetic of the surface reaction. Cyclohexene hydrogenation was conducted in three solvents under a wide range of H_2 pressure. The kinetic analysis unveils that third scenario when the H_2 adsorbed on different sites and the first hydrogenation is the rate determining step is the true kinetic on the Pd catalyst surface. The results are consistent with liquid phase hydrogenation of benzene over Pd[48].

The experimental data and the kinetic model fitting are presented in Figure 15. For experimental data in all solvents, hydrogenation rate increases with H_2 pressure. Activity in heptane is the highest followed by in methylcyclohexane and then in decalin. However, for all the solvents the rate maintains the same as H_2 pressure increased from 350 psi to 560 psi indicating the reaction order with respect of H_2 at high H_2 pressure is 0^{th} order. Therefore, the first scenario could be excluded since its kinetic illustrates a decrease in rate when H_2 pressure keeps increasing at high H_2 pressure operation conditions, yet other three scenarios would all reach 0^{th} order at high H_2 pressure.

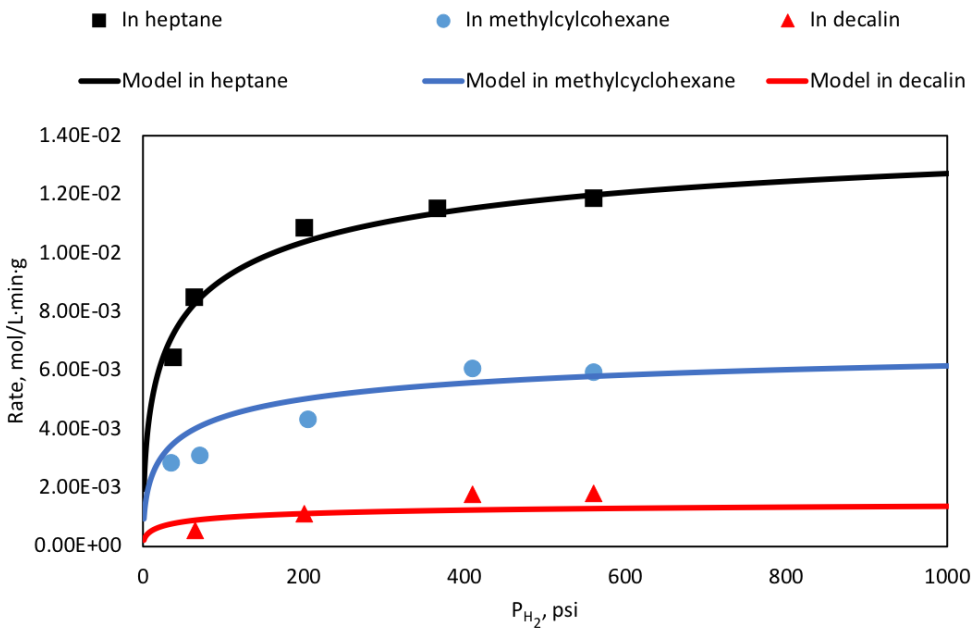

Figure 15. Hydrogenation as a function of H_2 pressure in three solvents fitted with the third scenario where hydrogen and reactant adsorb on different sites and the RDS is the first hydrogenation. Reaction conditions: temperature 70 °C, cyclohexene initial concentration 0.42 M.

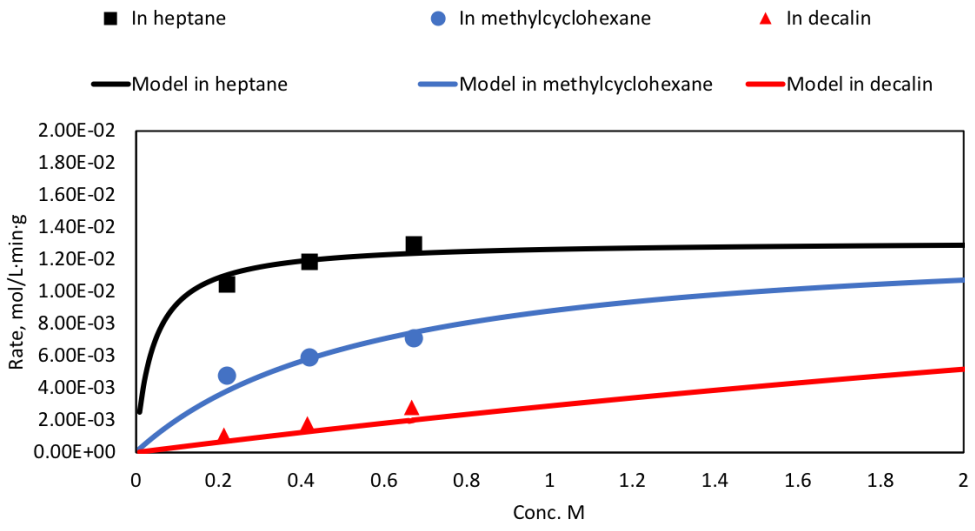

Figure 16. Hydrogenation as a function of cyclohexene concentration in three solvents fitted with the third scenario where hydrogen and reactant adsorb on different sites and the RDS is the first hydrogenation. Reaction conditions: temperature 70 °C, H_2 pressure 560 psi.

The kinetic based on cyclohexene concentration change was investigated by operating reactions at the fixed high H_2 pressure. The cyclohexene concentration was varied from 0.2 M to 0.7 M as shown in Figure 16. For all three solvents, the hydrogenation rate increases with cyclohexene concentration. The reaction orders based on cyclohexene are 0.18^{th}, 0.35^{th} and 0.83^{th} in heptane, methylcyclohexane and decalin respectively. However, the hydrogenation activity doesn't decrease with cyclohexene, which eliminates the possibility of the second scenario as the reaction order became -1^{th} when cyclohexene concentration increases.

So far, the first two scenarios have been excluded from the above interpretation. It's clear that H_2 dissociative adsorption doesn't happen on the same sites with reactant cyclohexene and solvent adsorption. Both circumstances exhibit the rate decrease as either the H_2 pressure or the cyclohexene concentration increase due to the competitive adsorption of H_2 with other surface adsorption species. On the contrary, hydrogenation reaction turns into 0^{th} order with respect of hydrogen pressure and cyclohexene concentration for the scenarios when H_2 is adsorbed on different sites that don't compete with other surface species. In fact, STM study has found that H atoms adsorb on the three-fold fcc sites[86] over Pd (111) surface.

Even at high H_2 pressure, as shown in both Figure 15 and Figure 16, there are still significant rate differences in three solvents. The observed solvent effect could be explained by the solvent adsorption term in the rate expressions. In scenario 4, the second hydrogenation is the rate determining step, the first hydrogenation of surface ES and HS is in quasi-equilibrium. Despite the H_2 dissociative adsorption on different sites, the adsorption term in the denominator includes not only surface cyclohexene and a

solvent, $1 + K_E a_E + K_s a_s$, but also the first hydrogenation product,$K_{E*2} K_E a_E \sqrt{P_{H_2} K_{H_2}}$. When reactions are carried out under high H_2 pressure, hydrogenation term $\sqrt{P_{H_2} K_{H_2}}$ becomes dominant. $K_{E*2} K_E a_E \sqrt{P_{H_2} K_{H_2}}$ overpowers $1 + K_E a_E + K_s a_s$ resulting in the situation that the rate expression under this condition should have be independent of solvent because the contribution from the solvent terms is insignificant than H_2. In other words, solvent effect should have disappeared and hydrogenation rate should have become the same in all solvents investigated in this study. As terms of scenario 3, the rate determining step is the first hydrogenation, the second hydrogenation step is in quasi-equilibrium. When $\sqrt{P_{H_2} K_{H_2}}$ overrules, the effect only takes place on the different sites that H_2 adsorbs on and the sites for cyclohexene and a solvent remain intact. In this way, the solvent adsorption term $K_s a_s$ does have the influence on the overall hydrogenation rate.

The experimental data was modelled utilizing the rate expression in scenario 3. The results are presented as smooth curves on Figure 15 and Figure 16. The H_2 reaction order at low pressure which ranges from 0 psi to 5 psi is found to be the 0.4^{th} order and is closer to the 0.5^{th} order in the scenario 3. Reaction order decreases with H_2 pressure and reaches 0^{th} order in all solvents at high H_2 pressure. As far as reaction order on cyclohexene under low concentration yet high H_2 pressure, the model illustrates the 0.7^{th}, 0.9^{th} and 1^{th} order based on reactions in heptane, methylcyclohexane and decalin respectively. The reaction order approaches to the 0^{th} order as cyclohexene concentration increases in three solvents eventually. The reaction orders acquired from kinetic model is consistent with Gonzo and Boudart's kinetic studies[36] on cyclohexene hydrogenation. At atmospheric conditions, the cyclohexene hydrogenation has also been found to be the 0.5^{th} order with respect of H_2

partial pressure and 0^{th} order based on cyclohexene concentration. The kinetic model predicts that the solvent effect will gradually disappear as the cyclohexene concentration keeps increasing.

The kinetic studies have illustrated the cyclohexene hydrogenation surface mechanism, which H_2 adsorbs on different sites and the rate determining step is the first hydrogenation reaction. This was further confirmed by our DFT calculations (Appendix: DFT calculations in Chapter 4). As shown in the energy diagram of the hydrogenation of cyclohexene on Pd(111) in Figure 17, the energy barrier for the first hydrogenation step of cyclohexene is calculated to be 94 kJ/mol, which is about 30 kJ/mol higher than the energy barrier for the second hydrogenation step on the clean Pd(111) surface, confirming that the first hydrogenation step is likely to be the rate determining step. This also holds at high H coverage, as shown in the energy diagram on the Pd(111) covered with 7/9 ML H* in Figure 17. On the 7/9 H* covered Pd(111) surface, the energy barrier for the first hydrogenation step of cyclohexene is calculated to be 88 kJ/mol, which is slightly lower than that on the clean Pd(111) surface, but is still much higher than the barrier for the second hydrogenation step (45 kJ/mol). This agrees with the experiments that the rate expression in scenario 3 in Table 6 describe the kinetics of the hydrogenation of cyclohexene is in a wide range of hydrogen pressure of 30-560 psi.

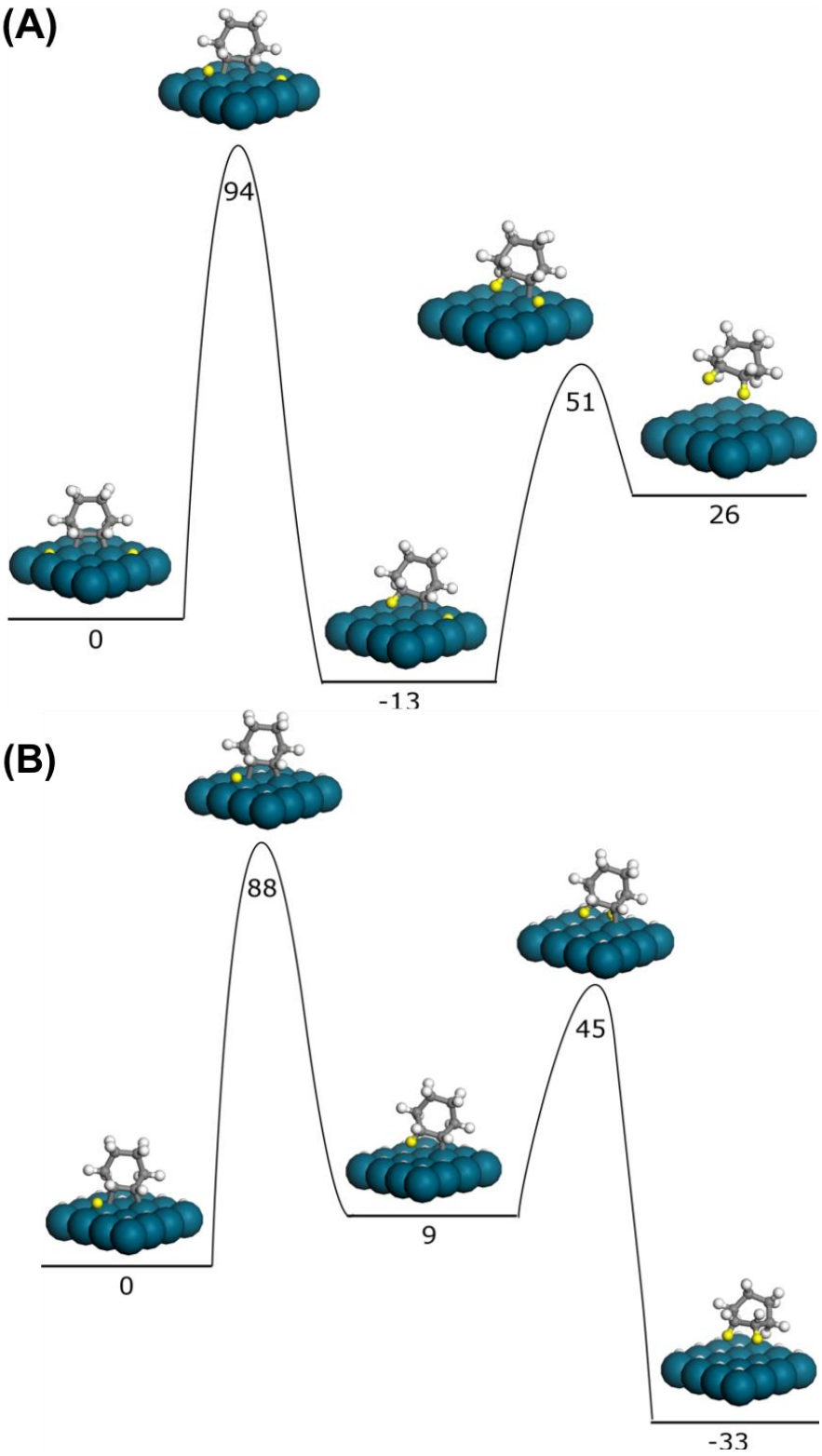

Figure 17. DFT calculated potential energy diagram for the hydrogenation of cyclohexene on clean Pd (111).

4.3.5 Solvent effect and solvent non-ideality

The observed solvent effect is mainly due to the solvent competitive adsorption with cyclohexene. The kinetic parameters acquired from the fitting in Table 7 further demonstrates adsorption constants on the catalyst surface. The strongest adsorption comes from reactant cyclohexene followed by the solvent decalin. Heptane and methylcyclohexane have a much weaker adsorption on the catalyst surface compared with cyclohexene and decalin. With the weakest interactions with active sites of heptane, catalyst surface is covered mostly by cyclohexene and hydrogen. The adsorption of cyclohexene and the three solvents decalin, methylcyclohexane and heptane were calculated. Their adsorption modes are shown in Figure A1 and the adsorption energies without the consideration of vdw interactions were listed in Table 8. It shows that the order of the adsorption energies of cyclohexene and the three solvents is consistent with the experiment fitted adsorption constants that cyclohexene > decalin > cyclohexane > heptane.

Table 7. Kinetic model fitting parameters.

	In heptane	In methylcyclohexane	In decalin
k_3, mol/L·min·g	0.022	0.022	0.022
K_{H_2}, psi^{-1}	0.018	0.018	0.018
K_E, L/mol	5.621	5.621	5.621
$K_{solv\ Hep}$, L/mol	0.000		
$K_{solv\ Ma}$, L/mol		0.491	
$K_{solv\ Dl}$, L/mol			4.370

Table 8. DFT calculated adsorption energies of cyclohexene, decalin, methylcyclohexane and heptane without vdw interactions.

	Cyclohexene	Heptane	Methylcyclohexane	Decalin
E_{ad} , kJ/mol	-30	-23	-16	-11

To further demonstrate the solvent competitive adsorption, cyclohexene hydrogenation was conducted in co-solvent mixture. The primary solvent was heptane since the adsorption was negligible among all the solvents, and any additional solvent could reveal the solvent effect if it had stronger adsorption. Therefore, the secondary solvent was added to create a solvent mixture with different compositions. The results are plotted in Figure 18. With the additional solvent, the hydrogenation rate decreases in both solvent mixtures. Since the adsorption constant for decalin is 4.370 L/mol and the 0.491 L/mol for methylcyclohexane, the rate decrease when adding decalin is drastically even with a small amount of decalin.

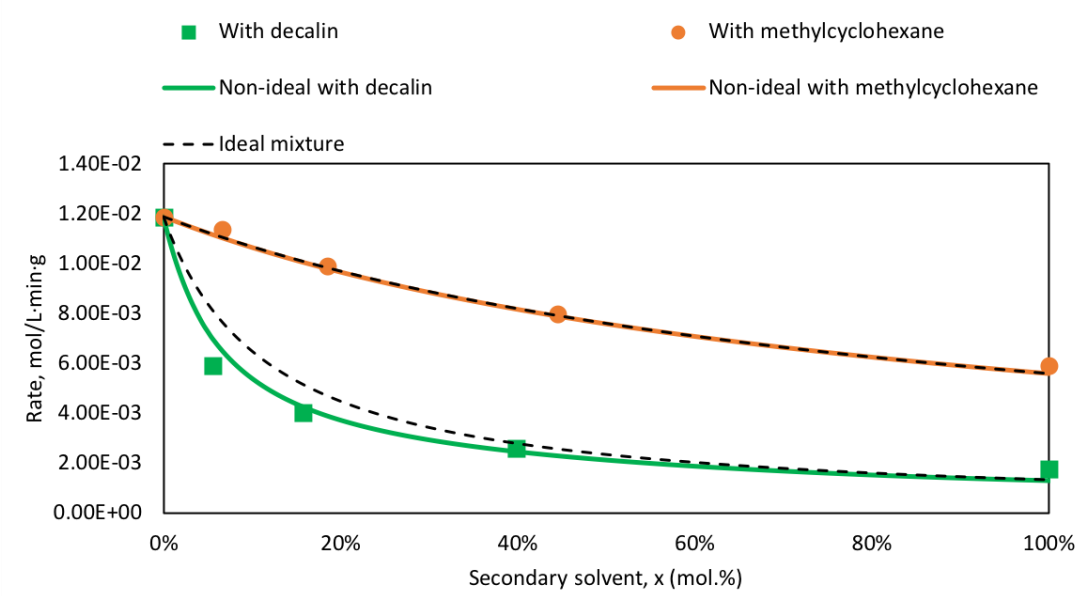

Figure 18. Hydrogenation in co-solvent mixtures. Reaction conditions: temperature 70 °C, H_2 pressure 560 psi, cyclohexene initial concentration 0.42 M.

The present of decalin gave rise to the strong adsorption that essentially altered the catalyst surface coverage by competing with other surface species. The comparisons of surface coverage under same reaction conditions is listed in Table 9. The calculations were

done by applying the kinetic parameters achieved in Table 7 and the reaction conditions were chosen to be at the 560 psi of H_2 and 0.42 M of cyclohexene. Gonzo and Boudart[36] have unveiled that reaction rate doesn't change with solvents H_2 solubility in cyclohexene hydrogenation over Pd catalysts. Therefore, the surface coverage and the vacant sites for H_2 adsorption are the same for all solvents since H_2 adsorbs on different sites that don't compete with other surface species. In pure solvents, cyclohexene surface coverage varies with solvents. In heptane, 71% of the surface is all covered with reactant cyclohexene since heptane doesn't absorb on the surface. The hydrogenation rate is directly related to the surface coverage of cyclohexene and hydrogen. Higher coverage of cyclohexene leads to the better hydrogenation activity. However, when 5 mol.% of decalin was introduced, the hydrogenation decreased rapidly. The surface coverage of cyclohexene changes from 71%, in pure heptane, to 43%, in decalin and heptane mixture. Decalin occupies the surface instantly. The presence of decalin competes mostly with cyclohexene over available active sites and causes the rate decrease. Comparing with the rate decrease in 5 mol.% methylcyclohexane in heptane, much weaker adsorption of methylcyclohexane only competes little and keeps 67% of cyclohexene still on surface. The rate decreases in methylcyclohexane and heptane mixture, but not as drastically as in decalin and heptane mixture.

Table 9. Surface coverage in different solvents[a].

	Surface Coverage				
	heptane	methylcyclohexane	decalin	5 mol.% decalin[b]	5 mol.% methylcyclohexane[b]
H_2	0.76	0.76	0.76	0.76	0.76
vacant site 1	0.24	0.24	0.24	0.24	0.24
cyclohexene	0.71	0.33	0.12	0.43	0.67
Primary solvent	0	0.52	0.85	0	0
Secondary solvent				0.39	0.05
vacant site 2	0.29	0.14	0.03	0.18	0.28

[a] Reaction conditions are 70 °C, H_2 pressure 560 psi, cyclohexene initial concentration 0.42 M
[b] Co-solvent mixture and primary solvent is heptane

For reactions utilizing one solvent, the interactions between cyclohexene and a solvent are not very strong. Because under the reaction conditions, the activity coefficient of both cyclohexene and any solvent listed in Table 5 are all close to 1, which is similar to ideal solution. The influence on the hydrogenation rate caused by solvent reactant interactions are negligible. However, for reactions involving two solvents mixture, the non-ideality of solution mixture incurred by strong interactions between two solvents can be phenomenal.

Thermodynamic property such as solvent activity also plays an important role in liquid-phase hydrogenation. The decalin-heptane mixture exhibits highly non-ideality with $\gamma_{decalin} = 1.51$ and $\gamma_{heptane} = 1.82$ at infinite dilution implying that either one shows positive deviation from Raoult's law[89]. Since the liquid bulk phase is not only in equilibrium with gas phase but also in equilibrium with catalyst surface, the solid phase, the total number of surface species could be affected by thermodynamic tendency towards equilibrium. When decalin is added in heptane, the solvent interactions repulse decalin away from the liquid bulk phase to the catalyst surface. Therefore, the surface

concentration of decalin is increased due to the thermodynamic tendency towards equilibrium.

A series of activity coefficients with different mole compositions in two solvents mixtures were calculated by ASPEN Plus and were applied in the kinetic model. The results are plotted in Figure 18. The dash lines represent the kinetic in ideal mixture and the smooth lines represent the kinetic in non-ideal mixture. It's clear to spot that thermodynamic activity greatly affects cyclohexene hydrogenation rate in decalin-heptane mixture. The strong interactions are unfavorable for decalin to form a stable mixture with heptane. Instead, decalin is tend to go to the catalyst surface to compete active sites with cyclohexene. Therefore, the kinetic model of ideal mixture that applies concentration instead of activity doesn't describe the experimental data well enough because the catalyst surface has more decalin to compete sites with cyclohexene than in ideal mixture. The actual hydrogenation rate in the mixture of 0-40 mol.% compositions illustrated much less reactivity. Since $\gamma_{decalin}$ decreases with decalin composition in the mixture, the more decalin in the mixture, the smaller $\gamma_{decalin}$ becomes. By the time decalin becomes the primary solvent and heptane is the secondary solvent, $\gamma_{decalin}$ approaches 1. Although $\gamma_{heptane}$ is larger than $\gamma_{decalin}$, the extreme weak adsorption of heptane on the catalyst surface doesn't compete sites with cyclohexene. As was measured in 40 mol.% decalin-heptane mixture, the kinetic started acting like it was acquired in ideal mixture. On the other hand, methylcyclohexane-heptane mixture activity coefficients are close to unity with $\gamma_{methylcyclohexane} = 1.04$ and $\gamma_{heptane} = 1.02$ at infinite dilution. The mixture

doesn't have much deviation from ideal solution. Therefore, kinetic using ideal mixture is able to capture the experimental data, and the non-ideal kinetic almost overlaps with it.

4.3.6 Kinetic and thermodynamic parameters

Thermodynamic parameters such as entropy and enthalpy change during adsorption and reaction are readily to be fitted with kinetic modelling. The experimental data of cyclohexene hydrogenation were collected under different temperatures ranging from 40 °C to 100 °C with the H_2 pressures of 600 psi and 100 psi in heptane. Therefore, the rate expression was simplified as:

$$r = k_3 \times \frac{K_E a_E}{1 + K_E a_E} \times \frac{\sqrt{P_{H_2} K_{H_2}}}{1 + \sqrt{P_{H_2} K_{H_2}}} \tag{63}$$

The rate constant k_3 and adsorption equilibrium constant K_i can be derived from transition state theory[26]:

$$k_3 = N_s \frac{k_B T}{h} e^{\frac{\Delta S^{\ddagger}}{R}} e^{-\frac{\Delta H^{\ddagger}}{RT}} \tag{64}$$

$$K'_i = e^{\frac{\Delta S_{ads}}{R}} e^{-\frac{\Delta H_{ads}}{RT}} \tag{65}$$

where $N_s, \Delta S^{\ddagger}, \Delta H^{\ddagger}$ are catalyst site density, entropy and enthalpy change of activation. k_B, h, R are Boltzmann constant, Planck constant and gas constant respectively. $\Delta S_{ads}, \Delta H_{ads}$ in adsorption equilibrium constant represent the entropy change of adsorption and heat of adsorption. K'_i is dimensionless thermodynamic adsorption constant, however the adsorption equilibrium constant K_i in the rate expression has a unit with a respect of concentration or pressure. The standard state of concentration or pressure was applied for each case.

Adsorption equilibrium constant K_i decreases with temperature. Therefore, surface coverage of reactants is approaching to a full coverage under low temperature and high pressure/concentration of reactants. The adsorption terms would have less impact on the overall reaction rate when they approach to 1. On the contrary, higher temperature and less reactants decrease the surface coverage and give more contributions to the rate expression. To acquire better fitting for cyclohexene and H_2 adsorption parameters, 80 °C to 100 °C reaction temperatures, and less amount of reactants, 0.17 M for cyclohexene, 100 psi for H_2, were applied. As terms of rate constants, the opposite reaction conditions were carried out. the reaction temperatures were decreased to 40 °C - 60 °C and the reactants were increased to 0.42 M and 600 psi for cyclohexene and H_2 respectively.

Eight fitting parameters including ΔS of adsorption/reaction, and ΔH of adsorption/reaction are solved with experimental measurements under different temperatures, pressures and concentrations. The data fits well with the kinetic model as shown in Appendix B (Figure B 1). When ΔS varies during mathematical fitting, the ΔH also produces corresponding values to match experimental data. The fitting parameters and their fitting variations derived from multiple data sets are presented in Table 10.

Entropy of adsorption

Entropy of adsorption ΔS of cyclohexene and hydrogen are demonstrated in Table 10. The entropy change during adsorption onto Pd surface for cyclohexene was referred to liquid phase cyclohexene, which entropy is 216 J/mol·K under reaction temperatures[90]. Hydrogen adsorption was referred to gas phase hydrogen and its entropy is 131 J/mol·K[91]. Combing kinetic measurements and statistical mechanics analysis, the

entropy of adsorption for cyclohexene is determined to be -143 ± 19 J/mol·K and therefore the adsorbed cyclohexene retained 75 ± 14 J/mol·K on the surface. Hydrogen adsorption unveiled a large entropy change, -108 ± 12 J/mol·K, compared to free hydrogen in the gas phase reserving only 23 ± 12 J/mol·K after adsorption.

Table 10. Kinetic and thermodynamic parameters from experimental fittings.

	ΔS, J/mol·K	ΔH, kJ/mol	α_{Hads}, kJ/mol
k_3	-2±1	81±2	
K'_E	-143±19	-75±14	22±6
K'_{H_2}	-108±12	-41±7	8±1

The entropy of adsorption could be estimated from statistical mechanics, although reasonable assumptions were made in order to provide a range of entropy change based on the degree of freedom (DOF) of the adsorbed species. The equations and discussions are demonstrated in Chapter 2: 2.2 Statistical Thermodynamics. The thermodynamic equilibrium constant is derived from statistical thermodynamics, which involves partition functions for both adsorbed species and free molecules as follows [24, 26, 27, 68]:

$$K'_i = \frac{Q'''_{ads}}{Q'''_{gas/liquid}} e^{-\frac{\Delta H_{ads}}{RT}} \tag{66}$$

$$Q'''_i = q_{t,i} q_{r,i} q_{v,i} \tag{67}$$

$$A_{ads} = \frac{q_{t,ads} q_{r,ads} q_{v,ads}}{q_{t,gas/liquid} q_{r,gas/liquid} q_{v,gas/liquid}} \tag{68}$$

Where q_t, q_r, q_v are the translational partition function, rotational partition function and total vibrational partition function respectively. The ratio of the partition functions for adsorbed state and the gas/liquid phase state is the pre-exponential factor A_{ads} .The following equations were used to calculate partition function of each mode for polyatomic molecules:

$$q_t^{1DOF} = l\frac{(2\pi m k_B T)^{1/2}}{h} \tag{69}$$

$$q_r^{3DOF} = \frac{1}{\sigma}(\frac{8\pi^2 k_B T}{h^2})^{3/2}\sqrt{\pi I_A I_B I_C} \tag{70}$$

$$q_v = \frac{1}{1 - e^{-h\nu/k_B T}} \tag{71}$$

Where l is the length that any particle of mass m moves in one dimension. σ is the symmetry factor and I_A, I_B, I_C are moments of inertia for a larger molecules along the three principal axes. ν is the vibrational frequency.

For cyclohexene in the liquid phase, one molecule moves with 3 DOF of q_t inside a volume V, which can be calculated by molecular weight and cyclohexene density ρ:

$$V = \frac{M.W.}{\rho}\frac{1}{N_A} \tag{72}$$

Where N_A is the Avogadro constant. The symmetry number σ for cyclohexene[92] in rotational partition function Eq.(70) is 2. I_A, I_B are moments of inertia around the axes on the same plane as cyclohexene and I_C is produced perpendicularly to the plane. The values[93] are 106.6 uÅ^2, 111.2 uÅ^2, 197.2 uÅ^2. The vibrational partition function Eq. (71) can be approximated as 1 since the wavenumbers of cyclohexene are larger.

For adsorbed cyclohexene on the Pd site, the most stable adsorption structure has been shown to be π bonding on a top site (Figure A2) since the heat of adsorption has the lowest value of -134 kJ/mol among all the other adsorption geometries. Upon adsorption, cyclohexene can diffusion on the surface two dimensionally with an area A, which can be estimated by a square with a length of l. Since the top site adsorption has the local minima on the potential energy surface, it's reasonable to assume that the translational length that

adsorbed cyclohexene diffuse on a (111) surface from a top site to its adjacent top site is the diameter of Pd atom, which rounds up to 3 Å. When the surface coverage of cyclohexene increases, the attractive-repulsive interaction hinders the mobility of cyclohexene and therefore the translational length decreases. As for the rotational partition function of adsorbed cyclohexene, the π bonding adsorption geometry leads to only 2 DOF or less. The axes of rotation are from the same plane as the adsorbed cyclohexene while its perpendicular axe has been restricted. However, one of the axes has shifted from the center of cyclohexene to the C=C axe compared with liquid phase cyclohexene. The moments of inertia produced under the adsorbed state needs to be recalculated using the point mass of cyclohexene and the distance to C=C axe[94]. The rotational DOF is also influenced by the surface coverage and eventually adsorbed cyclohexene becomes 0DOF. The vibrational partition function $q_{v,ads}$ can be written as $q_{v,gas/liquid}q_{v,C-Pd}$. Cyclohexene obtains extra vibrations upon adsorption on Pd and it is due to the formation of C-Pd bonds. The study of ethylene adsorption on Pd (111)[95] has unveiled that the vibrational frequencies for C-Pd are 341 cm^{-1} and 533 cm^{-1}. The estimation of the vibrational partition function $q_{v,C-Pd}$ has utilized 400 cm^{-1} for both C. Therefore, combing Eq. (69) - (71), Eq. (68) for cyclohexene adsorption is:

$$\boldsymbol{A_{ads}(T = 343K) = \frac{q_{t,ads}^{2DOF} q_{r,ads}^{2DOF} q_{v,gas/liquid} q_{v,C-Pd}}{q_{t,liquid}^{3DOF} q_{r,liquid}^{3DOF} q_{v,liquid}}}$$

$$\boldsymbol{= \frac{(l \times 9.61 \times 10^{10})^2 \times (37.80 \times 39.66) \times (1.23 \times 2)}{1.68 \times 10^{-28}(m^3) \times (9.61 \times 10^{10})^3 (m^{-3}) \times (34.42 \times 39.66 \times 52.81)}}$$

The A_{ads} is the pre-exponential factor that serves as the entropy term in equilibrium constant in Eq. (65). There are two variables that make major contributions to the entropy change: the translational length and rotational DOF upon adsorption. The entropy of

adsorption has been plotted in Figure 19. More mobility of adsorbed cyclohexene has on the surface, longer the translational length and higher DOF of rotations it retains. Therefore, as depicted in Figure 19 (a), when the adsorbed cyclohexene has the ability to diffuse from one top site to another with a length of 3Å as well as it rotates with two axes, the entropy of adsorption is -74 J/mol·K retaining 143 J/mol·K. By the time when adsorbed cyclohexene molecules are restricted to move and rotate freely, 0.5 Å and 0DOF of rotation for instance, the entropy of adsorbed cyclohexene only has 53 J/mol·K. The experimental result emerges in the range with a value of -143 ± 19 J/mol·K, which indicates that the molecule processes 74 ± 19 J/mol·K after adsorption. Campbell and Sellers[96] investigated entropies of adsorbed alkanes on Pt (111) and MgO(100). It has been demonstrated that the entropies are around 2/3 of the gas and it is due to the freeze of motion in the z direction. The possibilities shown in Figure 19 (b) reveal that the entropy of adsorbed alkene can be less than 2/3 of the original state, and it is around 1/3 of the liquid cyclohexene in the experiment. The much stronger bonding of alkenes on metal surface leads to restrictions on not only z direction, but also x, y directions along with rotations.

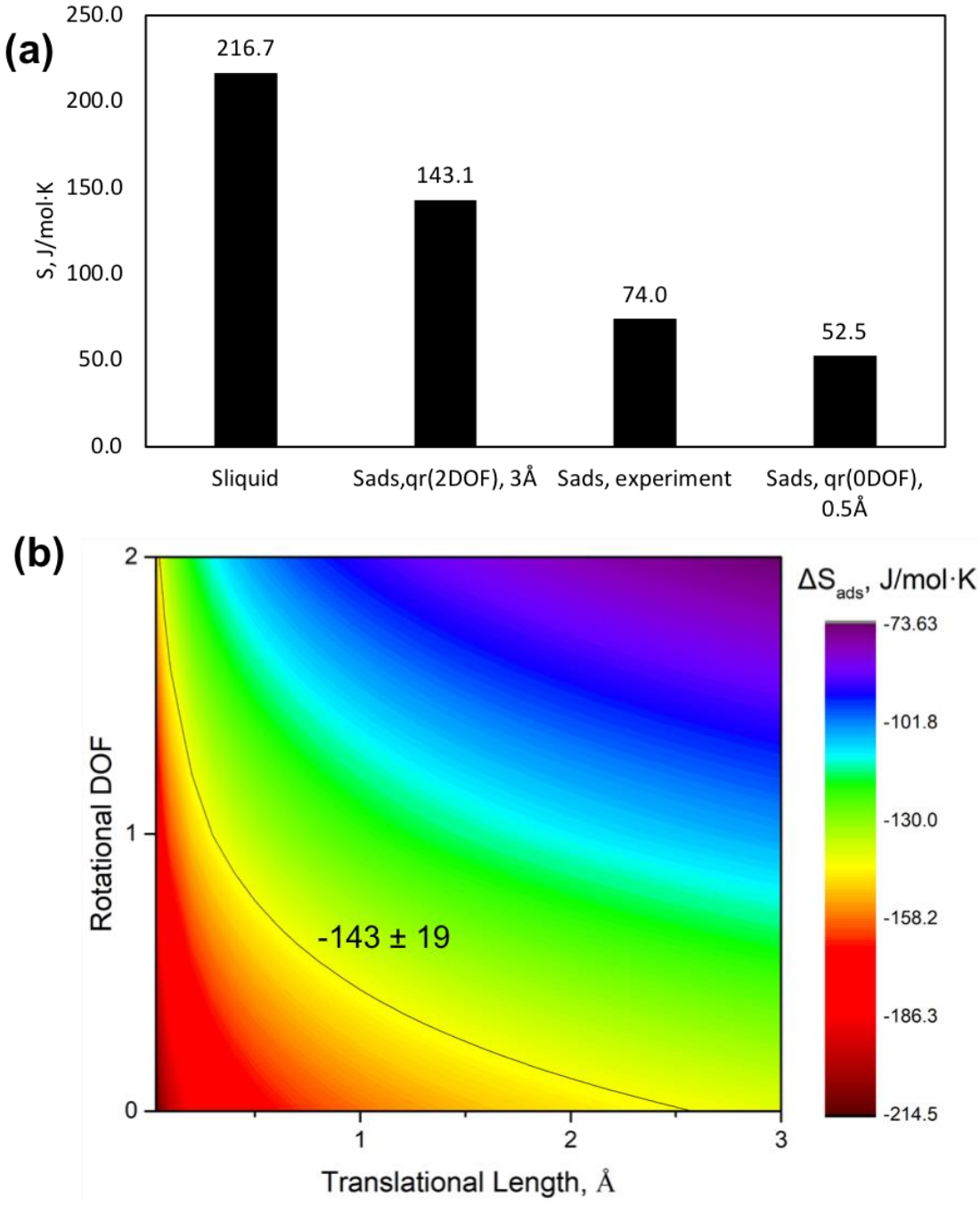

Figure 19. (a) Entropy of cyclohexene in liquid phase and on surface combined with scenarios at different translational lengths and rotational DOF, with experimental data. (b) Entropy of adsorption as a function of translational length and rotational DOF. The solid line is the value from kinetic fitting.

Similarly, the pre-exponential factor for gas phase H_2 adsorption is derived using partition functions. The kinetic fitting for its entropy of adsorption is presented in Table 7. Adsorbed hydrogen atoms only possess translational degree of freedom and newly formed H-Pd vibrations on surface while rotations have been completely restricted. H diffusion barrier on Pd (111) has been utilized to estimate the translational DOF. The preference sites for H_2 adsorption on Pd (111) are fcc hollow sites. The lowest energy pathway for the diffusion of dissociated H is to pass through the bridge site and reach to a hcp site[87, 97]. The energy barrier is 12 kJ/mol, while the highest energy pathway that going through atop site is as high as 47 kJ/mol[87]. Therefore, diffusion over Pd (111) is hindered in some extent. The distance between a fcc site to a bridge site is 0.8 Å, to a hcp site is 1.6 Å. The translational length l for adsorbed H is no more than 1.6 Å. Gas phase H_2 molecule moves in a volume of V, which can be approximated using ideal gas law at the standard pressure. For rotational partition function, since the adsorbed H forms three H-Pd with the adjacent Pd atoms, the only rotational DOF has been restricted after adsorption. However, diatomic H_2 has 2 DOF along the axes and q_r at 343 K equals 2.61[24]. The vibrational partition functions for both gas phase H_2 and adsorbed H are assumed to be the same. Therefore, the pre-exponential factor for H_2 dissociative adsorption is:

$$\boldsymbol{A_{ads}(T = 343K)} = \frac{(\boldsymbol{q_{t,ads}^{2DOF} q_{v,ads}})^{\boldsymbol{2}}}{\boldsymbol{q_{t,gas}^{3DOF} q_{r,gas}^{2DOF} q_{v,gas}}} = \frac{[(\boldsymbol{l \times 1.50 \times 10^{10}})^{\boldsymbol{2}}]^{\boldsymbol{2}}}{\frac{\boldsymbol{k_B T}}{\boldsymbol{p^0}}(\boldsymbol{m^3}) \times (\boldsymbol{1.50 \times 10^{10}})^{\boldsymbol{3}}(\boldsymbol{m^{-3}}) \times \boldsymbol{2.61}}$$

The major contribution for the entropy of adsorption lies in the translational partition function since adsorbed hydrogen atoms don't have rotational DOF. Solving for the entropy of adsorption, the results are plotted in Figure 20. Upon adsorption, surface H

atoms reserve only little entropy since its rotation axe is no long valid for fcc sites adsorption and diffusion on the Pd (111) is also greatly limited by the high energy barrier. If a H atom moves from a fcc site to a hcp site through a bridge site, the translational length is 1.6 Å. Therefore, the entropy of adsorption is -89 J/mol·K keeping 42 J/mol·K with it. Since the energy barrier for diffusion is not barrierless, diffusing to a bridge site requires more energy. In this case, for a H atom that moves along a distance of 0.6 Å, the entropy of adsorption is -123 J/mol·K and the its entropy is now merely 8 J/mol·K. The experimental fitting in Table 7 illustrates that upon adsorption, H still has 23 ± 12 J/mol·K and the entropy of adsorption is -108 ± 12 J/mol·K. The kinetic fitting is consistent with the H_2 adsorption study using a PC isotherms over Pd black and the entropy of adsorption is around -90 J/mol·K[98].

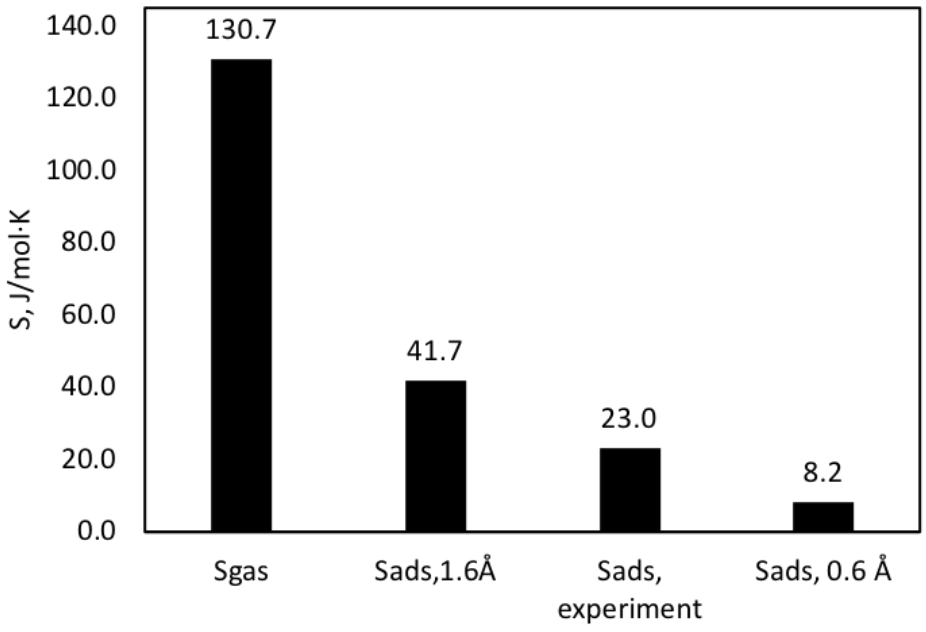

Figure 20. Entropy of hydrogen in gas phase and on surface combined with scenarios at possible translational lengths with experimental data.

Enthalpy of adsorption

Statistical thermodynamics provide reasonable analysis on entropy of adsorption ΔS for both cyclohexene and hydrogen on Pd (111). Since a thermodynamic equilibrium constant in Eq. (65) consists of two terms, $e^{\frac{\Delta S_{ads}}{R}}$ and $e^{-\frac{\Delta H_{ads}}{RT}}$, heat of adsorption ΔH is acquired once the entropy of adsorption has been determined. Adsorption over metal surface such as benzene on Pt (111)[99], benzene on Pd (111)[100], cyclohexene on Pt (111)[101], H on Pd (111)[102] have demonstrated to be coverage dependent. The Temkin isotherm takes into account of the surface coverage effect on heat of adsorption, which would decrease linearly with coverage[103]. Therefore, kinetic model on enthalpy of adsorption employed the equation as follows

$$\Delta H_{ads} = \Delta H_{ads}^{0} + \alpha\theta \tag{73}$$

Where ΔH_{ads}^{0} represents the heat of adsorption on a clean surface. α is the fitting parameter indicating the unit change in heat of adsorption per surface coverage and has a unit of J/mol.

The heat of adsorption and the fitting parameters for cyclohexene and hydrogen derived from kinetic fittings are presented in Table 10. On clean Pd surface, the heat of adsorption for cyclohexene is -75 ± 14 kJ/mol, while the heat of adsorption for hydrogen is -41 ± 7 kJ/mol. As surface coverage increases, cyclohexene adsorption energy increases and the fitting parameter α is 22 ± 6 kJ/mol, indicating the heat of adsorption for cyclohexene on a fully covered Pd surface becomes 53 kJ/mol. On the other hand, hydrogen adsorption energy doesn't increase as much as that of cyclohexene with the surface coverage. The fitting parameter α is 8 ± 1 kJ/mol, yielding 33 kJ/mol as the heat of

adsorption for hydrogen on a fully covered surface. Experimental fittings are all smaller than DFT calculations. As depicted in Figure A2, heat of adsorption of cyclohexene on clean Pd(111) is -134 kJ/mol. Since the calculation has considered the vdw interactions of the molecule with the Pd surface, the value might have overestimated the actual heat of adsorption. Without the vdw interactions, the heat of adsorption of cyclohexene on Pd(111) has been calculated to be -30 kJ/mol in Table 8. Therefore, the result from experiment fitting is reasonable.

Entropy and enthalpy of reaction activation

Rate constant k_3 containing entropy change of activation and enthalpy of reaction activation acquired from experimental fitting is listed in Table 10. The entropy of activation is -2 ± 1 J/mol·K. Since the first hydrogenation is the rate-determining step, the initial states are adsorbed cyclohexene and adsorbed hydrogen atom. The negative entropy of activation illustrates that entropy at the transition state decreases after surface reacting species are activated. An adsorbed H atom is combined with C=C of cyclohexene, some entropy decrease is anticipated. On the other hand, a positive entropy of activation is also possible when activated complex C_6H_{11} gain a certain amount of freedom at the same time because the bonding strength between it and the catalyst should decrease as the ring becomes more saturated with hydrogen[104]. However, the small and negative entropy of activation from the experiment fitting indicates a slightly stronger binding at the transition state. It is reasonable to consider the adsorbed activated complex as an immobile molecule, which is bonded to the catalyst surface.

The measured enthalpy of activation is 81 ± 2 J/mol. The kinetic model considers that the RDS is the first hydrogenation step. The energy barrier for the first hydrogenation of cyclohexene is therefore 81 ± 2 kJ/mol. The result is also in agreement with DFT calculations in Figure 17. The first hydrogenation has the energy barrier of 94 kJ/mol, which is about 30 kJ/mol higher than the energy barrier for the second hydrogenation step on the clean Pd(111) surface. On the 7/9 H* covered Pd(111) surface, the energy barrier for the first hydrogenation step of cyclohexene is calculated to be 88 kJ/mol, which is slightly lower than that on the clean Pd(111) surface, but is still much higher than the barrier for the second hydrogenation step (45 kJ/mol).

4.4 Conclusion

Cyclohexene hydrogenation in three inert nonpolar solvents, heptane, methylcyclohexane and decalin was investigated in a wide range of reaction operation conditions over 0.25% Pd/α-Al_2O_3. Langmuir-Hinshelwood kinetic models are applied for the reaction and four kinetic rate expressions can be derived depending on whether the H_2 adorbs on the same sites with cyclohexene and solvent and which hydrogenation step is the rate determining step.

By varying H_2 pressure from 30 psi to 560 psi and cyclohexene initial concentration at 70 °C, solvent effects are greatly observed. Hydrogenation reaction is the fastest in heptane followed by in methylcyclohexane and then the slowest in decalin. The reaction order analysis indicates that H_2 dissociative adsorption happens on the different sites than cyclohexene and solvent adsorption, as well as the rate determining step is the first hydrogenation step. The reaction order based on H_2 changes from 0.5^{th} order to 0^{th} order in low H_2 pressure and high H_2 pressure respectively. Furthermore, the reaction order of

cyclohexene starts at 1^{th} order and approaches 0^{th} order with cyclohexene concentration in all solvents eventually.

The observed solvent effect in this study is caused by solvent competitive adsorption, which alters the surface coverage of reactant cyclohexene. Besides the strongest cyclohexene adsorption on catalyst surface, decalin has the second highest adsorption followed by methylcyclohexane. Heptane has the weakest adsorption on catalyst surface. Surface coverage of reactant cyclohexene is relatively low in decalin because decalin competes sites with cyclohexene. Moreover, adding the second solvent into heptane results in the rate decrease due to the decrease in surface coverage of cyclohexene.

Additionally, thermodynamic activity in non-ideal solvent mixture plays an important role in liquid-phase hydrogenation. Reactions in only one solvent illustrate negligible deviation from ideal solution since activity coefficients are close to unity. However, the co-solvent decalin-heptane mixture is highly non-ideal. The interactions between decalin and heptane tend to drive decalin onto the catalyst surface and compete sites with cyclohexene. The non-ideality of the mixture thermodynamically increases the surface solvent species that leads to further decrease in reactivity.

Entropy and enthalpy change determine the equilibrium and reaction constants. Derived from statistic thermodynamic, entropy of adsorption relates to the translational, rotational and vibrational partition functions of free molecules and adsorbed species. Adsorbed cyclohexene could have the up to 3 Å translational mobility and 2 DOF of rotations on the surface, yielding the entropy of adsorption of -143 ± 19 J/mol·K upon adsorption. On the other hand, adsorbed hydrogen has been restricted much more on the

surface with the entropy of adsorption of -108 ± 12 J/mol·K. The statistical thermodynamic analysis unveils a reasonable range to provide guidance for kinetic fittings so that the corresponding heat of adsorption obtained from kinetic fittings has physical meaning and is comparable with DFT studies. The Enthalpy change during adsorption, heat of adsorption, is the coverage dependent. On clean surface, heat of adsorption for cyclohexene and hydrogen is -75 ± 14 kJ/mol and -41 ± 7 kJ/mol respectively. The energy increases with surface coverage linearly. When surface is fully covered with adsorbed cyclohexene or hydrogen, the heat of adsorption becomes 53 kJ/mol for cyclohexene and 33 kJ/mol for hydrogen.

Acknowledgements

This work was supported by the U.S. Department of Energy, DOE/EPSCOR (Grant DESC0004600).

Chapter 5: Mechanistic Role of Water in Aqueous Phase Furfural Hydrogenation on Pd Catalysts*

5.1 Introduction

In liquid-phase heterogeneous catalysis, reactants adsorb and react at the active sites in the presence of the solvent, which may have multiple and distinct effects rather than traditionally dissolving chemicals and transferring heat. Multiple effects may work simultaneously, and the dominant effect varies among different reactions. Solvent may change the kinetics of the reactions when the rate-determining steps involve a solvated transition state[34, 105]. The aqueous phase can also affect the molecular adsorption by redistributing the electrons at the solid/water interface[63]. Additionally, water may also directly participate the reaction, like in hydrogen-assisted activation of CO[53] and O_2[106] and in alcohol oxidation via hydroxide ions[107]. Moreover, the expanding utilization of water/oil biphasic system for reactions has depicted simultaneously separation of the water- and oil-soluble products while the reaction keeps occurring at the water/oil interface[30, 59].

Aqueous-phase upgrading of small oxygenates is particularly desirable for biomass conversion[22, 108] since pyrolysis of biomass produces large amounts of water and water-soluble small oxygenates[15]. Furfural, one of these small oxygenates, is an important platform chemical produced from pyrolysis of biomass at moderate temperature by dehydration of xylose[5, 109]. Hydrogenation of furfural produces furfuryl alcohol (FOL), tetrahydrofurfural (THFAL) and tetrahydrofurfuryl alcohol (THFOL) as shown in Scheme

* SEM/EDX and TEM images were taken by Dr. Nicholas Briggs;
DFT calculations were performed by Reda Bababrik and Dr. Wenhua Xue.

4. The FOL compound is widely used in the manufacture of resins and fragrances etc.[110]. Further metal-catalyzed hydrodeoxygenation of FOL produces methyfuran[78, 111] while acid-catalyzed hydrolysis of FOL results in levulinic acid[105, 112]. Both methyfuran and levulinic acid are desirable and important chemicals in biorefineries[113].

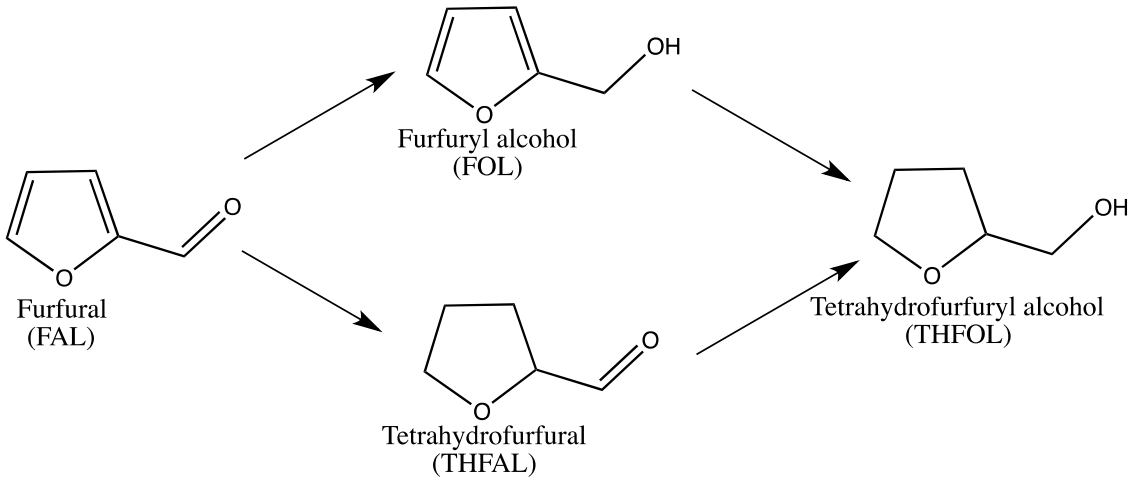

Scheme 4. Reaction pathway of furfural hydrogenation.

How to control the catalytic selectivity of furfural hydrogenation towards FOL represents a challenge for rational catalyst design. The toxicity of the CuCr-based industrial catalysts also drives the exploration of more environmentally friendly alternatives. Sitthisa *et al.* [78, 114, 115] showed that the hydrogenation selectivity is mainly dictated by the adsorption configuration of furfural on the metal surface, that is, strong interaction between the heteroaromatic furanyl ring and the Pd or Ni surface leads to formation of furan while tilted adsorption configuration on group VIII metals through carbonyl group results in high selectivity to FOL. Density functional theory (DFT) calculations of furfural reaction on a Pd(111) surface showed that production of furan and CO is more energetically favorable[116, 117] at low hydrogen coverage, and selectivity towards FOL can be achieved at high hydrogen coverage due to the conformation change of the furfural

molecule[118]. Similarly, modification of the Pd surface using a self-assembled thiol modifier has also been shown to reverse selectivity from furan to FOL as the main product[119, 120].

Liquid-phase catalysis provides another option for tuning the selectivity. Previous experiments generally suggested high yield of FOL over supported single metal (Pt, Ru, Rh, Co, Pd, Cu)[121-123] and multi-metallic metal (PtSn, PdCu, CuCr, CuMgAl)[122, 124-126] in liquid phase, particularly in polar solvent[122, 124], however, the underlying mechanism remains elusive[56]. Additionally, it has also been reported that, over Pt, Pd, Ru and Ni in water at 160-175°C, hydrogenation of furfural produces mainly furan-ring rearrangement products such as cyclopentanone[54, 127, 128]. Understanding the reaction mechanism and the effects of solvent is thus valuable for promoting catalytic activity and tuning activation of either the furanyl ring or the carbonyl group in the furfural upgrading.

In this work, we explore the solvent effect in furfural hydrogenation over a Pd catalyst. We find rate enhancement for furfural conversion and improved selectivity towards hydrogenation of carbonyl group in an aqueous phase as compared to reactions in cyclohexane. DFT calculations unveil that water solvent has multiple effects including stabilizing the intermediate and final products by forming hydrogen bonds and changes the rate-determining step. The reaction order with respect to H_2 changed from 0.3^{th} order in cyclohexane to 0.8^{th} order in water, indicating the difference in rate-determining steps for furfural hydrogenation in two solvents.

5.2 Experimental

5.2.1 Catalyst preparation

Here α-Al_2O_3 supported 3 wt% Pd catalyst was synthesized through sequential incipient wetness impregnation. The α-phase alumina support was acquired from Sigma-Aldrich. The BET method was performed using a Micromeritics ASAP 2010 unit[129]. The α-Al_2O_3 support was found to have a surface area of 3.68 m^2/g and pore volume of 0.0121cm^3/g. The low surface area and low pore volume limited the effectiveness of traditional sequential incipient wetness impregnation method due to the sintering of precursor when drying. The sequential incipient wetness impregnations were applied for three times with 1 wt.% of Pd loading after each performance. A wetting test was used to determine the liquid volume that could coat the outside of the α-Al_2O_3. The α-Al_2O_3 was found to hold 0.1 mL of water per gram of α-Al_2O_3. After the first incipient wetness impregnation with the $Pd(NO_3)_2 \cdot 2H_2O$ aqueous solution, the catalyst was dried in a vacuum oven overnight at 70℃, followed by calcination in air at 300℃ for 3h. 1 wt.% of Pd was anchored after calcination each time. The second and the third-time incipient wetness impregnation were applied sequentially resulting in a 3 wt% Pd loading on α-Al_2O_3.

5.2.2 Catalyst characterization

SEM characterization was performed with a Zeis Neon 40 EsB operated with an accelerating voltage of 5 keV equipped with a field emission gun and INCA Energy 250 Energy Dispersive X-ray (EDX) Microanalysis detector. EDX was used to map the Pd catalyst particles supported on the alumina. The surface metal dispersion of 1 %Pd/α-Al_2O_3

and 2 %Pd/α-Al_2O_3 intermediate catalysts was examined for the effectiveness of the sequential incipient wetness.

For TEM characterization, a JEOL 200FX operated with an accelerating voltage of 200 kV and equipped with a LaB_6 filament was used. The TEM images were used to determine the average particle size and size distribution of Pd particles. The particles were measured using ImageJ software and the particle diameter distributions were analyzed by histogram for average particle diameter calculation.

5.2.3 Catalyst test

The liquid phase furfural hydrogenation reactions were carried out in a total volume of 300 mL high-temperature and high-pressure Parr Batch stirred reactor (Series 4564). 90 mL of solvents and a certain amount of catalyst were loaded in the reactor before the reaction. N_2 was purged into the whole reaction system to vent the air, followed by H_2. The catalyst was reduced under 0.69 Mpa (100 psi) in H_2 and at 100°C for 1 hour. The reactor was cooled down to 40°C and then 30 mL of solvent that contained reactant was purged into the reactor until pressure reached 5.52 Mpa (800 psi) and temperature was held at 40°C. The total reaction volume was kept at 120 mL. The reaction started when mechanic stirring was turned on after the reactant injection. The H_2 inlet valve was kept open to maintain the constant pressure.

The liquid product was filtered and analyzed by gas chromatography. Shimadzu GCMS-QP2010S equipped with a Zebron ZB-1701 column was used for identification of products in the liquid mixture. Agilent 7890B GC-FID equipped with a Zebron ZB-WAXplus column was used for quantification of the individual product. Conversion and yields toward each product are defined as follows:

$$Conversion\ (x\%) = \frac{(mole\ of\ reactant\ reacted)}{(mole\ of\ reactant\ fed)} \times 100\% \quad (74)$$

$$Conversion\ (y\%) = \frac{(mole\ of\ product\ i)}{(mole\ of\ reactant\ fed)} \times 100\% \quad (75)$$

Solvents used in the study were classified as non-polar and protic polar. Non-polar solvents were decahydronaphthalene (decalin) (99%, Sigma-Aldrich) and cyclohexane (99.5%, Sigma-Aldrich). Protic solvent was purified deionized water. Reactant furfural (FAL, 99%, Sigma-Aldrich) was distillated in the N_2 flow before use.

5.3 Results and discussion

5.3.1 Catalyst characterization

The EDX images in Figure 21 present the general compositions on the catalyst surface. The weight percentage of Pd on 3% Pd/α-Al_2O_3 after the third time sequential incipient wetness impregnation is 12.7 wt% (Figure 21 B), which is about 3 times the 4.0 wt% of Pd on the 1% Pd/α-Al_2O_3 sample (Figure 21 A), showing that the sequential incipient wetness impregnation is effective for synthesizing catalysts that have supports with low surface area and low pore volume. Since the volume of precursor aqueous solution is as low as 0.1 mL/g, the method decreases the possibility of palladium particles sintering during drying and calcination at high temperature leading to increased metal dispersion.

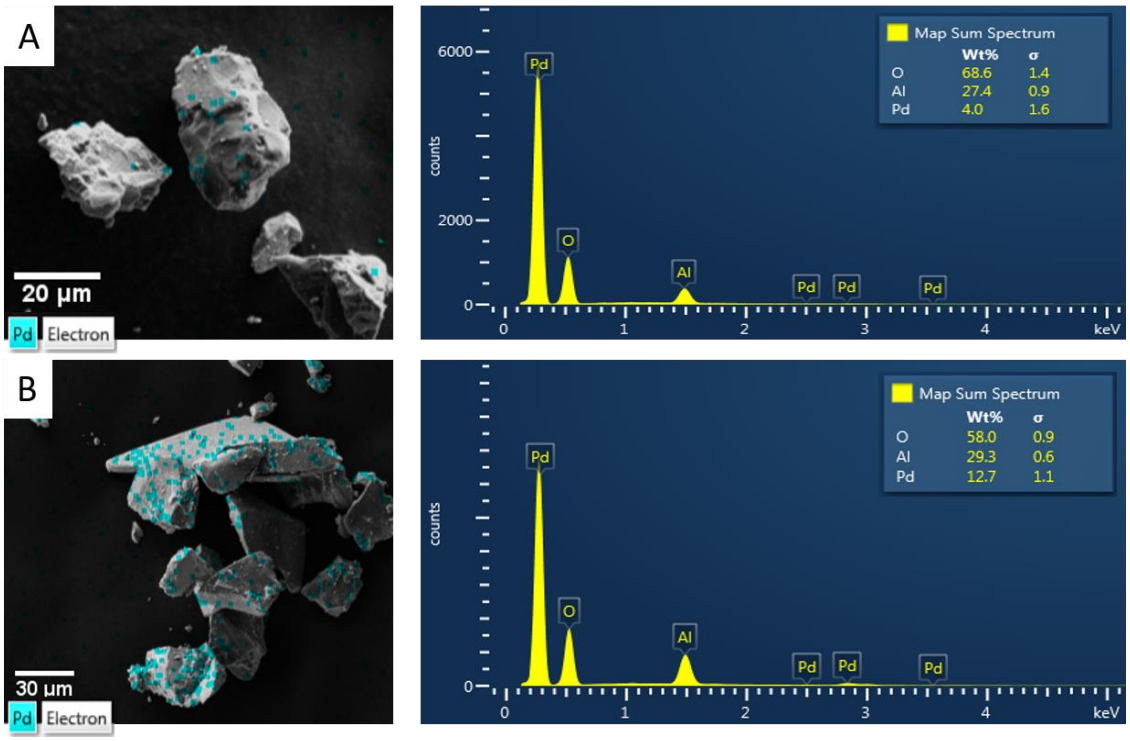

Figure 21. EDX images and elements spectra of (A) 1% Pd/α-Al_2O_3. (B) 3% Pd/α-Al_2O_3

Further TEM images in Figure 22 illustrate the particle sizes of 3% Pd/α-Al2O3. The average particle size are calculated by volume-weighed average diameter equation [27], $\overline{d_v} = \sum_i n_i d_i^4 / \sum n_i d_i^3$, where ni is the number of particles with a diameter di. 100 particles were counted, and the diameter calculated is 4.4 ± 1.1 nm.

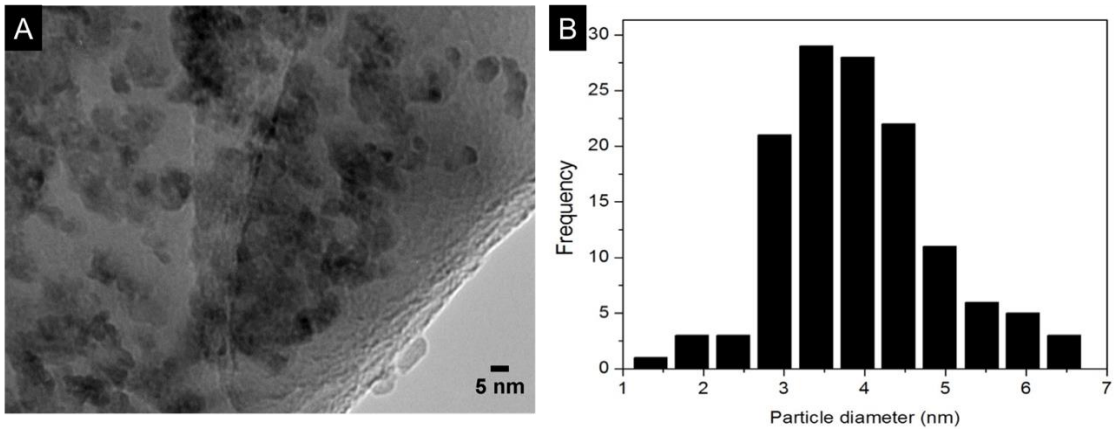

Figure 22. (A) TEM images of 3% Pd/α-Al_2O_3. (B) Pd particle diameter histogram.

5.3.2 Kinetic regime and deactivation test

To ensure the collection of reliable kinetic data, mass transfer tests were conducted to ensure no transport limitations of hydrogen transfer from gas phase to liquid phase and the reactant from bulk to the catalyst surface. Heat transport limitations in liquid phase reactions are commonly not dominant due to the high heat capacities and good thermal conductivities compared to gas phase reactions[56].

To ensure the reaction was carried out with no mass transfer limitations, the stirring speed was increased until conversion no longer changed. These tests were performed in the furfural hydrogenation. Water was chosen to be the solvent due to the highest hydrogenation activity being shown, which may exhibit the mass transfer resistance from the bulk liquid phase to the catalyst surface. 0.1 M of furfural was reacted over 0.1g of 3%Pd/α-Al_2O_3 for 0.8h at 425 rpm and 600 rpm respectively. The result in Figure 5 depicts that the conversion of furfural and yields towards each product, THFAL, FOL, THFOL, are independent of the mechanic stirring force the impeller provided.

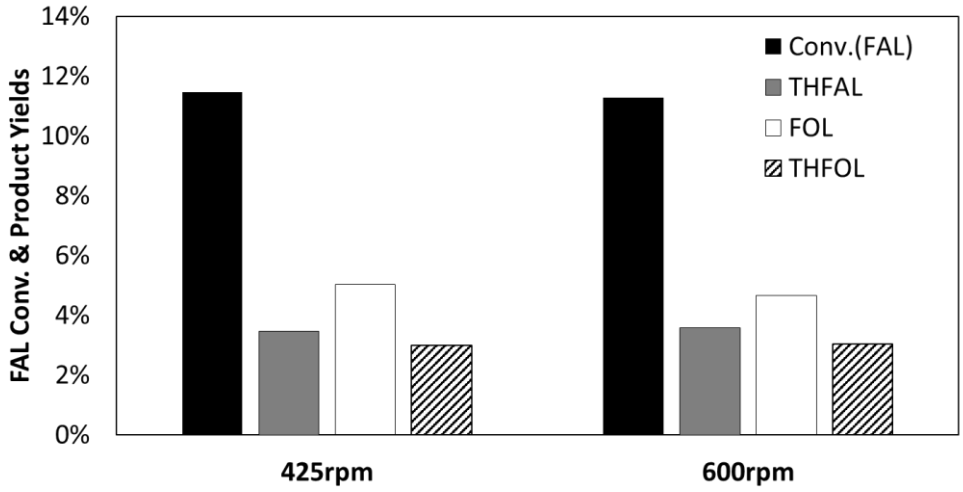

Figure 23. External mass transport test at different stirring rate in water. Reaction conditions: initial concentration of FAL is 0.1M, T=40°C, P=800psi, catalyst amount=100mg 3%Pd/α-Al2O3, reaction time=0.8h.

However, Chambers and Boudart[130] pointed out this test may fail in laboratory reactors. Because the stirring speed is still at low Reynolds number where the mass transfer coefficient is insensitive with the increase of stirring speed.

In order to further prove that the reactions are in the kinetic regime, the widely used criteria in three phases stirring reactors [39, 131, 132] were used. Proposed by Ramachandran and Chaudhari[133], the criteria define the ratio of observed rate to the maximum rate. α_1 describes the gas-liquid mass transfer ratio, and α_2 describes the liquid-solid mass transfer ratio. The criteria are shown as followed:

$$\alpha_1 = \frac{(r_A)_{obs}}{k_l a_b C_A^*} < 0.1 \tag{76}$$

$$\alpha_2 = \frac{r_{obs}}{k_s a_p C_A^*} < 0.1 \tag{77}$$

k_l is the gas-liquid mass transfer coefficient. C_A^* is the saturation solubility that is calculated by Henry's Law. ks is the effective diffusivity, a_p is the catalyst external surface area. The calculation gave the values for α1 is 0.04 and α2 is 2.035×10^{-5}, smaller than 0.1. Showing the kinetic data acquired were in the absence of external mass transfer limitation. In addition, the low surface area and the extremely low pore volume of the catalyst support diminish the presence of intraparticle mass transfer limitation.

The reactions in the study were conducted under 425 rpm in order to provide a moderate agitation so that the thermal couple is fully immersed in the liquid and the catalyst wouldn't splash.

The deactivation tests were carried out in solvent water under reaction conditions. The amount of catalyst was kept at 250 mg and the reaction time was varied. The furfural conversion was compared under shorter time and longer time. The results are plotted in

Figure 24. The overall conversion doubles from 13% in 0.4 h to 26% in 0.8 h, indicating that deactivation is practically absent under the reaction time for 0.8 h. Reactions in both water and cyclohexane didn't show severe deactivation, however it did appear in decalin solvent. This phenomena have been discussed in the following section 5.3.3 Solvent effect. Meanwhile, there is less likely to have polymerization during reaction, because the furfural and furfuryl alcohol polymerization happen at high temperature and under acid-catalyzed condition[134].

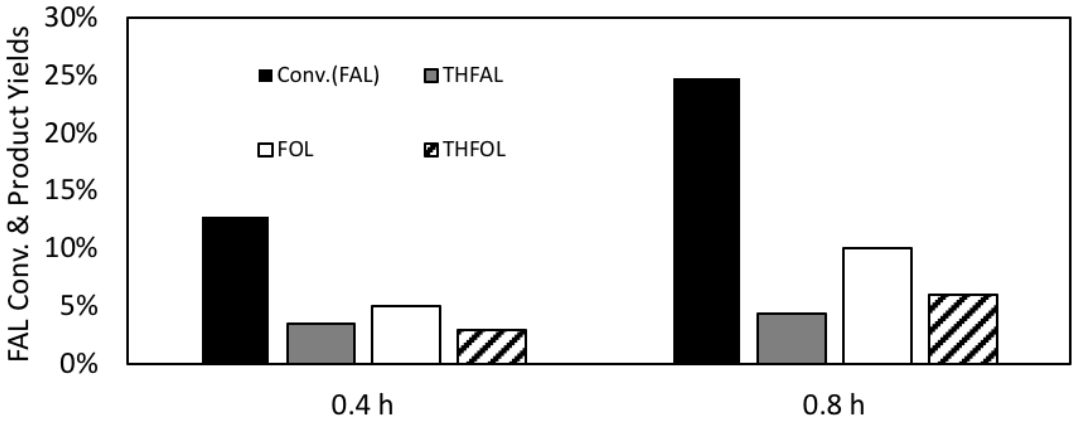

Figure 24. Catalyst deactivation test with different reaction times in water. Reaction conditions: initial concentration of FAL is 0.1M T = 40°C, P = 5.52 MPa, catalyst amount = 250 mg 3%Pd/α-Al_2O_3.

5.3.3 Solvent effect

Furfural hydrogenation reactions were carried out in non-polar solvents, decalin and cyclohexane. The comparisons are listed in Figure 29. The catalytic reactivity in organic solvents is relatively low. 0.25 g of catalyst was used to increase the FAL conversion.

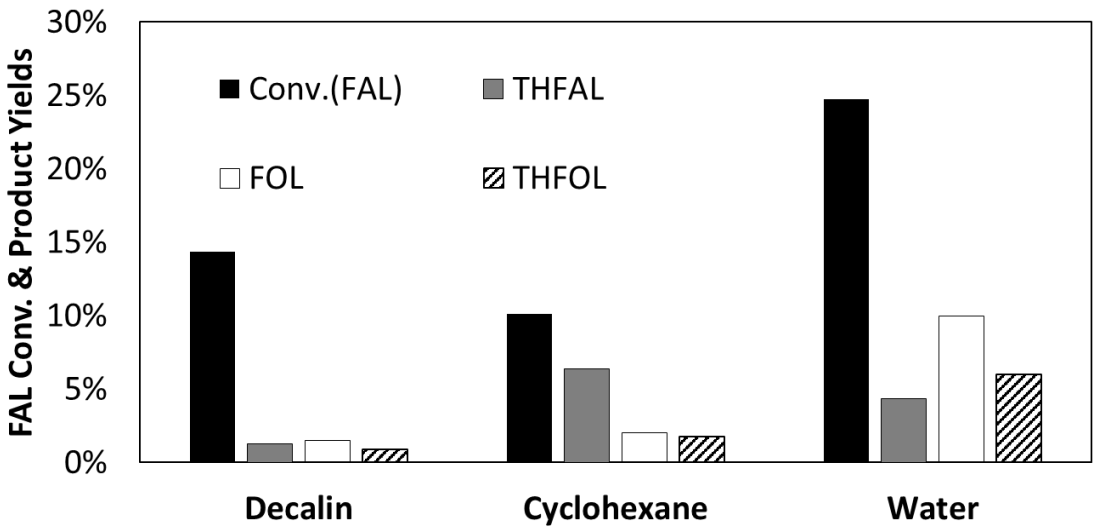

Figure 25. FAL hydrogenation conversion and products yields in different solvents. Reaction conditions: initial concentration of FAL is 0.1M, T=40°C, P=800psi, catalyst amount=250mg 3%Pd/α-Al_2O_3, reaction time=0.8h

Figure 29 shows that THFAL is the main product in cyclohexane, suggesting that furanyl ring hydrogenation (Scheme 4) is preferred. The conversion, defined by disappearance of FAL, in decalin is 14%. However, only 4% of the product yields (FOL, THFAL, THFOL) could be added-up and no other new products were detected by GC-MS. The same reaction in decalin, but with half the reaction time, was conducted and fast catalyst deactivation was observed, while no deactivation has been found in cyclohexane. Furfural dissolves poorly in decalin as compared to cyclohexane. The heterogeneous catalyst provides extra sites for the deposition of FAL on the surface, and the catalyst deactivation was caused by occlusion of furfural, which blocks catalytic sites[135, 136].

However, when furfural hydrogenation reactions were carried out in water, a protic solvent, the reactivity compared to cyclohexane is two times higher, as shown in Figure 29. More importantly, the dramatic difference lies in the selectivity shift. In water, instead

of the furanyl ring hydrogenation, the carbonyl group hydrogenation is preferred. Furfuryl alcohol is produced as the main product.

To understand the increased catalytic activity and selectivity, we explored reaction mechanism and the role of solvents using first-principles DFT calculations on Pd (111). In the absence of liquid water, we find that, in agreement with previous calculations[116], the most stable adsorption configuration of FAL on Pd (111) is the one with the furanyl ring parallel to the surface. When furfural is at the water-Pd (111) interface, the situation is more complicated. Three circumstances are taking into account. The energy profiles of furfural hydrogenation without the presence of water or with water, as well as water assisted H-shuttling are investigated.

Figure 26 shows the calculated reaction pathways of furfural hydrogenation in gas phase and with the presence of liquid water. In these calculations, the hydrogen atoms H*, illustrated in Figure 26A, come from the metal surface rather than as a proton. We find sequential hydrogenation of the oxygen and carbon in the carbonyl groups has an transition state energy of 46 kJ/mol (Figure 26C). In the following discussions, we only focus on the reaction pathway with O and C hydrogenated sequentially. In the presence of liquid water, the transition state energy decreases to -4 kJ/mol with hydrogenation of the oxygen atom as the rate-determining step. The overall reaction becomes more exothermic in water, as compared to only slightly exothermic on a clean Pd(111) surface, because the water phase stabilizes the intermediate (the product after first-step oxygen hydrogenation) and FOL via hydrogen bonds with the intermediate (IMT) and final products. In this mechanism water doesn’t participate in the reaction directly, but its presence changes the adsorption of the intermediate and final products, which in turn modifies the rate-determining step.

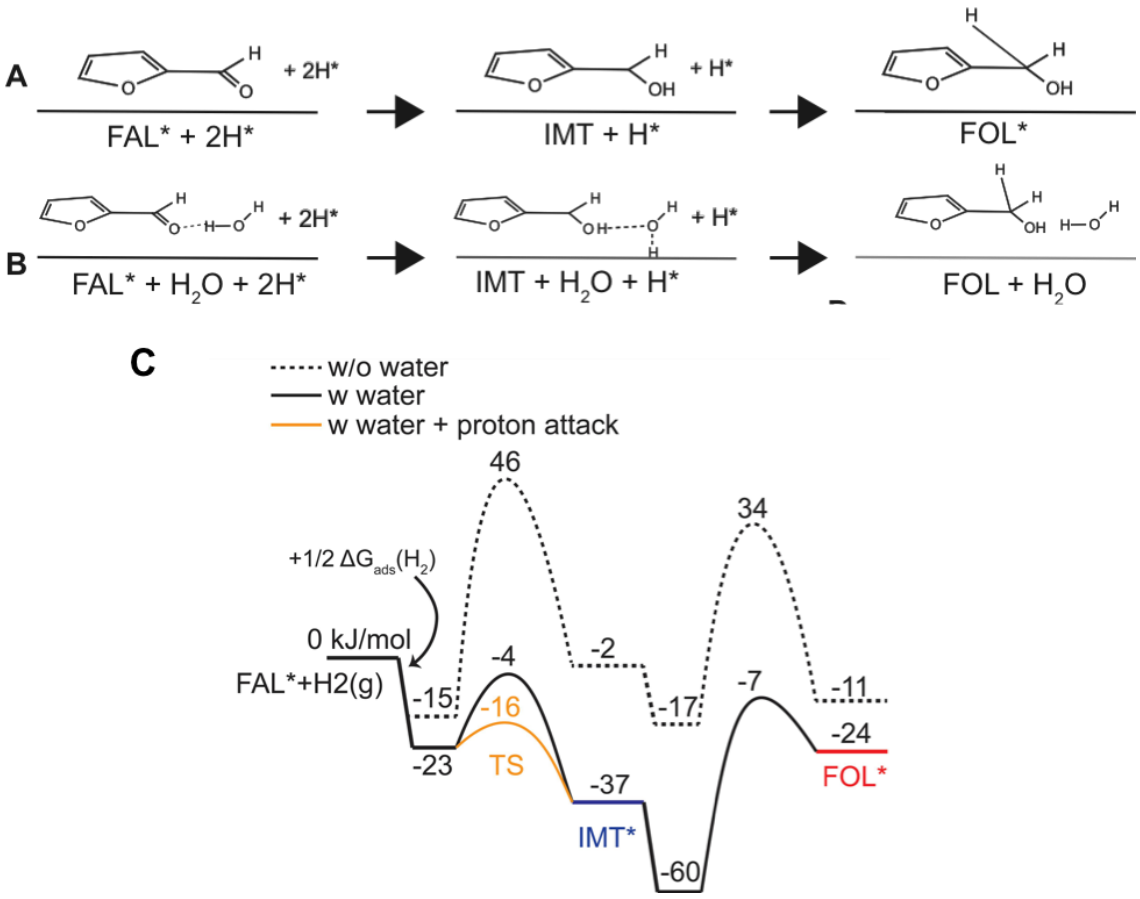

Figure 26. DFT calculations of hydrogenation of furfural. (A) Schematic reaction path in the vapor phase. (B) Reaction path in the liquid water with proton shuttling hydrogenation. (C) Calculated energy profile of the hydrogenation path on Pd in the gas phase and in liquid water.

Water, as a protic solvent, may also directly participate through proton shuttling in the reaction. We find that indeed a water molecule, which adsorbs in the proximity of the FAL and forms a hydrogen bond with the carbonyl group, in the liquid phase can take the hydrogen atom directly from the surface, as shown in Figure 26B, and transfer another hydrogen atom to the carbonyl group via the aforementioned hydrogen bond. In this case, this water molecule acts as a bridge between the carbonyl group and the surface hydrogen atom, resulting in an overall activation barrier of -7 kJ/mol (Figure 26C). The activation barrier for the first hydrogenation step is -16 kJ/mol in liquid water (Figure

26C). The transition state along each reaction pathway (TS1 in Figure 26C) involves a H_3O species.

When organic solvent is applied, the selectivity difference in products has been observed. The calculated adsorption energy of furfural, tetrahydrofuran, cyclohexane, and water over Pd (111) without van der Waals (VDW) interactions are shown in Table 11. The adsorption energy of reactant (furfural) and solvent molecules (water and cyclohexane) is significantly increased when including VDW interaction. The adsorption energy of water is -31 kJ/mol, and the one of cyclohexane is -26 kJ/mol, both of which are significantly smaller than it of furfural, indicating that competitive adsorption between the reactants and the solvents should play a minor role. The change in selectivity in water and cyclohexane is mainly caused by stabilization of intermediates and products via H-bonds and the proton transfer in water, both of which affect significantly the carbonyl group rather than the ring, since the latter of which doesn't form H-bonds with the water phase.

Table 11. Adsorption energy over Pd (111) surface.

	Heat of adsorption, kJ/mol
Furfural	-114
Cyclohexane	-26
Water	-31

5.3.4 Reaction order and rate determining step

The straightforward approach to observe water assisted H-shuttling is to carry out isotope study using D_2O as the solvent. Indeed, the oxygen in the carbonyl group of furfural is deuterated after reaction. However, the further studies indicate that the HD exchange happens rapidly even without catalysts. The hydroxyl group (-OH) in furfuryl alcohol exchanges with D_2O and forms deuterated furfuryl alcohol instantly (Appendix D). The

isotope study fails to demonstrate H-shuttling effect, and therefore an alternative method has been utilized. The DFT calculation has indicated that the presence of water lowers the energy barrier for the 1st hydrogenation, which is the oxygen hydrogenation in the carbonyl group, leading the 2nd hydrogenation of the carbon the rate determining step.

Langmuir-Hinshelwood kinetic model was derived to investigate the furfural hydrogenation in water and in cyclohexane. The organic molecules and hydrogen are adsorbed on different sites. Yoshinao and Tomishige[137] showed that furfural hydrogenation rate over Pd/SiO_2 increases with H_2 pressure, while the furfural concentration change results a negligible change in reaction rate. Therefore, H_2 absorb on different sites and don't compete active sites with other organic molecules. Moreover, in the kinetic study using Pt/C as the catalyst, dual site kinetic model provided the best fit of experimental data[121] .

The hydrogenation kinetic models of furfural hydrogenation to furfuryl alcohol involves adsorption, surface reaction and desorption as follows:

$$H_2^g \leftrightarrow H_2^l \tag{78}$$

$$H_2^l + 2S_1 \overset{K_{H_2}}{\longleftrightarrow} 2HS_1 \tag{79}$$

$$FAL + S_2 \overset{K_{FAL}}{\longleftrightarrow} FALS_2 \tag{80}$$

$$FALS_2 + HS_1 \overset{k_3}{\rightarrow} FALHS_2 + S_1 \tag{81}$$

$$FALHS_2 + HS_1 \overset{k_4}{\rightarrow} FOLS_2 + S_1 \tag{82}$$

$$FOLS_2 \overset{K_{FOL}}{\longleftrightarrow} FOL + S_2 \tag{83}$$

Where k_i is rate constant, and S represents empty Pd sites. Different site adsorption for hydrogen and furfural has been considered on Pd surface based on the conclusion in Chapter 4: 4.3.4 True kinetic model and DFT studies. Depending on whether the first or the second hydrogenation is the rate-determining step, the initial reaction rate when final product is negligible can be expressed as:

$$r = \frac{k_3 K_{FAL} C_{FAL} \sqrt{P_{H_2} K_{H_2}}}{(1 + K_{FAL} C_{FAL})(1 + \sqrt{P_{H_2} K_{H_2}})} \quad (84)$$

$$r = \frac{k_4 K_{FALS} K_{FAL} C_{FAL} (P_{H_2} K_{H_2})}{(1 + K_{FAL} C_{FAL} + K_{FALS} K_{FAL} C_{FAL} \sqrt{P_{H_2} K_{H_2}})(1 + \sqrt{P_{H_2} K_{H_2}})} \quad (85)$$

Where Ki is adsorption constant. Eq. (84) represents the rate when the first hydrogenation of furfural is the rate-determining step, and Eq. (85) is the rate expression when the second hydrogenation is the rate-determining step. When the reactions are carried out under low H_2 pressure, $\sqrt{P_{H_2} K_{H_2}}$ term become insignificant. $1 + \sqrt{P_{H_2} K_{H_2}}$ in the denominator is approximate to 1. Therefore, the reaction order based on H_2 at low H_2 pressure is half order for Eq. (84) and first order for Eq. (85). Similarly, the hydrogenation of furfural to tetrahydrofurfural generates the same reaction order for both surface mechanisms. The difference in reaction order based on H_2 pressure leads to distinguishing rate-determining step during hydrogenation. Furfural hydrogenation is further investigated in cyclohexane and water.

The measured H_2 reaction orders in water and cyclohexane are plotted in Figure 27. H_2 pressure was varied at much lower pressure ranging from 30 psi to 300 psi and the reaction rate was calculated at approximately 10% of overall FAL conversion, which the main product was FOL in water and THFAL in cyclohexane.

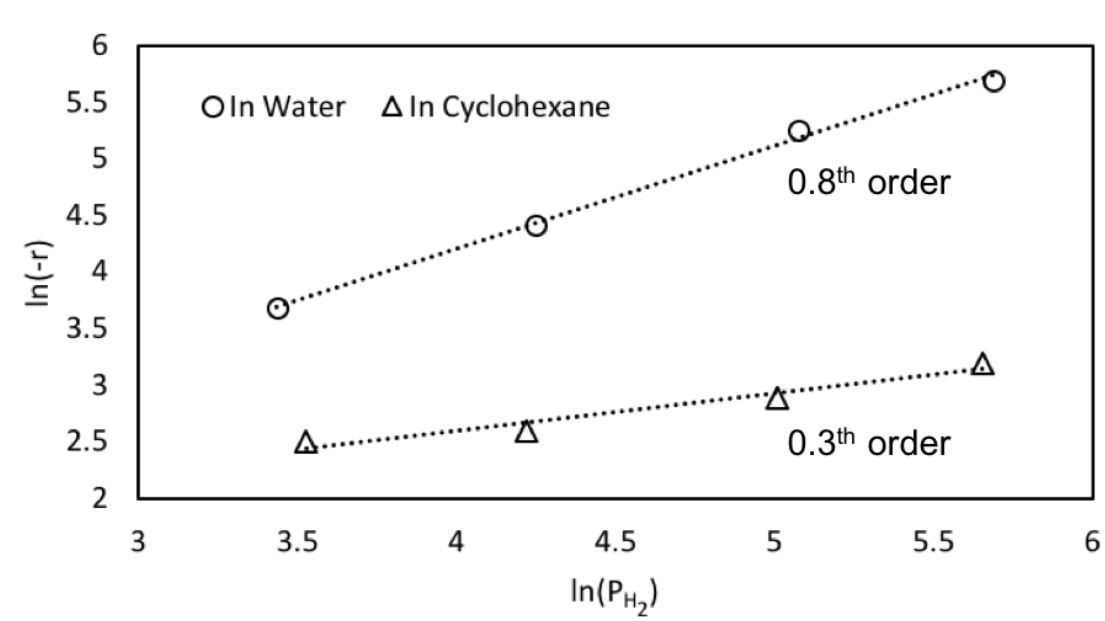

Figure 27. Reaction order as respective of H_2 pressure in water and cyclohexane. Initial concentration of FAL is 0.1M, T=40°C.

In water, the reaction order corresponding to H_2 pressure is 0.8^{th} order, closer to first order reaction, manifesting the rate-determining step is the second hydrogenation of the furfural carbonyl group. The DFT calculations on water assisted H-shuttling effect indicates that water H-bonding network not only stabilizes intermediates but also transfers H^+ through the bridge to the O, which further lowers the activation barrier for the first hydrogenation step. Therefore, the following hydrogenation of the C, the second hydrogenation step, becomes the highest energy barrier for the reaction. The kinetic measurement draws the same conclusion as the DFT calculations in water.

On the contrary, the reaction order as respective of H_2 pressure is 0.3^{th} order in cyclohexane, which is much closer to the 0.5^{th} order reaction. The reaction order analysis demonstrates without the presence of water the first hydrogenation is the highest the energy barrier regardless of carbonyl group or C=C hydrogenation. Because THFAL is the main

product in cyclohexane. Combining the kinetic analysis from Eq. (84), the rate-determining step is the first hydrogenation of C=C in furfural ring. Similar results have been found in cyclohexene hydrogenation over Pd in Chapter 4: 4.3.4 True kinetic model and DFT studies where the first hydrogenation of C=C has been found to be the rate determining step experimentally.

5.4 Conclusion

In this Chapter, hydrogenation of furfural has been investigated in different solvents over on a palladium catalyst. Hydrogenation of the furanyl ring is favored in organic aprotic solvent and carbonyl group is favored in aqueous solution with an enhanced reaction rate. DFT calculations suggest that water solvent influences the hydrogenation rate by taking part in the kinetically relevant step of furfural activation. Both the intermediate and final products are stabilized by the liquid water via H-bonds formed between the water phase and the carbonyl group in furfural. Proton shuttling through the H-bonded water network further reduces the activation barrier for the hydrogenation of the carbonyl group. Moreover, reactions with different H_2 pressures further unveil that the reaction order with respect of H_2 in water is 0.8^{th} compared to the 0.3^{th} order in cyclohexane. Kinetic analysis indicates a consistent result with DFT calculations that second hydrogenation of the C of the carbonyl group is the rate determining step in water while the first hydrogenation of the C=C of the furanyl ring is the rate determining step in cyclohexane. This work shows that solvent provides an additional degree of freedom for tuning the activity and selectivity of a catalytic reaction, which is expected to be generally true for liquid-phase heterogeneous catalysis.

Acknowledgements

This work was supported by the U.S. Department of Energy, DOE/EPSCOR (Grant DESC0004600). The computational research used the supercomputer resources of the National Energy Research Scientific Computing Center (NERSC), the Extreme Science and Engineering Discovery Environment (XSEDE), the OU Supercomputing Center for Education & Research (OSCER) at the University of Oklahoma, and the Tandy Supercomputing Center (TSC). We thank Dr. Tawan Sooknoi (King Mongkut's Institute of Technology Ladkrabang, Thailand) for valuable discussions.

Chapter 6: Aqueous Phase Reforming of Ethanol on Synergistic Bimetallic Ru-Pt Catalysts*

6.1 Introduction

Hydrogen-based technologies play a key role in the development of sustainable, cleaner, more efficient, and lower CO_2 footprint energy systems [138]. Aqueous phase reforming (APR) of biomass-derived oxygenates provides high-yield H_2 production in a single-step catalytic processes at moderate temperatures [20, 21]. Bio-ethanol, produced from renewable biomass, is an attractive feedstock for H_2 production, which has been widely used for high-temperature steam reforming over different metal catalysts [139-142]. Almost all catalysts for ethanol steam reforming produces CO and coke at high temperature that result catalysts deactivation. Therefore, the advantage of using low-temperature aqueous phase reforming not only eliminates significant energy input but also operates at temperature range that thermodynamically favors water gas shift (WGS) reaction in order to extract more H_2 from water.

In low-temperature ethanol reforming, the primary reaction mechanism involves dehydrogenation upon adsorption, followed by cleavage of the C-C bond to form surface CO, which further reacts via water gas shift (WGS) reaction [142, 143] and CH_x species, which can be hydrogenated to produce CH_4. If the surface CO undergoes methanation instead of WGS, the production of hydrogen is greatly inhibited since not only prevents formation of H_2, but also it consumes H_2 to make CH_4. Among the various metals investigated during the last few decades, Pt exhibits one of the highest selectivity towards

* TEM images were taken by Brent Johnson and Lisa Whitworth at Oklahoma State University; XRD image was prepared by Feifei Yang.

H_2 and has been often considered as a promising catalyst for APR of oxygenates [21]. However, the low reaction activity of Pt results in the insufficient C-C cleavage. By contrast, although Ru has shown lower selectivity towards H_2 production and high yield towards alkanes (especially CH_4) formation via methanation reaction and Fischer-Tropsch synthesis (FTS) [21, 144], it also reveals high activity towards C-C bond breaking, which is a desirable reaction to maximize yield. Therefore, designing optimal catalysts for APR of ethanol requires maximizing the efficiency of C-C cleavage, inhibiting the methanation reaction, and facilitating WGS activity.

In this work, we have explored mono- and bimetallic Pt and Ru catalysts supported on carbon and TiO_2. First, particle size effects were investigated over monometallic Ru and Pt catalysts. It was found that small Ru particles exhibit higher selectivity towards H_2 production and lower CH_4 formation than larger Ru particles. To explore the effect of particle size on surface CO dissociation after the C-C cleavage of ethanol, the rate of Fischer-Tropsch synthesis was compared over the different Ru catalysts. On Pt, selectivity towards CH_4 and C1 oxygenated is higher for smaller particle sizes, but in general, Pt is less active than Ru for C-C cleavage. The comparison of the performance of both monometallic metals lead to the investigation of bimetallic Ru-Pt catalysts, which show synergistic performance, with increased reaction rate for H_2 production but lower rate for CH_4.

6.2 Experimental

6.2.1 Catalyst preparation

Supported Ru and Pt catalysts were synthesized by conventional incipient wetness impregnation, followed by high temperature thermal decomposition of the metal

precursors. This decomposition was conducted in hydrogen flow for the C-supported catalysts or in air flow for the TiO_2-supported ones. A series of monometallic Ru catalysts with different loadings and supports were prepared by impregnating ruthenium(III) nitrosyl nitrate solution (Sigma-Aldrich, 1.5 wt.% Ru) over activated carbon (Sigma-Aldrich, charcoal activated Norit®) and titanium(IV) oxide (Sigma-Aldrich, ⩾ 99.5%, P25), respectively. The 5% Ru/C (Type 619) was purchased from Alfa Aesar. The monometallic Pt catalysts were prepared by impregnating an aqueous solution of chloroplatinic acid hydrate (H_2PtCl_6, Sigma-Aldrich, ⩾ 99.9%) over the same two supports as above, and subsequently dried at 70°C, overnight. The thermal decomposition was achieved by heating (in H_2 or air) at 400°C for 4 h for $Ru(NO)(NO_3)_3$ [145] and at 500°C for 3 h for H_2PtCl_6 [146]. Bimetallic Ru-Pt catalysts supported on TiO_2 were prepared by sequential impregnation or co-impregnation. The sequential impregnation was carried out by impregnation and decomposition of the first metal precursor followed by loading the second metal precursor. The calcination conditions employed were the same as those for the preparation of monometallic catalysts. In the co-impregnation method, the impregnating aqueous solutions were mixtures of ruthenium (III) chloride hydrate (Sigma-Aldrich, 99.98 %) and chloroplatinic acid hexahydrate at the desired ratios. The impregnated sample was then dried at 70°C overnight followed by calcination in air at 500°C for 4 h [147]. Based on the preparation method used, $Ru/Pt/TiO_2$ indicates that Pt was sequentially impregnated over a previously calcined Ru/TiO_2. Likewise, $Pt/Ru/TiO_2$ indicates that Pt was impregnated first and then Ru. By contrast, the co-impregnated bimetallic catalyst is represented as $Ru\text{-}Pt/TiO_2$.

6.2.2 Catalyst characterization

N_2 physisorption was performed on supported monometallic Ru and Ru-Pt bimetallic catalysts on a Micromeritics ASAP 2010 unit. Prior to analysis, the samples were degassed *in situ* at 230°C for 24 h. The micropore volume was derived from the t-plot method (relative pressure range: 0.2−0.6) and the total pore volume was determined at $p/p_0 = 0.99$.

The TEM images were obtained in a transmission electron microscope JEOL JEM-2100, operating with an accelerating voltage of 200 kV, equipped with LaB_6 gun. Catalyst samples were pre-reduced under H_2 flow at 250°C for 3 h before depositing them on carbon-coated copper TEM grids. From the TEM images, metal particle size distributions were obtained by analysis with ImageJ software [27].

X-ray powder diffraction (XRD) patterns for monometallic Pt, Ru and bimetallic Pt-Ru catalysts were collected on a D8 Series II X-ray Diffractometer (BRUKER AXS), using K radiation generated at 40 kV and 35 mA. Prior to the measurements, the samples were reduced ex-situ under pure H_2 (60 mL/h) at 523.15 K for 3 h. The scans covered the 2θ range from 20 to 80°.

6.2.3 Reaction procedure

APR of ethanol was conducted in the liquid phase, in a 160 mL high-pressure Parr reactor (Model 4564), operated at high temperature in batch mode. In each run, 80 mL of deionized water and 100 to 200 mg of catalysts were placed in the vessel to perform the catalyst reduction under 200 psi of H_2 at 250°C[147, 148], for 2 h. Subsequently, the reactor was cooled down to room temperature and purged with Ar. At this point, 20 mL solution consisted of 15 mL ethanol (Sigma-Aldrich, $\geqslant$ 99.5 %) and 5 mL water were injected into

the aqueous solution. The overall volume of reactants is 100 mL, corresponding to an ethanol concentration of 15 vol %, which was the same for all reaction runs. By injecting Ar, the system was pressurized to 200 psi (1.38 MPa), which allowed having an internal standard for gas composition analysis. Mechanical stirring was started at 600 rpm and the temperature was raised to the desired value of 250°C. After the reaction period, the stirring was stopped, and the reactor was quenched to room temperature. The gas phase products were collected in a single-ended miniature sample cylinder and quantitatively analyzed on a Carle Series 400 AGC equipped with TCD. Liquid products were qualitatively identified on a Shimadzu GCMS-QP2010S, equipped with a Zebron ZB-1701 column and quantified on an Agilent 7890B GC-FID, equipped with a Zebron ZB-WAXplus column.

Aqueous phase Fischer Tropsch synthesis (FTS) reaction was carried out as an additional probe reaction. For this, 100 mg of 5% Ru/C and 150 mg of 0.5% Ru/C were reduced in 100 mL of water under 200 psi of H_2 and 250°C for 2 h. Then, the system was cooled down and purged with N_2 before introduction of the reactant gas mixture, which contained a H_2 and CO at a molar ratio of 5 and 200 psi. The FTS reaction was conducted at 250°C for 17 h. The gas phase products were analyzed on Carle Series 400 AGC, equipped with a TCD and on an Agilent GC-MS, equipped with a J&W HP-PLOT Q column; the liquid phase products were identified using Shimadzu GCMS-QP2010S, equipped with a Zebron ZB-1701 column.

Ethanol conversion and H_2 production rate for each catalyst are defined as follows:

$$Conversion\ (\%) = \frac{(mole\ of\ reactant\ reacted)}{(mole\ of\ reactant\ fed)} \times 100\% \qquad (86)$$

$$Rate\ of\ Hydrogen\ Production = \frac{(mole\ of\ H_2\ producred)}{(mass\ of\ catalyst) \times time} \quad (87)$$

6.3 Results and discussion

6.3.1 Catalysts characterization

The surface area, pore volume, and average particle size of the various catalysts investigated are presented in Table 12. The measured surface area for the C-supported Ru catalysts is much higher than those of TiO_2-supported Ru catalysts due to the correspondingly different areas of the two supports. The surface areas for the C-supported catalyst series are greater than 500 m^2/g while those of the TiO_2 -supported series are less than 50 m^2/g. The TiO_2 utilized in the catalyst synthesis is P25, which is a mixture of anatase and rutile phase. Since the anatase phase is less stable than the rutile phase upon heating the higher calcination temperature (500°C) used for the bimetallic catalyst may have led to partial collapse of the pore structure and loss of overall surface area [147, 149], as observed in Table 12.

Table 12. Characterization of Ru series catalysts.

Sample	Surface area m^2/g	Pore volume cm^3/g
5% Ru/C	585	0.42
0.5% Ru/C	867	0.68
2.6% Ru/TiO_2	51	0.25
0.5% Ru/TiO_2	52	0.20
1% Ru-2% Pt/TiO_2	33	0.10

The TEM images and particle size distributions are shown in Figure 28. It can be seen that varying metal loading on the different supports resulted in significant differences in particle size. For instance, the samples with higher Ru loading, 5% Ru/C and 2.6% Ru/TiO_2, have average diameters of 3.3 and 3.9 nm, respectively. By contrast, those with

low Ru loading, 0.5% Ru/C and 0.5% Ru/TiO_2, have much smaller diameters, 1.4 and 1.7 nm, respectively. Since the fraction of surface sites with low coordination, such as corners and edges, greatly increases when the particle size is smaller than 2 nm, while above that the surface is dominated by flat plane terraces [150], we can consider these four samples as representative of the two extremes, high coordination flat terraces and low coordination steps/edges. Chemical bonding of reactants and intermediates on these different types of surface sites during the APR of ethanol is expected to be different, which should result in changes in relative reaction rates and product distribution, as shown below.

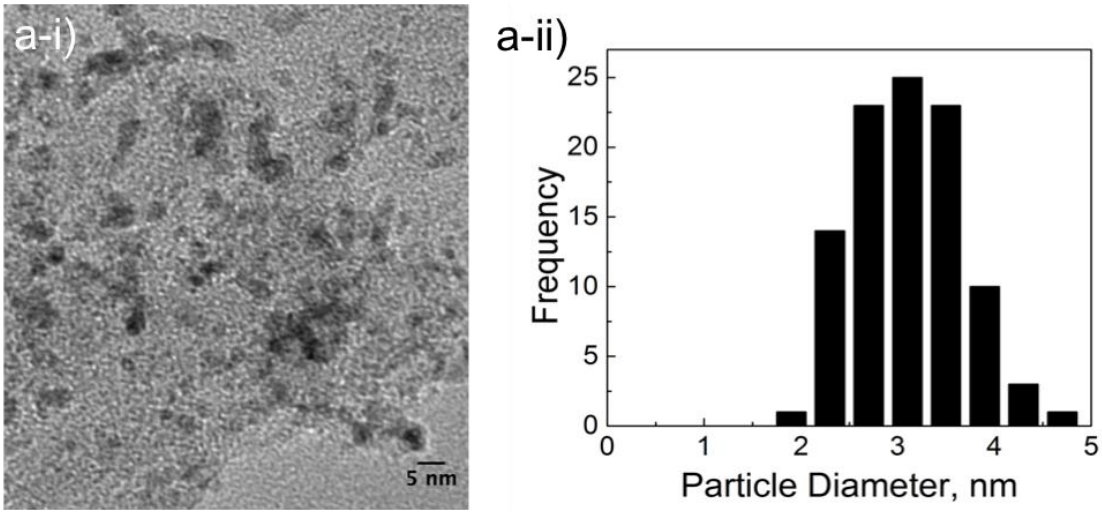

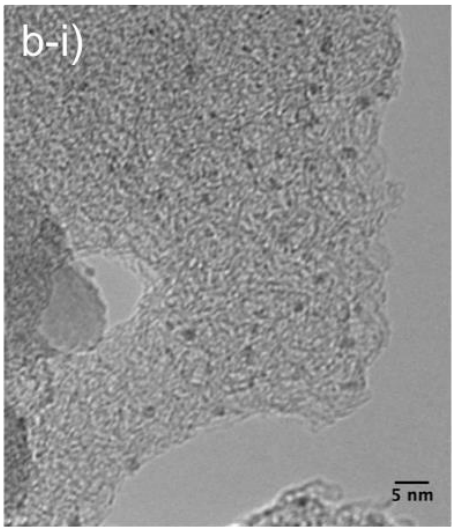
b-i)
5 nm

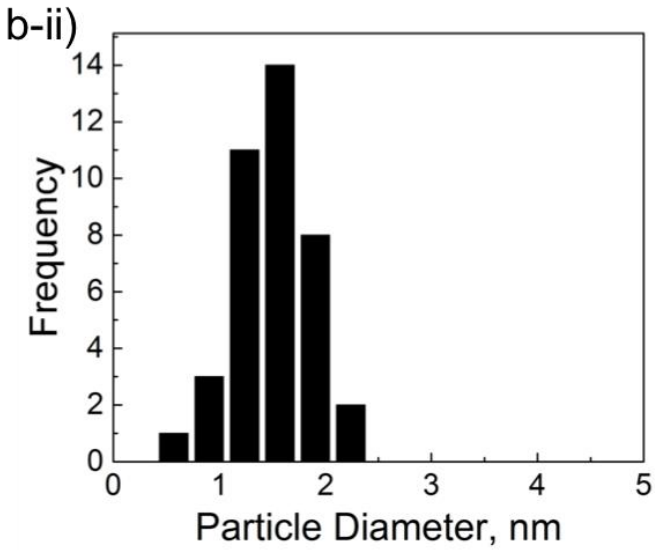
b-ii)
Frequency
Particle Diameter, nm
0
2
4
6
8
10
12
14
0
1
2
3
4
5

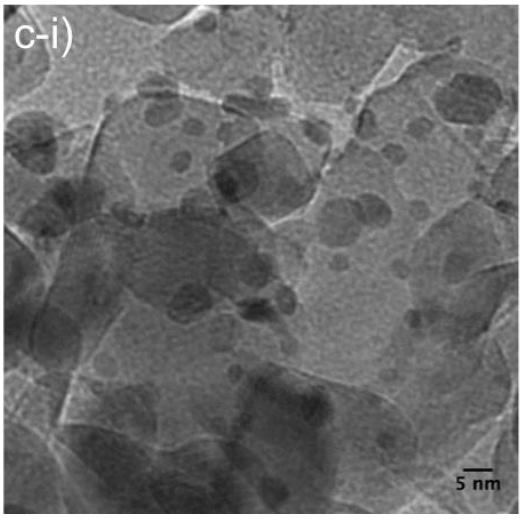
c-i)
5 nm

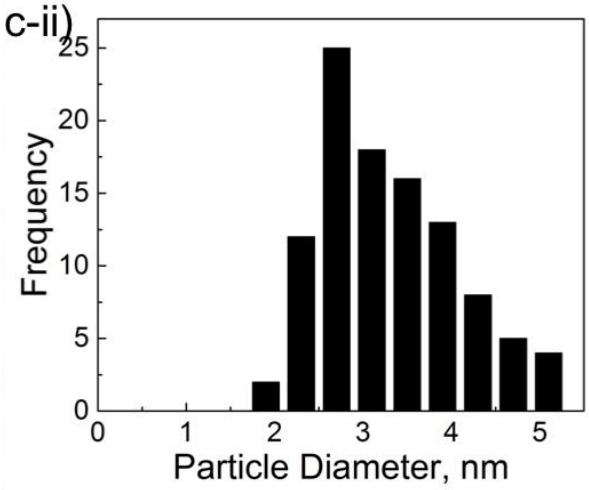
c-ii)
Frequency
Particle Diameter, nm
0
5
10
15
20
25
0
1
2
3
4
5

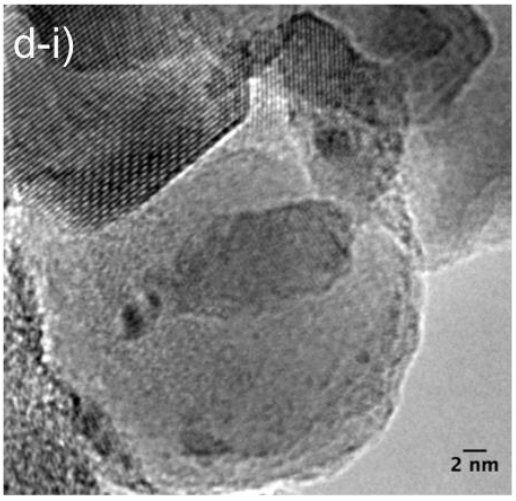
d-i)
2 nm

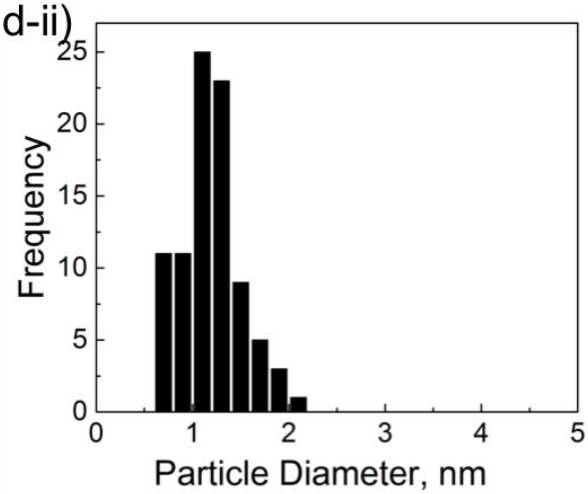
d-ii)
Frequency
Particle Diameter, nm
0
5
10
15
20
25
0
1
2
3
4
5

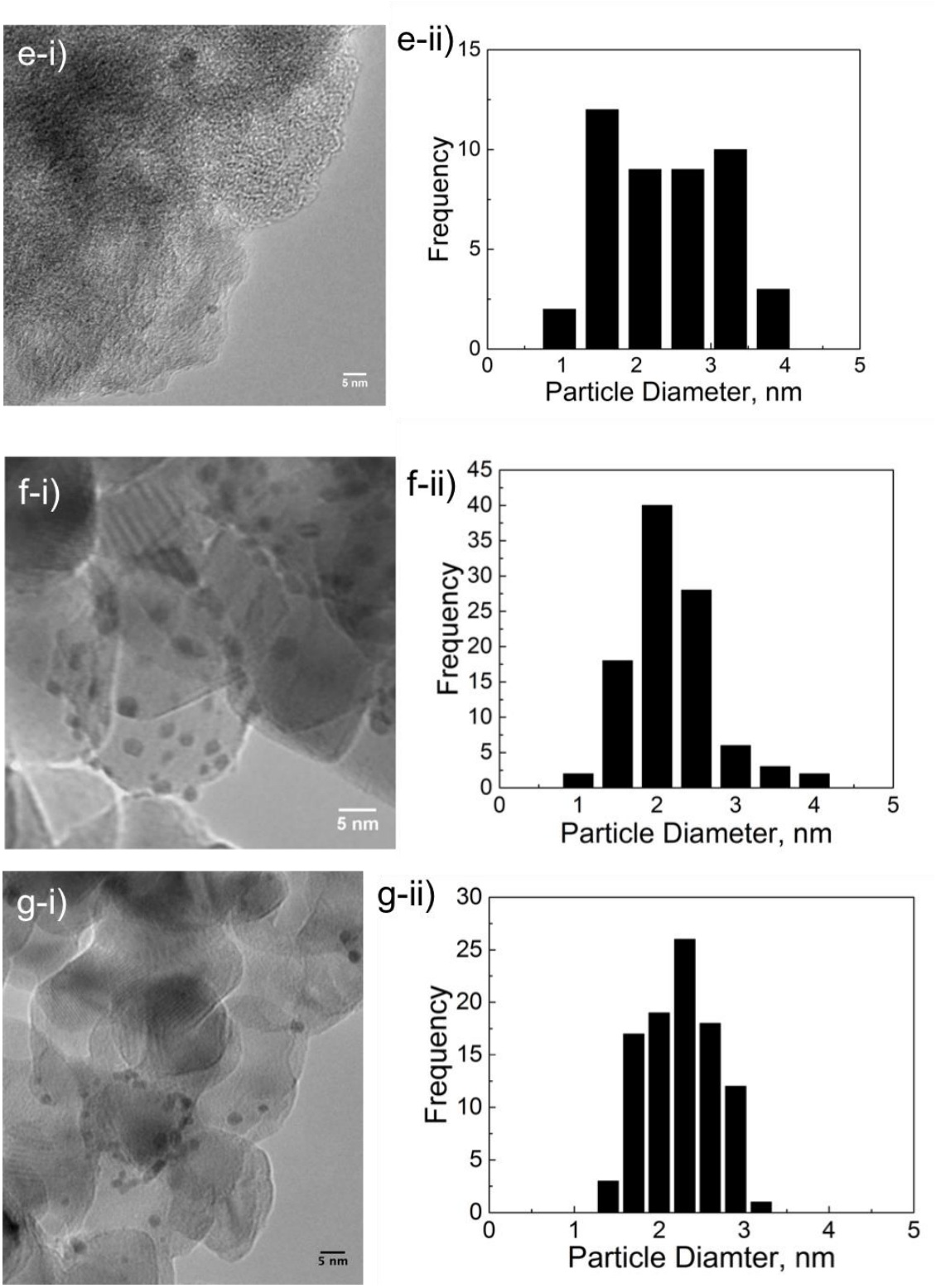

Figure 28. TEM images (i) and particle diameter distribution (ii) of the different catalysts; (a) 5% Ru/C; (b) 0.5% Ru/C; c) 2.6% Ru/TiO_2 ; (d) 0.5% Ru/TiO_2; (e) 1% Pt/C; (f) 2% Pt/TiO_2 and (g) 1% Ru-2% Pt/TiO_2

6.3.2 Reaction pathways

The experimental results on both Ru and Pt catalysts obtained at an initial ethanol conversion of approximately 10% are shown in Table 13. It is observed that at the same level of low conversions, acetaldehyde is the main liquid product while diethyl ether and acetic acid were only significant in some of the catalysts. The gas products contain predominantly H_2, CO_2 and CH_4, with smaller amounts of ethane and ethylene. To analyze the possible reaction pathways on 0.5% Ru/TiO_2, the evolution of liquid products has been plotted as a function of reaction time (Figure 29). It can be observed that on this low metal loading the initial rate of acetaldehyde formation at 1 hour is 6.6 mmol/h, which is much higher than that of diethyl ether. The formation of acetic acid is not detected by GCs until 3 hours of reaction. Therefore, it can be concluded that the primary products of ethanol reforming on this catalyst are acetaldehyde and H_2, arising from the direct dehydrogenation of ethanol.

Table 13. Liquid phase and gas phase product distribution of APR of ethanol.

Sample	Amount mg	Time h	Conversion	Liquid products mmol			Gas product mmol						Product Ratio	
				acetaldehyde	acetic acid	diethyl ether	H_2	CO_2	CH_4	CO	C_2H_6	C_2H_4	C1/C2	CO_2/CH_4
5% Ru/C	100	1	12 %	3.82	0.00	0.11	6.93	9.60	33.99	0.72	1.29	0.00	11.59	0.28
0.5 % Ru/C	150	3	9 %	6.75	0.00	1.35	12.13	4.16	8.08	2.00	0.99	0.00	2.11	0.52
2.6% Ru/TiO_2	200	1	11 %	2.73	0.00	0.02	9.18	9.10	29.56	0.00	3.03	0.00	14.14	0.31
0.5% Ru/TiO_2	200	3	11 %	8.22	1.06	3.12	18.08	3.58	7.64	0.84	1.38	0.00	1.30	0.47
1% Ru/C	200	1	7 %	3.36	0.63	0.60	27.30	7.27	10.29	0.00	1.03	0.00	4.40	0.71
2% Ru/C	200	1	11 %	3.74	2.54	3.98	18.95	3.26	3.33	0.00	2.06	0.00	1.05	0.98
0.5% Ru/2% Pt/TiO_2	200	1	9 %	3.55	3.60	1.92	33.04	2.72	2.91	0.00	1.14	0.00	0.79	0.93
2% Pt/0.5% Ru/TiO_2	200	1	13 %	2.91	4.18	2.80	39.65	8.45	14.74	0.00	1.84	0.00	3.27	0.56
1% Ru-2%Pt/TiO_2	200	0.75	9 %	1.84	0.00	0.19	44.12	9.10	12.03	0.00	2.75	0.00	11.49	0.76
TiO_2	200	1	1 %	1.52	0.00	1.49	1.88	0.00	0.00	0.00	0.00	0.29	0	0

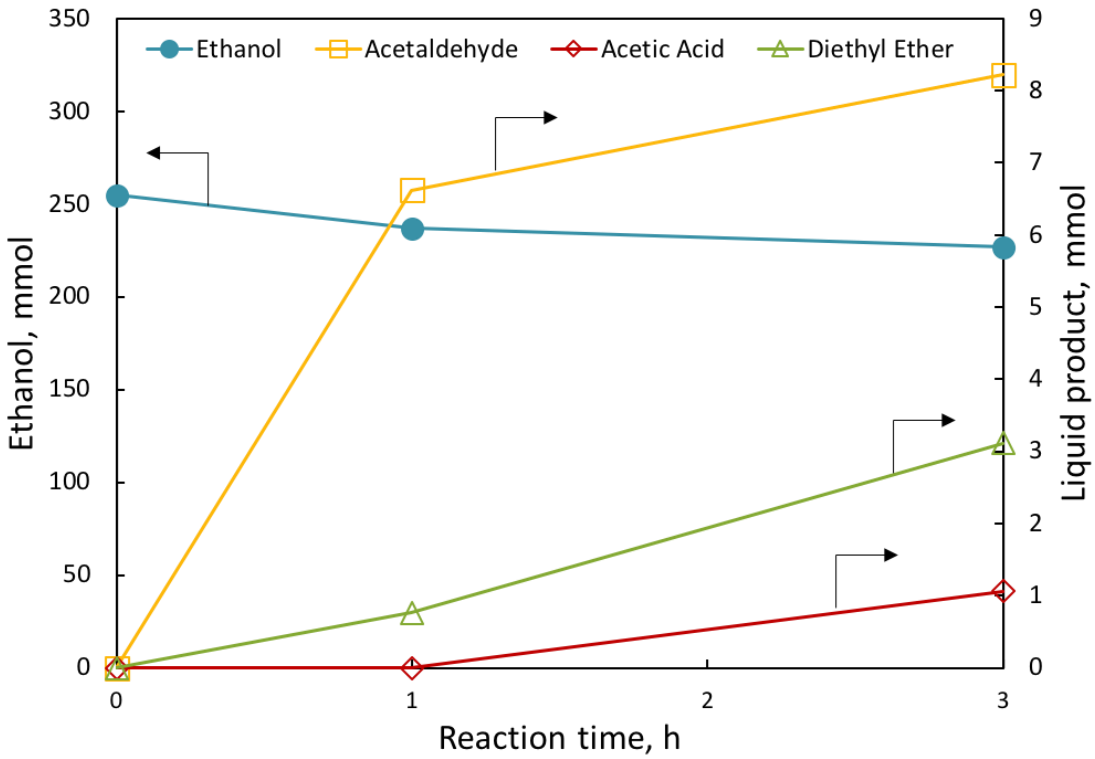

Figure 29. Liquid product distribution of 0.5% Ru/TiO_2 catalysts as a function of reaction time. Reaction conditions: 200 mg of catalyst, 250 °C 200 psi of Ar; Feed: 15 vol.% ethanol aqueous solution with overall volume of 100 mL.

Density functional theory (DFT) calculations of oxygenates reforming have been previously conducted over Ru [151, 152] and Pt [153-158]. The adsorption of ethanol is thermodynamically favorable when a surface ethoxy species is formed via dehydrogenation, which starts at the O. The elongation of the O-H bond reduces the electron orbital overlap between H and O, leading to the detachment of H from O. This first steps is followed by dehydrogenation of the Cα and, finally, formation of the adsorbed surface acetaldehyde [155]. The dehydrogenation of the surface acetaldehyde has been studied with high-resolution electron energy loss spectroscopy (HREELS) [159]. It has been shown that this step leads to the formation of a surface acetyl species, which are

important metastable intermediates. Further dehydrogenation of acetyl species takes place on Cβ, which would produce a ketene CH_2CO species.

As a consequence of the sequential dehydrogenation, the C-C bond weakens. It seems like this double dehydrogenation (of O-H and C-H bonds) requires a lower energy barrier than that required for C-C cleavage, which still requires another dehydrogenation step before it can occur. Calculations show that the energy barrier for C-C cleavage decreases with the extent of dehydrogenation. For example, over Ru (0001), the activation energy of C-C cleavage decreases from 255 kJ/mol prior to adsorption to the lowest value of 38 kJ/mol when the surface ketene CH_2CO species are formed [152]. A much lower effect of dehydrogenation occurs with Pt; in fact, the activation energy of C-C cleavage over Pt (111) only diminishes to 90.24 kJ/mol after the surface ketenyl CHCO is formed [156]. In comparison, a deeper degree of dehydrogenation is needed over Pt in order to weaken the C-C bond. Moreover, over both metals the adsorption geometry of ethanol changes during the dehydrogenation steps [152, 154]. The metal-O bond of the surface ethoxy group is tilted upon adsorption, making dehydrogenation of O-H and Cα-H easier than C-C cleavage. However, a later dehydrogenation of Cβ leads to a parallel adsorption geometry that weakens the metal-O bond. As O moves away from the surface C-O cleavage becomes much harder.

Cleavage of the C-C bond results in the formation of CH_4 and CO with a molar ratio of 1. The detection of CH_4 shows up among all the metal catalysts in Table 13, although the quantity varies between different catalysts. Yet CO takes little or no partial pressure in gas products. In fact, CO is usually formed as one of the major gas product in ethanol reforming[160, 161]. However, under the reaction temperature of 250°C and high

water/ethanol molar ratio (18:1), the WGS reaction is thermodynamically favored[162], and therefore CO rapidly reacts with water, yielding CO_2 and H_2.

Theoretically, CO is converted into an equimolar of CO_2 completely after the WGS reaction. Combining with previously formed CH_4 after C-C cleavage, an equimolar ratio of CO_2 to CH_4 would be produced in the end. On the contrary, catalysts such as 5% Ru/C and 2.6% Ru/TiO_2 have significantly deviated from this ratio. In 5% Ru/C for instance, the amount of CH_4 is 33.99 mmol, which surpasses 9.6 mmol of CO_2. Provided that CH_4 directly comes C-C cleavage, there should have been 33.99 mmol of H_2 or CO_2 produced after the WGS reaction. Nevertheless, the total H_2 is merely 6.93 mmol and CO_2 is 9.60 mmol. The discrepancy suggests that H_2 and CO_2 in the reaction system have been further consumed in order to produce additional CH_4. It has been investigated that both Pt and Ru have different activities towards methanation [163, 164], which is the hydrogenation of CO and CO_2 and the product of this reaction is CH_4. Therefore, the ratio of CO_2 to CH_4 varies over different catalysts, depending on their relative activities for the two reactions. Thus, this CO_2/CH_4 ratio can be taken as a figure of merit when assessing different catalysts for the APR of ethanol.

As depicted in Scheme 5, the low temperature APR of ethanol over Ru and Pt involves the following steps. First, ethanol can be dehydrogenated to form a surface aldehyde species, which in turn could either desorb to the liquid phase or undergo hydration and further dehydrogenation to produce a carboxylic acid. While this path generates H_2, it does not include C-C cleavage and consequently does not produce the maximum yield of H_2. By contrast, if the surface aldehyde species undergoes C-C cleavage via decarbonylation, CH_4 and CO are produced at a 1:1 ratio. In a subsequent step, adsorbed

CO could alternatively undergo water-gas shift reaction or methanation. In the first case, it further produces H_2, in the second case, CH_4. A parallel path that does not produce H_2 is the dehydration-etherification that leads to diethyl ether. Another possible product is ethane, which is obtained by dehydration of ethanol to ethylene followed by hydrogenation.

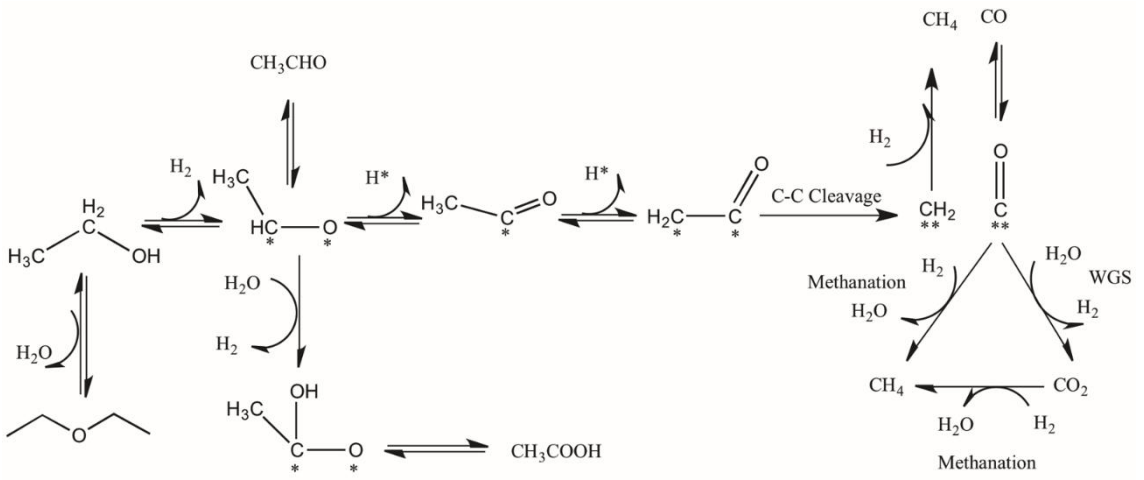

Scheme 5. Reaction pathways of the low temperature aqueous phase reforming of ethanol.

6.3.3 Ru particle size effects

To evaluate the effect of particle size on Ru catalysts, liquid- and gas-phase product distributions are compared at early stages of reaction (approximately 10% conversion) for the different Ru catalysts, as listed in Table 13. The greatest differences in the Ru series are observed in the gas-phase product distributions (see Figure 30). The catalysts with high Ru loading and larger particle sizes produce much more CH_4 than H_2. The CH_4/H_2 molar ratios for 5% Ru/C and 2.6% Ru/TiO_2 are 5 and 3, respectively. By contrast, on the low loading, small particle size catalysts, 0.5% Ru/C and 0.5% Ru/TiO_2, the CH_4/H_2 ratio is less than 1, indicating that the reaction selectively produces H_2, rather than CH_4. These results are consistent with previous studies conducted at 200°C [165], in which the CH_4/H_2 ratio was 3.3 over a 5% Ru/TiO_2 catalyst and 0.4 over 0.5% Ru/TiO_2.

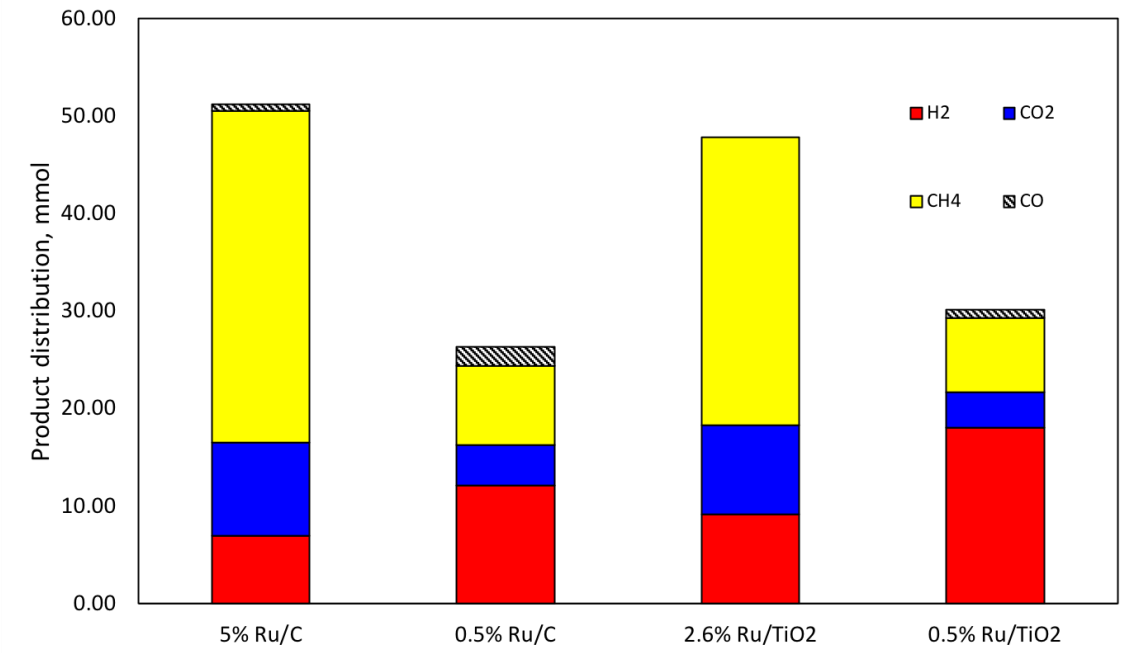

Figure 30. Gas phase product distribution over different Ru catalysts. Reaction conditions: 250 °C 200 psi of Ar; Feed: 15 vol% ethanol aqueous solution with overall volume of 100 mL.

Another important figure of merit to evaluate catalyst performance is the C1/C2 product ratio, listed in Table 13, which is a measure of the relative ability of the catalyst to achieve C-C bond cleavage. Higher C1/C2 ratio indicates more C1 products, which are CO, CO_2 and CH_4 in the gas phase. Similarly, liquid products such as acetaldehyde and acetic acid make up for C2 products and A low C1/C2 ratio signifies that ethanol has further reacted, mainly to liquid products. Our experimental results clearly show that the C1/C2 product ratio is higher on the catalysts with larger particle sizes (i.e., 5% Ru/C > 0.5% Ru/C, and 2.6% Ru/TiO_2 > 0.5% Ru/TiO_2). However, DFT calculation usually show that the energy barriers for C-C bond cleavage are lower on low-coordination-number sites at the corners and step-edges on metal surfaces [84, 166, 167]. A possible explanation could be that the more active, low-coordination sites are more likely to be blocked by the

fragment produced during the initial C-C cleavage, and the binding of these fragments (CO or CH_x) is too strong to easily react with H_2 and regenerate the active site [151]. Other possible deactivation mechanisms are attributed to reactions such as Boudouard reaction, methane decomposition, ethylene polymerization and cracking of ethane[140, 168]. Among all, lower reaction temperature of ethanol reforming potentially promotes carbon deposition through Boudouard reaction as follows:

$$2CO \leftrightarrow CO_2 + C \tag{88}$$

Nevertheless, the solid carbon formation under excess amount of water and low temperature is thermodynamically unfavorable [169, 170].

The phenomenon of site blocking by CO was further demonstrated by investigating the Fischer Tropsch synthesis (FTS) reaction in the aqueous phase over the two catalysts, 5% Ru/C and 0.5% Ru/C. This is a good probe reaction, which is known to involve the C-O dissociation as the rate-limiting step. To make a closer connection with the main reaction of interest for this contribution, the same conditions used in the APR of ethanol were employed for the FTS, with the only difference in the composition of the gas phase, which in this case was kept at a H_2/CO molar mixture ratio of 5. Interestingly, the 0.5% Ru/C catalyst produced mainly CO_2 and additional H_2 in the gas phase, via WGS reaction. By contrast, CO_2 was not observed as a product over 5% Ru/C. Instead, C_1- C_7 alkanes were the main products observed. These results clearly indicate that the small particle 0.5% Ru/C is deactivated by CO to a large extent. That is, the low-coordination (corner, steps) sites present in small Ru particles adsorb CO so strongly that are quickly rendered inactive. CO activation is hard to achieve. The FTS is hindered over low coordinate step edge sites. However 5% Ru/C, surface CO is easier to be activated over with larger Ru particles. By

contrast, adsorption of CO/CO_2 on high coordinate surface sites are much weaker, so these sites are kept clean and active for C-O dissociation and subsequent C-C bond formation to longer chain hydrocarbons.

Carballo *et al*. [171] investigated Ru particle size effects on the FT synthesis ranging from 4 nm to 23 nm. The turnover frequencies (TOF) of H_2 and CO consumption as well as CH_4 formation increases with particle sizes that are smaller than 10 nm. The DFT calculation by Loveless *et al.* [172, 173] further unveils that energy barriers of chemisorbed CO activation on low coordinated corner and step-edge sites are larger than high coordinated flat extended surface. H-assisted CO activation on Ru (111) terrace of Ru_{201} cluster lowers the activation energy to 165 kJ/mol compared to 356 kJ/mol for CO activation without H-assistance at corner sites. Strong adsorption of CO at the corner and step-edge sites greatly blocks the Ru active sites.

6.3.4 Pt particle size effects

All monometallic Pt catalysts exhibit high selectivity towards H_2. The results are plotted in Figure 31. Both 1% Pt/C and 2% Pt/TiO_2 have low production towards CH_4. Meanwhile liquid products such as acetaldehyde, acetic acid and diethyl ether are noteworthy. However, as demonstrated by DFT calculations, ethanol decomposition via C-C cleavage is more difficult on Pt [156] than on Ru [152], as revealed by the calculated energy barriers, 90 kJ/mol for Pt, compared to 38 kJ/mol for Ru. Moreover the C-C cleavage over Pt happens after the surface ketenyl CHCO species via dehydrogenation of Cβ indicating the stronger affinity of Pt to H atoms. Therefore, one should expect that most of the H_2 produced over Pt catalysts derives from dehydrogenation of ethanol. However, since no CO is observed in the gas phase products when Pt is present due to the favorable

WGS reaction at low temperatures one can expect that surface CO converts to CO_2 producing additional H_2. This is in line with previous results of WGS reactions [174], showing that the TOF over Pt is about 6 times higher than over Ru, under same reaction temperatures.

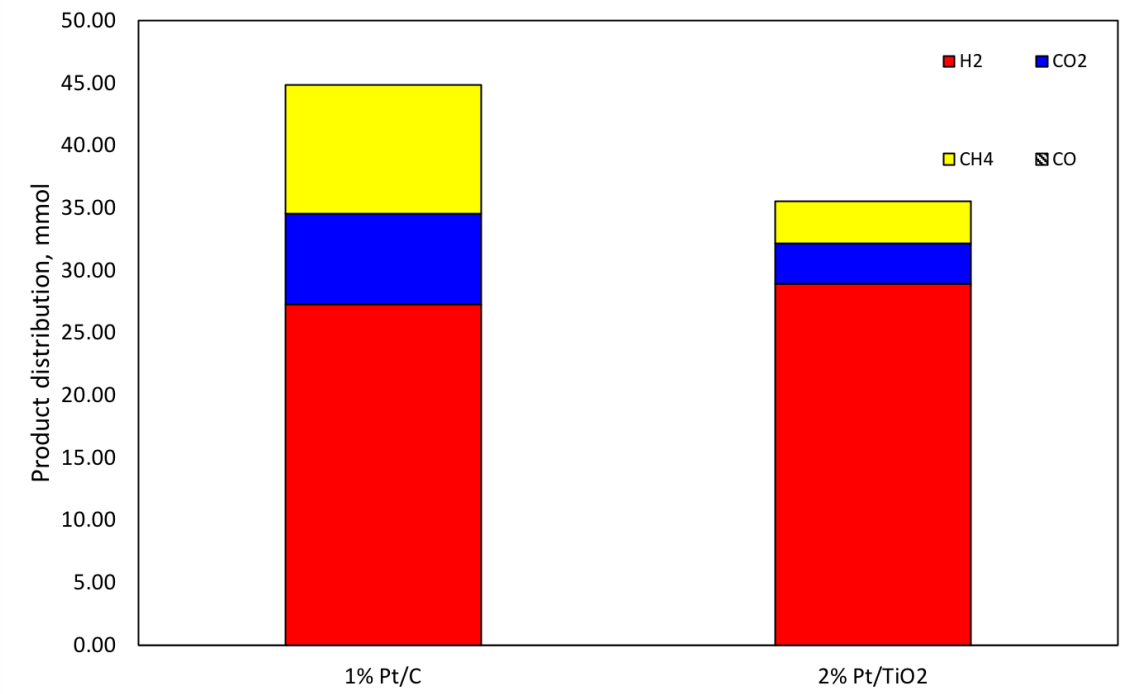

Figure 31. Gas phase product distribution over different Pt catalysts. Reaction conditions: 250 °C 200 psi of Ar; Feed: 15 vol% ethanol aqueous solution with overall volume of 100 mL.

For Pt catalysts, increasing the metal loading from 1 to 2 wt % did not result in a significant change in particle size, as shown in the TEM images and particle size distributions of Figure 28(e-f), i.e. 2.2 nm for 1% Pt/C and 2.4 nm for 2% Pt/TiO_2. The product distributions on these two catalysts were similar, with the 1% Pt/C catalysts producing only slightly more CO_2 and CH_4. Contrasting with Ru, Pt has been shown to have low activity towards the methanation reaction [163]. Indeed, DFT calculations reveal the high activation energy barrier for CO dissociation on a Pt (111) surface, with a C-O

bond length close to the value for free CO [175]. Therefore, H_2 consumption for CH_4 production is practically negligible on Pt. On the other hand, the adsorption and decomposition of ethanol, acetaldehyde and glycerol have been previously investigated over Pt catalysts of different particle size and different planes of Pt single crystals. For instance, Cong *et al.* [176] has investigated the adsorption and desorption of ethanol on Pt (331), which consists of steps and terraces of Pt(111). The step sites display high activity for direct C-C cleavage upon adsorption, while terrace sites catalyze dehydrogenation of ethanol, followed by C-C cleavage. Likewise, the decomposition of acetaldehyde has been studied over Pt catalysts of different particle sizes [177], with the observation that large particles have low activity towards C-C cleavage, reflected by a low rate of acetaldehyde decomposition. Pt particle size effects have also been studied in the APR of glycerol [177, 178], which produces higher selectivity to CH_4 and C1 oxygenates over Pt catalysts of small particle sizes. Finally, several experimental studies agree that WGS reactivity on Pt is independent of particle size [174, 179].

6.3.5 Effect of the support

Supports are not only used to disperse metal particles but they may also promote catalytic activity for some reactions. Our experimental results, summarized in Table 13, indicate that the bare TiO_2 support catalyzes dehydrogenation and dehydration reactions under ethanol APR reaction conditions. Dehydrogenation of ethanol produces H_2 and acetaldehyde, while dehydration of ethanol yields diethyl ether and ethylene, which are observed in moderate amounts. By contrast, no CO, CO_2 or CH_4 is detected, indicating that TiO_2 has no activity for C-C bond cleavage.

On the other hand, TiO_2 exhibits a higher activity towards ethanol conversion than the carbon support, most probably via acid-base interactions. It is possible that an H atom of ethanol, acting as an acid, may interact with a basic site of TiO_2, while the O atom of ethanol may be attracted by a surface Ti^{4+} site, having Lewis acidity [180]. As a result, an ethoxide is formed on the surface of TiO_2. Under the presence of water, the surface ethoxide may further interact with surface OH groups, further dehydrogenating to acetaldehyde [168, 180, 181], which can in turn react to form a surface acetate. Then, when a metal is supported on TiO_2, bifunctional activity may develop [168, 178]. That is, it has been proposed that the acetate species can decompose at the metal-support interface, producing CO, which can undergo WGS reaction, yielding CO_2 and H_2. Guo et al. [182] has suggested that strong basic sites present on a supports could promote the dissociation of water, facilitating the WGS. This idea is consistent with our experimental results (see Table 2), which show that carbon-supported Ru produces much more CO in the gas phase than TiO_2-supported Ru. That is, the sequential conversion of CO via WGS reaction is not promoted on the carbon support as much as it is on TiO_2.

6.3.6 Bimetallic Ru-Pt catalysts

Based on the results shown above, we have selected the bimetallic Ru-Pt catalysts supported on TiO_2 as potentially promising materials that may incorporate the beneficial properties of the support as well as both metals (Ru and Pt), without the negative effects of either. That is, the TiO_2 support may enhance C2 decomposition as well as WGS while Ru catalyze C-C cleavage and Pt enhances WGS. However, we have shown that flat Ru surfaces, with large Ru ensembles, may result in undesired methanation that consumes H_2 and produces CH_4, which is detrimental. At the same time, small Ru particles may lead to

strong adsorption of CO at the low-coordination corner and step-edge sites, poisoning the sites. Alloying with Pt, on the other hand, may simultaneously result in lower density of large Ru ensembles and lower density of uncoordinated defects. Pt itself has low activity towards C-C cleavage, but enhanced WGS.

Table 13 summarizes the results of the APR over the three bimetallic catalysts. Two of them are the sequentially impregnated bimetallics (one Ru first, the other Pt first), while the third one is the co-impregnated (Ru-Pt). The product distributions observed in the gas phase are presented in Figure 33. The behavior of the bimetallic 0.5% Ru/2% Pt/TiO_2 (Ru first) resembles that of the monometallic 2% Pt/TiO_2. This result would suggest that the small Ru loading (0.5 %) deposited first on the support becomes covered by the larger amount of Pt (2%), without much Ru exposure. In the reversed preparation sequence, 2% Pt/0.5% Ru/TiO_2 (Pt first), the added Ru provides enhanced C-C bond cleavage, producing surface CO. But, the abundant liquid products indicate that Pt there is still large fractions of Pt that catalyze dehydrogenation and not enough Ru to break C-C bonds. However, the co-impregnated 2% Pt-1% Ru/TiO_2, with higher Ru loading, demonstrates an excellent performance and not only it provides sufficient C-C cleavage activity upon ethanol adsorption, but high WGS activity to convert the surface CO species with water to produce CO_2 and H_2, but without undergoing methanation. Aiming to detect any interaction between Pt and Ru in the bimetallic Pt-Ru/TiO_2 catalyst, the XRD patterns of 2% Pt/TiO_2, 1% Ru/TiO_2 and 2% Pt-1% Ru/TiO_2 were recorded (see Figure 32). However, only TiO_2 diffraction peaks, composed of anatase and rutile forms, were detected for those three catalysts. Pt and Ru intensities were too weak to be use as a measure of Pt-Ru interactions. This is due to the low loading of Pt and Ru, as well as their high state of dispersion on the

TiO_2 support. A weak peak was observed at 2θ of 40.0° for 2% Pt-1% Ru/ TiO_2 (line a), and 2%Pt/ TiO_2 (line b) catalysts. As depicted in line d, after subtracting the 1%Ru/ TiO_2 (line c) from 2% Pt-1% Ru/ TiO_2 (line a), a weak intensity emerged. This peak corresponds to the Pt(111) diffraction. Similarly, subtracting 1% Ru/ TiO_2 (line c) from 2% Pt/ TiO_2 (line b) should have resulted diffraction patterns for monometallic Pt in line e. However, the intensities for both lines d and e are too similar to identify any Pt-Ru interaction. The same analysis is also conducted to identify Ru diffraction patterns. As indicated in line f, no noticeable intensities have been detected.

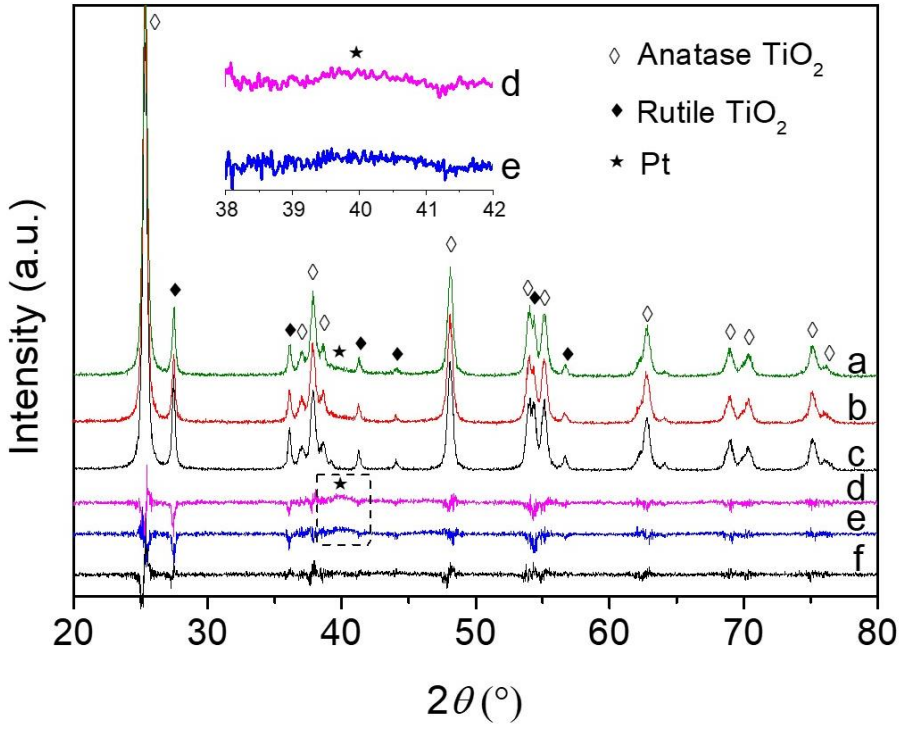

Figure 32. XRD patterns for pre-reduced 2 %Pt-1 %Ru/TiO_2 as line 'a'; 2 %Pt/TiO_2 as line 'b'; 1 %Ru/TiO_2 as line 'c'. The line 'd' shows the difference in intensity between 2 %Pt-1 %Ru/TiO_2 and 1 %Ru/TiO_2; the line 'e' shows the difference in intensity between 2%Pt/TiO_2 and 1%Ru/TiO_2; whereas the line 'f' shows the difference in intensity between 2 %Pt - 1 %Ru/TiO_2 and 2 %Pt/TiO_2.

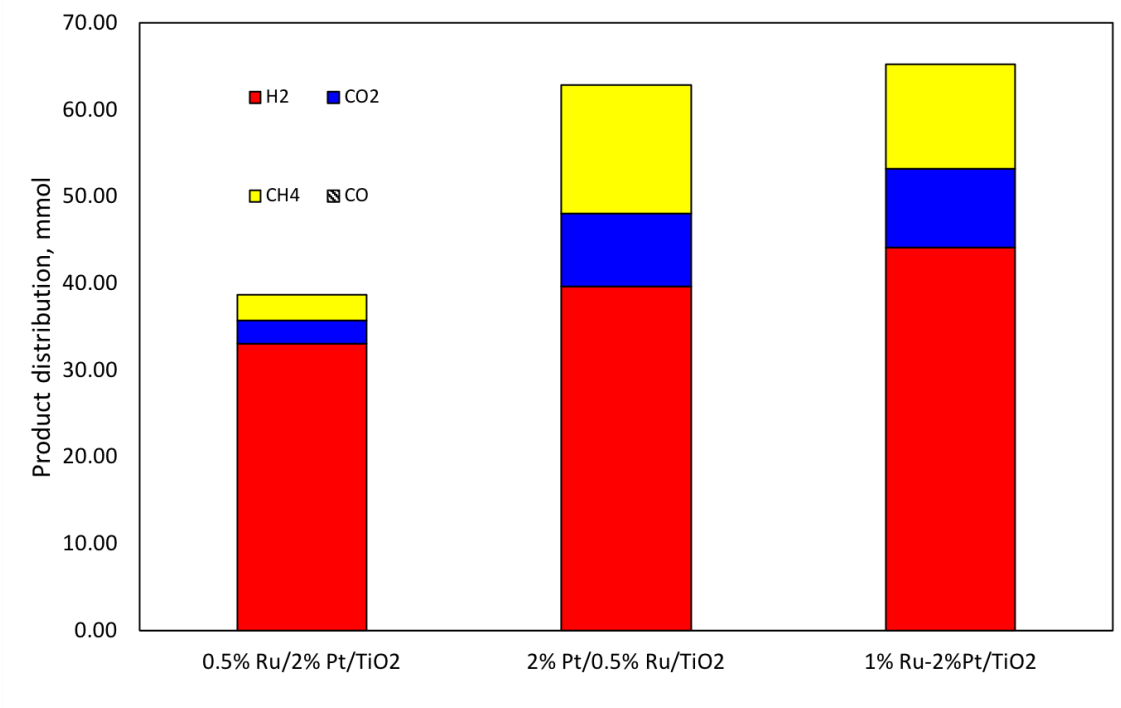

Figure 33. Gas phase product distribution over different Pt-Ru bimetallic catalysts. Reaction conditions: 250 °C 200 psi of Ar; Feed: 15 vol% ethanol aqueous solution with overall volume of 100 mL.

Bimetallic Pt-Ru catalysts have been found to be effective for aqueous phase reforming of biomass, with high catalytic activity towards H_2 production [183, 184]. The multi-objective optimization diagram presented in Figure 34 provides a comprehensive perspective with full assessment of optimal catalysts towards this reaction. Catalysts can be compared on the basis of their H_2 production rate (per gram of catalyst) along with the ratio of COx to C2 products. COx represents the sum of CO_2 and CO; C2 represents the total amount of two-carbon products. The ratio of COx-to-C2 provides a measure of the efficiency of each catalyst for C-C cleavage. Catalyst with maximum potential for APR of ethanol should maximize the yield of H_2 per unit time with maximum utilization of the carbon source. It is clear that all the points for the pure Ru series are located to the left side of the diagram, which is less desirable. While Ru is efficient at C-C cleavage readily

converting C2 products into C1 products the yield of H_2 production is rather low. Large Ru particles tend to dissociate CO easily and produce CH_4 by consuming the desirable product H_2. At the same time, smaller Ru particles display strong adsorption of CO, which is hard to be further converted and lead to site poisoning. On the other hand, while Pt catalysts produce significant amounts of H_2, this conversion is mainly through dehydrogenation of ethanol. Therefore, even though the H_2 production rate is higher than on Ru catalyst the utilization of ethanol is incomplete. That is, the low COx-to-C2 ratios observed for pure Pt catalysts indicates that large amounts of C2 liquid products are required to obtain a given H_2 yield. Finally, the bimetallic catalysts display their points towards to upper right of the diagram because the efficiency of the C-C cleavage is enhanced and the produced CO is further converted via WGS reaction, mostly catalyzed by Pt, which results in maximum H_2 production rate with maximum utilization of ethanol.

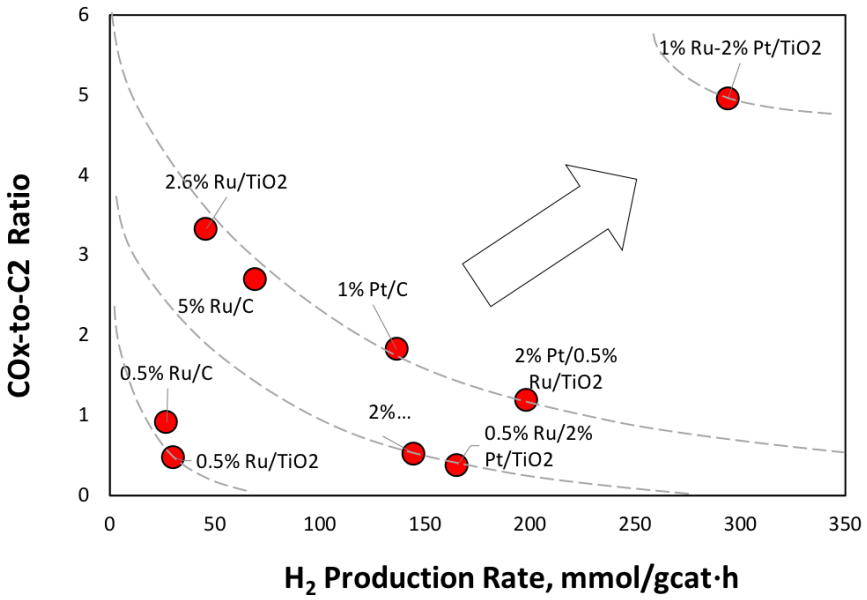

Figure 34. Assessment of catalyst performances based on two desirable ratios: vertical: COx-to-C2 ratio, which indicates the catalyst efficiency for C-C cleavage; horizontal: overall H_2 production rate. The optimal catalysts should appear on the upper right corner of the diagram.

6.4 Conclusion

APR of ethanol demonstrates an efficient route to obtain H_2 with a low energy input and low CO production. The solvent water serves as a reactant and drive reaction equilibrium by converting surface CO to CO_2 and release more H_2.

Monometallic Ru catalysts with large particle sizes display high activity towards C-C cleavage upon ethanol adsorption. However larger Ru also dissociates CO and reacts with H_2 simultaneously to form CH_4 and doesn't accomplish the H_2 production by APR of ethanol. Smaller Ru particle shows high selectivity towards H_2, but the CO species present strong adsorption on low index corner step-edge sites and eventually lower the overall catalytic activity due to the sites poisoning. On the contrary, Pt also reveals high selectivity towards H_2 production and low activity to methanation reaction. The surface CO species are reacted with water via WGS reaction to produce more H_2 and CO_2. However the activation energy of C-C cleavage over Pt is much higher than that over Ru, making ethanol reforming less efficient and yielding more liquid products that needed to be decomposed to convert more ethanol.

Support TiO_2 interacts strongly with ethanol and water through acid-base interaction. Ethanol decomposes upon adsorption and produced acetaldehyde as the dehydrogenation product and ethylene along with diethyl ether as dehydration products. The basicity of TiO_2 is also believed to promote the WGS reaction.

Bimetallic Ru-Pt with 1% Ru co-impregnated with 2% Pt over TiO_2, located at the top right of the optimization diagram, exhibited the beneficial properties of both Ru and Pt without the negative effects of either. Its synergistic behavior results in higher H_2

production rate, higher C-C cleavage ability, and lower methanation rate than any of the monometallic Ru or Pt catalysts.

Acknowledgements

This research has been funded by Abengoa Research.

Chapter 7: Summary

7.1 Kinetics in hydrogenation

To reach a mechanistic understanding of hydrogenation reactions used for biomass conversion, hydrogenation of cyclohexene and furfural has been investigated as the model compound for aromatics and sugar derived molecules.

Four kinetic models have been built to study the adsorption sites of hydrogen/ cyclohexene and rate determining steps. Analysis on reaction orders unveils that H_2 adsorbs on much smaller sites that don't compete with reactant cyclohexene. The interpretation of each term in rate expressions indicates the rate determining step is the first hydrogenation step. In furfural hydrogenation, water assisted H-shuttling mechanism reduced the activation barrier for the first hydrogenation. The experiment results are consistent with the DFT studies. Kinetic measurements in water further verify the second hydrogenation rather than the first hydrogenation becomes the rate determining step in the presence of water. In general, the analysis on reaction rate expressions coupled with measurements on reaction orders can be widely used to study kinetics of reactions.

When finalizing kinetic parameters, there are many sets of fitting values that could be used on a kinetic model to get a good fit. The most important parameters are adsorption equilibrium constants and a rate constant, which are directly determined by entropy and enthalpy of the step. To provide reasonable estimations, statistical thermodynamics can be applied to study molecule adsorptions. By analyzing partition functions of adsorbed species and its original phase, the range of entropy of adsorption is confined. The corresponding enthalpy of adsorption is then obtained and is compared with DFT calculations to further investigate scenarios of surface adsorption. Combing statistical thermodynamics

calculations with DFT calculations, surface reactions are readily modelled and reactions can be predicted in a more efficient and accurate way.

7.2 Solvent effect

Solvents play an essential role in liquid phase reactions for biomass conversion. The observed solvent effects are due to solvent impact on kinetically relevant steps of reactions.

For inert organic solvents, interactions between solvents and catalytic sites lead to competitive adsorption of solvent molecules. Surface coverage of reacting species decreases, resulting in a rate decrease. The stronger solvents compete, the lower the reactivity. Moreover, liquid phase non-ideality demonstrates interactions between molecules within liquid media and can change surface coverages of reacting species. Activity coefficients are applied to quantify non-ideal behaviors of solution mixtures. Solvent and solute interactions could either repel each other or attract each other in bulk phase. Therefore, solvent/solute concentration on catalyst surface will be higher or lower than its bulk phase depending on their non-ideality.

For protic solvent such as water, furfural hydrogenation can be facilitated via water assisted H-shuttling mechanism. The presence of water stabilizes the energy at intermediates and final states through H-bonding, and also participates in the hydrogenation step. Water molecules pick up surface adsorbed H atoms and shuttle it towards the oxygen of the carbonyl group in furfural through H-bonding network. This route has greatly reduced the energy barrier for furfural hydrogenation. In aqueous phase reforming of ethanol, solvent water serves as the reactant that converts surface CO species to CO_2 and H_2 via water-gas-shift (WGS) reaction. Not only the reaction equilibrium is

driven towards more H_2 production, active sites are also quickly removed to prevent strong adsorption of CO that causes deactivation of catalysts.

References

1. Cherubini, F., et al., *CO2 emissions from biomass combustion for bioenergy: atmospheric decay and contribution to global warming.* Gcb Bioenergy, 2011. **3**(5): p. 413-426.

2. Gallezot, P., *Conversion of biomass to selected chemical products.* Chemical Society Reviews, 2012. **41**(4): p. 1538-1558.

3. Alonso, D.M., J.Q. Bond, and J.A. Dumesic, *Catalytic conversion of biomass to biofuels.* Green Chemistry, 2010. **12**(9): p. 1493-1513.

4. Huber, G.W., S. Iborra, and A. Corma, *Synthesis of transportation fuels from biomass: chemistry, catalysts, and engineering.* Chemical reviews, 2006. **106**(9): p. 4044-4098.

5. Resasco, D.E., et al., *5. Furfurals as chemical platform for biofuels production.* Solid Waste as a Renewable Resource: Methodologies, 2011: p. 103.

6. Hayes, D.J., *An examination of biorefining processes, catalysts and challenges.* Catalysis Today, 2009. **145**(1-2): p. 138-151.

7. Bridgwater, A., D. Meier, and D. Radlein, *An overview of fast pyrolysis of biomass.* Organic geochemistry, 1999. **30**(12): p. 1479-1493.

8. Bridgwater, A.V., *Renewable fuels and chemicals by thermal processing of biomass.* Chemical Engineering Journal, 2003. **91**(2-3): p. 87-102.

9. Van der Stelt, M., et al., *Biomass upgrading by torrefaction for the production of biofuels: A review.* Biomass and bioenergy, 2011. **35**(9): p. 3748-3762.

10. Zheng, A., et al., *Effect of torrefaction temperature on product distribution from two-staged pyrolysis of biomass.* Energy & Fuels, 2012. **26**(5): p. 2968-2974.

11. Waters, C., *Understanding Thermochemical Process and Feedstock Compositional Impacts on Strategies to Control Pyrolysis and Torrefaction Product Distributions.* 2016.

12. Zaimes, G.G., et al., *Multistage torrefaction and in situ catalytic upgrading to hydrocarbon biofuels: analysis of life cycle energy use and greenhouse gas emissions.* Energy & Environmental Science, 2017. **10**(5): p. 1034-1050.

13. Bjerkaas, D., *Adsorption of Biomass Torrefaction Vapors on Activated Carbon.* 2017.

14. Herron, J.A., et al., *A Systems‐Level Roadmap for Biomass Thermal Fractionation and Catalytic Upgrading Strategies.* Energy Technology, 2017. **5**(1): p. 130-150.

15. Pham, T.N., D. Shi, and D.E. Resasco, *Evaluating strategies for catalytic upgrading of pyrolysis oil in liquid phase.* Applied Catalysis B: Environmental, 2014. **145**: p. 10-23.

16. Gumidyala, A., T. Sooknoi, and S. Crossley, *Selective ketonization of acetic acid over HZSM-5: The importance of acyl species and the influence of water.* Journal of Catalysis, 2016. **340**: p. 76-84.

17. Zhang, L., et al., *Synthesis of C4 and C8 Chemicals from Ethanol on MgO‐Incorporated Faujasite Catalysts with Balanced Confinement Effects and Basicity.* ChemSusChem, 2016. **9**(7): p. 736-748.

18. Sanna, A., T.P. Vispute, and G.W. Huber, *Hydrodeoxygenation of the aqueous fraction of bio-oil with Ru/C and Pt/C catalysts.* Applied Catalysis B: Environmental, 2015. **165**: p. 446-456.

19. Nie, L. and D.E. Resasco, *Kinetics and mechanism of m-cresol hydrodeoxygenation on a Pt/SiO 2 catalyst.* Journal of Catalysis, 2014. **317**: p. 22-29.

20. Cortright, R., R. Davda, and J.A. Dumesic, *Hydrogen from catalytic reforming of biomass-derived hydrocarbons in liquid water.* Nature, 2002. **418**(6901): p. 964-967.

21. Davda, R., et al., *A review of catalytic issues and process conditions for renewable hydrogen and alkanes by aqueous-phase reforming of oxygenated hydrocarbons over supported metal catalysts.* Applied Catalysis B: Environmental, 2005. **56**(1): p. 171-186.

22. Chheda, J.N., G.W. Huber, and J.A. Dumesic, *Liquid-phase catalytic processing of biomass-derived oxygenated hydrocarbons to fuels and chemicals.* Angewandte Chemie-International Edition, 2007. **46**(38): p. 7164-7183.

23. Bond, G. and P. Wells, *The mechanism of the hydrogenation of unsaturated hydrocarbons on transition metal catalysts*, in *Advances in Catalysis*. 1965, Elsevier. p. 91-226.

24. Chorkendorff, I. and J.W. Niemantsverdriet, *Concepts of modern catalysis and kinetics*. 2017: John Wiley & Sons.

25. Atkins, P. and J. De Paula, *Atkins' physical chemistry.* New York, 2006: p. 77.

26. Laidler, K.J., *Chemical kinetics*. 1987.

27. Vannice, M.A. and W.H. Joyce, *Kinetics of catalytic reactions*. Vol. 134. 2005: Springer.

28. Boudart, M., *Kinetics of Chemical Processes: Butterworth-Heinemann Series in Chemical Engineering*. 2014: Elsevier.

29. Reichardt, C. and T. Welton, *Solvents and solvent effects in organic chemistry*. 2011: John Wiley & Sons.

30. Crossley, S., et al., *Solid nanoparticles that catalyze biofuel upgrade reactions at the water/oil interface.* Science, 2010. **327**(5961): p. 68-72.

31. Buncel, E. and H. Wilson, *Initial-state and transition-state solvent effects on reaction rates and the use of thermodynamic transfer functions.* Accounts of Chemical Research, 1979. **12**(1): p. 42-48.

32. Walrafen, G., *Water: a Comprehensive Treatise, edited by F. Franks*. 1972, Plenum Press, New York and Londonl.

33. Blandamer, M.J. and J. Burgess, *Initial state and transition state solvation in inorganic reactions.* Coordination Chemistry Reviews, 1980. **31**(2): p. 93-121.

34. Madon, R.J. and E. Iglesia, *Catalytic reaction rates in thermodynamically non-ideal systems.* Journal of Molecular Catalysis A: Chemical, 2000. **163**(1): p. 189-204.

35. Madon, R., J. O'connell, and M. Boudart, *Catalytic hydrogenation of cyclohexene: Part II. Liquid phase reaction on supported platinum in a gradientless slurry reactor.* AIChE Journal, 1978. **24**(5): p. 904-911.

36. Gonzo, E. and M. Boudart, *Catalytic hydrogenation of cyclohexene: 3. Gas-phase and liquid-phase reaction on supported palladium.* Journal of Catalysis, 1978. **52**(3): p. 462-471.

37. Vaidya, M.J., S.M. Kulkarni, and R.V. Chaudhari, *Synthesis of p-aminophenol by catalytic hydrogenation of p-nitrophenol.* Organic process research & development, 2003. **7**(2): p. 202-208.

38. Toukoniitty, E., et al., *Enantioselective hydrogenation of 1-phenyl-1, 2-propanedione.* Journal of Catalysis, 2001. **204**(2): p. 281-291.

39. Bertero, N.M., et al., *Solvent effect in the liquid-phase hydrogenation of acetophenone over Ni/SiO2: A comprehensive study of the phenomenon.* Applied Catalysis A: General, 2011. **394**(1-2): p. 228-238.

40. Mukherjee, S. and M.A. Vannice, *Solvent effects in liquid-phase reactions II. Kinetic modeling for citral hydrogenation.* Journal of Catalysis, 2006. **243**(1): p. 131-148.

41. Toukoniitty, E., et al., *Solvent effects in enantioselective hydrogenation of 1-phenyl-1, 2-propanedione.* Journal of Molecular Catalysis A: Chemical, 2003. **192**(1): p. 135-151.

42. Nikoshvili, L., et al., *Selective hydrogenation of 2-methyl-3-butyn-2-ol over Pd-nanoparticles stabilized in hypercrosslinked polystyrene: Solvent effect.* Catalysis Today, 2015. **241**: p. 179-188.

43. Drelinkiewicza, A., et al., *Acetophenone hydrogenation on polymer–palladium catalysts. The effect of polymer matrix.* Catalysis Letters, 2004. **94**(3-4): p. 143-156.

44. Mukherjee, S., *Solvent effects in liquid-phase hydrogenation reactions*. 2005.

45. Lo, H. and M. Paulaitis, *Estimation of solvent effects on chemical reaction rates using UNIFAC group contribution.* AIChE Journal, 1981. **27**(5): p. 842-844.

46. Rajadhyaksha, R. and S. Karwa, *Solvent effects in catalytic hydrogenation.* Chemical engineering science, 1986. **41**(7): p. 1765-1770.

47. Boudart, M. and G. Djéga-Mariadassou, *Kinetics of heterogeneous catalytic reactions*. 2014: Princeton University Press.

48. Singh, U.K. and M.A. Vannice, *Kinetic and thermodynamic analysis of liquid‐phase benzene hydrogenation.* AIChE journal, 1999. **45**(5): p. 1059-1071.

49. Rautanen, P.A., J.R. Aittamaa, and A.O.I. Krause, *Solvent effect in liquid-phase hydrogenation of toluene.* Industrial & engineering chemistry research, 2000. **39**(11): p. 4032-4039.

50. Augustine, R.L. and P. Techasauvapak, *Heterogeneous catalysis in organic synthesis. Part 9. Specific site solvent effects in catalytic hydrogenations.* Journal of molecular catalysis, 1994. **87**(1): p. 95-105.

51. Kishida, S. and S. Teranishi, *Kinetics of liquid-phase hydrogenation of acetone over Raney nickel catalyst.* Journal of Catalysis, 1968. **12**(1): p. 90-96.

52. Akpa, B., et al., *Solvent effects in the hydrogenation of 2-butanone.* Journal of catalysis, 2012. **289**: p. 30-41.

53. Hibbitts, D.D., et al., *Mechanistic role of water on the rate and selectivity of Fischer–Tropsch synthesis on ruthenium catalysts.* Angewandte Chemie International Edition, 2013. **52**(47): p. 12273-12278.

54. Hronec, M., K. Fulajtarová, and T. Liptaj, *Effect of catalyst and solvent on the furan ring rearrangement to cyclopentanone.* Applied Catalysis A: General, 2012. **437**: p. 104-111.

55. Taylor, C.D. and M. Neurock, *Theoretical insights into the structure and reactivity of the aqueous/metal interface.* Current Opinion in Solid State and Materials Science, 2005. **9**(1-2): p. 49-65.

56. Singh, U.K. and M.A. Vannice, *Kinetics of liquid-phase hydrogenation reactions over supported metal catalysts—a review.* Applied Catalysis A: General, 2001. **213**(1): p. 1-24.

57. Červený, L., B. Vostrý, and V. Růžička, *Hydrogen solubility in organic solvents and adsorption from them on catalyst surface.* Collection of Czechoslovak Chemical Communications, 1981. **46**(8): p. 1965-1969.

58. He, J., C. Zhao, and J.A. Lercher, *Impact of solvent for individual steps of phenol hydrodeoxygenation with Pd/C and HZSM-5 as catalysts.* Journal of Catalysis, 2014. **309**: p. 362-375.

59. Shi, D., et al., *Enhanced Activity and Selectivity of Fischer–Tropsch Synthesis Catalysts in Water/Oil Emulsions.* ACS catalysis, 2014. **4**(6): p. 1944-1952.

60. Wilds, A., *Reduction with aluminum alkoxides.* Organic Reactions, 1944.

61. Cohen, R., et al., *The mechanism of aluminum-catalyzed Meerwein− Schmidt− Ponndorf− Verley reduction of carbonyls to alcohols.* Journal of the American Chemical Society, 2004. **126**(45): p. 14796-14803.

62. Michel, C., et al., *Role of water in metal catalyst performance for ketone hydrogenation: a joint experimental and theoretical study on levulinic acid conversion into gamma-valerolactone.* Chemical Communications, 2014. **50**(83): p. 12450-12453.

63. Yoon, Y., et al., *First-principles study of phenol hydrogenation on Pt and Ni catalysts in aqueous phase.* Journal of the American Chemical Society, 2014. **136**(29): p. 10287-10298.

64. Hibbitts, D.D., et al., *Mechanistic Role of Water on the Rate and Selectivity of Fischer-Tropsch Synthesis on Ruthenium Catalysts.* Angewandte Chemie-International Edition, 2013. **52**(47): p. 12273-12278.

65. Agmon, N., *The grotthuss mechanism.* Chemical Physics Letters, 1995. **244**(5-6): p. 456-462.

66. Merte, L.R., et al., *Water-mediated proton hopping on an iron oxide surface.* Science, 2012. **336**(6083): p. 889-893.

67. Bridgwater, A.V., *Review of fast pyrolysis of biomass and product upgrading.* Biomass & Bioenergy, 2012. **38**: p. 68-94.

68. Saeys, M., et al., *First-principles based kinetic model for the hydrogenation of toluene.* Journal of Catalysis, 2005. **236**(1): p. 129-138.

69. Segal, E., R. Madon, and M. Boudart, *Catalytic hydrogenation of cyclohexene: I. Vapor-phase reaction on supported platinum.* Journal of Catalysis, 1978. **52**(1): p. 45-49.

70. Boudart, M. and W. Cheng, *Catalytic hydrogenation of cyclohexene: 7. Liquid phase reaction on supported nickel.* Journal of Catalysis, 1987. **106**(1): p. 134-143.

71. Boudart, M. and D. Sajkowski, *Catalytic hydrogenation of cyclohexene: liquid-phase reaction on rhodium.* Faraday Discussions, 1991. **92**: p. 57-67.

72. Chen, Y.-W. and C. Li, *Liquid phase hydrogenation of cyclohexene over Pt/aluminum borate catalyst.* Catalysis letters, 1992. **13**(4): p. 359-361.

73. Lu, S., et al., *Low temperature hydrogenation of benzene and cyclohexene: a comparative study between γ-Al 2 O 3 supported PtCo and PtNi bimetallic catalysts.* Journal of Catalysis, 2008. **259**(2): p. 260-268.

74. Rioux, R., et al., *Influence of particle size on reaction selectivity in cyclohexene hydrogenation and dehydrogenation over silica-supported monodisperse Pt particles.* Catalysis letters, 2008. **126**(1-2): p. 10.

75. Struijk, J. and J. Scholten, *Selectivity to cyclohexenes in the liquid phase hydrogenation of benzene and toluene over ruthenium catalysts, as influenced by reaction modifiers.* Applied Catalysis A: General, 1992. **82**(2): p. 277-287.

76. Dynys, F.W. and J.W. Halloran, *Alpha alumina formation in alum‐derived gamma alumina.* Journal of the American Ceramic Society, 1982. **65**(9): p. 442-448.

77. Denning, A.L., et al., *Deoxydehydration of Glycols Catalyzed by Carbon‐Supported Perrhenate.* ChemCatChem, 2013. **5**(12): p. 3567-3570.

78. Sitthisa, S. and D.E. Resasco, *Hydrodeoxygenation of furfural over supported metal catalysts: a comparative study of Cu, Pd and Ni.* Catalysis letters, 2011. **141**(6): p. 784-791.

79. Silverstein, R.M., et al., *Spectrometric identification of organic compounds*. 2014: John wiley & sons.

80. Bergeret, G. and P. Gallezot, *Particle size and dispersion measurements.* Handbook of heterogeneous catalysis, 2008.

81. Callister, W.D., *Fundamentals of materials science and engineering*. Vol. 471660817. 2000: Wiley London.

82. Slater, J.C., *Atomic radii in crystals.* The Journal of Chemical Physics, 1964. **41**(10): p. 3199-3204.

83. Rao, R.S., R.T.K. Baker, and M.A. Vannice, *Furfural hydrogenation over carbon - supported copper.* Catalysis Letters, 1999. **60**(1-2): p. 51-57.

84. Watwe, R.M., et al., *Theoretical studies of stability and reactivity of C2 hydrocarbon species on Pt clusters, Pt (111), and Pt (211).* The Journal of Physical Chemistry B, 2000. **104**(10): p. 2299-2310.

85. Eberhardt, W., S.G. Louie, and E. Plummer, *Interaction of hydrogen with a Pd (111) surface.* Physical Review B, 1983. **28**(2): p. 465.

86. Mitsui, T., et al., *Dissociative hydrogen adsorption on palladium requires aggregates of three or more vacancies.* Nature, 2003. **422**(6933): p. 705-707.

87. Watson, G.W., et al., *A comparison of the adsorption and diffusion of hydrogen on the {111} surfaces of Ni, Pd, and Pt from density functional theory calculations.* The Journal of Physical Chemistry B, 2001. **105**(21): p. 4889-4894.

88. Abrams, D.S. and J.M. Prausnitz, *Statistical thermodynamics of liquid mixtures: a new expression for the excess Gibbs energy of partly or completely miscible systems.* AIChE Journal, 1975. **21**(1): p. 116-128.

89. Elliott, J.R. and C.T. Lira, *Introductory chemical engineering thermodynamics*. 1999: Prentice Hall PTR Upper Saddle River, NJ.

90. Haida, O., H. Suga, and S. Seki, *Calorimetric Study of the Glassy State. XI. Plural Glass Transition Phenomena of Cyclohexene.* Bulletin of the Chemical Society of Japan, 1977. **50**(4): p. 802-809.

91. Cox, J., D.D. Wagman, and V.A. Medvedev, *CODATA key values for thermodynamics*. 1989: Chem/Mats-Sci/E.

92. Beckett, C., N. Freeman, and K.S. Pitzer, *The Thermodynamic Properties and Molecular Structure of Cyclopentene and Cyclohexene1*. Journal of the American Chemical Society, 1948. **70**(12): p. 4227-4230.

93. Scharpen, L.H., J.E. Wollrab, and D.P. Ames, *Microwave spectrum, structure, and dipole moment of cyclohexene.* The Journal of Chemical Physics, 1968. **49**(5): p. 2368-2372.

94. Chiang, J.F. and S.H. Bauer, *Molecular structure of cyclohexene.* Journal of the American Chemical Society, 1969. **91**(8): p. 1898-1901.

95. Gates, J. and L. Kesmodel, *EELS analysis of the low temperature phase of ethylene chemisorbed on Pd (111).* Surface Science Letters, 1982. **120**(2): p. L461-L467.

96. Campbell, C.T. and J.R. Sellers, *The entropies of adsorbed molecules.* Journal of the American Chemical Society, 2012. **134**(43): p. 18109-18115.

97. Greeley, J. and M. Mavrikakis, *Surface and subsurface hydrogen: Adsorption properties on transition metals and near-surface alloys.* The Journal of Physical Chemistry B, 2005. **109**(8): p. 3460-3471.

98. Yamauchi, M., et al., *Nanosize effects on hydrogen storage in palladium.* The Journal of Physical Chemistry C, 2008. **112**(9): p. 3294-3299.

99. Ihm, H., et al., *Calorimetric measurement of the heat of adsorption of benzene on Pt (111).* The Journal of Physical Chemistry B, 2004. **108**(38): p. 14627-14633.

100. Lee, A.F., et al., *On the coverage-dependent adsorption geometry of benzene adsorbed on Pd {111}: a study by fast XPS and NEXAFS.* The Journal of Physical Chemistry B, 2000. **104**(49): p. 11729-11733.

101. Lytken, O., et al., *Energetics of cyclohexene adsorption and reaction on Pt (111) by low-temperature microcalorimetry.* Journal of the American Chemical Society, 2008. **130**(31): p. 10247-10257.

102. Johansson, M., et al., *Hydrogen adsorption on palladium and palladium hydride at 1 bar.* Surface science, 2010. **604**(7-8): p. 718-729.

103. Temkin, M. and V. Pyzhev, *Kinetics of ammonia synthesis on promoted iron catalysts.* Acta physiochim. URSS, 1940. **12**(3): p. 217-222.

104. Chou, P. and M.A. Vannice, *Benzene hydrogenation over supported and unsupported palladium: II. Reaction model.* Journal of Catalysis, 1987. **107**(1): p. 140-153.

105. Mellmer, M.A., et al., *Solvent Effects in Acid-Catalyzed Biomass Conversion Reactions.* Angewandte Chemie-International Edition, 2014. **53**(44): p. 11872-11875.

106. Saavedra, J., et al., *The critical role of water at the gold-titania interface in catalytic CO oxidation.* Science, 2014. **345**(6204): p. 1599-1602.

107. Zope, B.N., et al., *Reactivity of the gold/water interface during selective oxidation catalysis.* Science, 2010. **330**(6000): p. 74-78.

108. Wan, H.J., et al., *Kinetic investigations of unusual solvent effects during Ru/C catalyzed hydrogenation of model oxygenates.* Journal of Catalysis, 2014. **309**: p. 174-184.

109. Lange, J.P., et al., *Furfural—a promising platform for lignocellulosic biofuels.* ChemSusChem, 2012. **5**(1): p. 150-166.

110. Corma, A., S. Iborra, and A. Velty, *Chemical routes for the transformation of biomass into chemicals.* Chemical Reviews, 2007. **107**(6): p. 2411-2502.

111. Panagiotopoulou, P., N. Martin, and D.G. Vlachos, *Effect of hydrogen donor on liquid phase catalytic transfer hydrogenation of furfural over a Ru/RuO2/C catalyst.* Journal of Molecular Catalysis a-Chemical, 2014. **392**: p. 223-228.

112. Maldonado, G.M.G., et al., *Experimental and theoretical studies of the acid-catalyzed conversion of furfuryl alcohol to levulinic acid in aqueous solution.* Energy & Environmental Science, 2012. **5**(5): p. 6981-6989.

113. Serrano-Ruiz, J.C., R. Luque, and A. Sepulveda-Escribano, *Transformations of biomass-derived platform molecules: from high added-value chemicals to fuels via aqueous-phase processing.* Chemical Society Reviews, 2011. **40**(11): p. 5266-5281.

114. Sitthisa, S., et al., *Conversion of furfural and 2-methylpentanal on Pd/SiO2 and Pd-Cu/SiO2 catalysts.* Journal of Catalysis, 2011. **280**(1): p. 17-27.

115. Sitthisa, S., W. An, and D.E. Resasco, *Selective conversion of furfural to methylfuran over silica-supported Ni-Fe bimetallic catalysts.* Journal of Catalysis, 2011. **284**(1): p. 90-101.

116. Vorotnikov, V., G. Mpourmpakis, and D.G. Vlachos, *DFT Study of Furfural Conversion to Furan, Furfuryl Alcohol, and 2-Methylfuran on Pd(111).* Acs Catalysis, 2012. **2**(12): p. 2496-2504.

117. Pang, S.H. and J.W. Medlin, *Adsorption and Reaction of Furfural and Furfuryl Alcohol on Pd(111): Unique Reaction Pathways for Multifunctional Reagents.* Acs Catalysis, 2011. **1**(10): p. 1272-1283.

118. Wang, S.G., V. Vorotnikov, and D.G. Vlachos, *Coverage-Induced Conformational Effects on Activity and Selectivity: Hydrogenation and Decarbonylation of Furfural on Pd(111).* Acs Catalysis, 2015. **5**(1): p. 104-112.

119. Pang, S.H., et al., *Effects of Thiol Modifiers on the Kinetics of Furfural Hydrogenation over Pd Catalysts.* Acs Catalysis, 2014. **4**(9): p. 3123-3131.

120. Pang, S.H., et al., *Directing reaction pathways by catalyst active-site selection using self- assembled monolayers.* Nature Communications, 2013. **4**.

121. Vaidya, P.D. and V.V. Mahajani, *Kinetics of liquid-phase hydrogenation of furfuraldehyde to furfuryl alcohol over a Pt/C catalyst.* Industrial & Engineering Chemistry Research, 2003. **42**(17): p. 3881-3885.

122. Merlo, A.B., et al., *Bimetallic PtSn catalyst for the selective hydrogenation of furfural to furfuryl alcohol in liquid-phase.* Catalysis Communications, 2009. **10**(13): p. 1665-1669.

123. Lee, J.C., Y. Xu, and G.W. Huber, *High-throughput screening of monometallic catalysts for aqueous-phase hydrogenation of biomass-derived oxygenates.* Applied Catalysis B-Environmental, 2013. **140**: p. 98-107.

124. Fulajtarova, K., et al., *Aqueous phase hydrogenation of furfural to furfuryl alcohol over Pd-Cu catalysts.* Applied Catalysis a-General, 2015. **502**: p. 78-85.

125. Frainier, L.J. and H.H. Fineberg, *Copper chromite catalyst for preparation of furfuryl alcohol from furfural*. 1979: US.

126. Villaverde, M.M., et al., *Selective liquid-phase hydrogenation of furfural to furfuryl alcohol over Cu-based catalysts.* Catalysis Today, 2013. **213**: p. 87-92.

127. Hronec, M. and K. Fulajtarova, *Selective transformation of furfural to cyclopentanone.* Catalysis Communications, 2012. **24**: p. 100-104.

128. Ordomsky, V.V., et al., *Biphasic single-reactor process for dehydration of xylose and hydrogenation of produced furfural.* Applied Catalysis a-General, 2013. **451**: p. 6-13.

129. Zhang, L., et al., *Improving the selectivity to C4 products in the aldol condensation of acetaldehyde in ethanol over faujasite zeolites.* Applied Catalysis A: General, 2015. **504**: p. 119-129.

130. Chambers, R.P. and M. Boudart, *Lack of dependence of conversion on flow rate in catalytic studies.* Journal of Catalysis, 1966. **6**(1): p. 141-145.

131. Rajashekharam, M., et al., *Hydrogenation of acetophenone using a 10% Ni supported on zeolite Y catalyst: kinetics and reaction mechanism.* Catalysis today, 1999. **48**(1): p. 83-92.

132. Wan, H., et al., *Kinetic investigations of unusual solvent effects during Ru/C catalyzed hydrogenation of model oxygenates.* Journal of Catalysis, 2014. **309**: p. 174-184.

133. Ramachandran, P. and R. Chaudhari, *Three-phase catalytic reactors*. Vol. 2. 1983: Gordon & Breach Science Pub.

134. Hu, X., et al., *Polymerization on heating up of bio‐oil: A model compound study.* AIChE Journal, 2013. **59**(3): p. 888-900.

135. Huang, H., et al., *Effect of water on Cu/Zn catalyst for hydrogenation of fatty methyl ester to fatty alcohol.* Korean Journal of Chemical Engineering, 2009. **26**(6): p. 1574-1579.

136. Sadaba, I., et al., *Deactivation of solid catalysts in liquid media: the case of leaching of active sites in biomass conversion reactions.* Green Chemistry, 2015. **17**(8): p. 4133-4145.

137. Nakagawa, Y., et al., *Total hydrogenation of furfural and 5-hydroxymethylfurfural over supported Pd–Ir Alloy catalyst.* ACS Catalysis, 2014. **4**(8): p. 2718-2726.

138. Barreto, L., A. Makihira, and K. Riahi, *The hydrogen economy in the 21st century: a sustainable development scenario.* International Journal of Hydrogen Energy, 2003. **28**(3): p. 267-284.

139. Haryanto, A., et al., *Current status of hydrogen production techniques by steam reforming of ethanol: a review.* Energy & Fuels, 2005. **19**(5): p. 2098-2106.

140. Ni, M., D.Y. Leung, and M.K. Leung, *A review on reforming bio-ethanol for hydrogen production.* International Journal of Hydrogen Energy, 2007. **32**(15): p. 3238-3247.

141. Liguras, D.K., D.I. Kondarides, and X.E. Verykios, *Production of hydrogen for fuel cells by steam reforming of ethanol over supported noble metal catalysts.* Applied Catalysis B: Environmental, 2003. **43**(4): p. 345-354.

142. Zhang, B., et al., *Hydrogen production from steam reforming of ethanol and glycerol over ceria-supported metal catalysts.* International Journal of Hydrogen Energy, 2007. **32**(13): p. 2367-2373.

143. Huber, G.W. and J.A. Dumesic, *An overview of aqueous-phase catalytic processes for production of hydrogen and alkanes in a biorefinery.* Catalysis Today, 2006. **111**(1): p. 119-132.

144. Rabe, S., et al., *Towards understanding the catalytic reforming of biomass in supercritical water.* Angewandte Chemie International Edition, 2010. **49**(36): p. 6434-6437.

145. Petrović, Ž., et al., *Formation of RuO2 nanoparticles by thermal decomposition of Ru(NO)(NO3)3.* Ceramics International, 2015. **41**(6): p. 7811-7815.

146. Nie, L. and D.E. Resasco, *Kinetics and mechanism of m-cresol hydrodeoxygenation on a Pt/SiO2 catalyst.* Journal of Catalysis, 2014. **317**: p. 22-29.

147. Omotoso, T., S. Boonyasuwat, and S.P. Crossley, *Understanding the role of TiO2crystal structure on the enhanced activity and stability of Ru/TiO2catalysts for the conversion of lignin-derived oxygenates.* Green Chem., 2014. **16**(2): p. 645-652.

148. Tokarev, A., et al., *The role of bio-ethanol in aqueous phase reforming to sustainable hydrogen.* International journal of hydrogen energy, 2010. **35**(22): p. 12642-12649.

149. Wetchakun, N., et al., *Influence of calcination temperature on anatase to rutile phase transformation in TiO 2 nanoparticles synthesized by the modified sol–gel method.* Materials Letters, 2012. **82**: p. 195-198.

150. Van Santen, R.A., *Complementary structure sensitive and insensitive catalytic relationships.* Accounts of chemical research, 2008. **42**(1): p. 57-66.

151. Ferrin, P., et al., *Modeling ethanol decomposition on transition metals: a combined application of scaling and Brønsted− Evans− Polanyi relations.* Journal of the American Chemical Society, 2009. **131**(16): p. 5809-5815.

152. Chiu, C.-c., A. Genest, and N. Rösch, *Decomposition of Ethanol Over Ru (0001): A DFT Study.* Topics in Catalysis, 2013. **56**(11): p. 874-884.

153. Alcala, R., M. Mavrikakis, and J.A. Dumesic, *DFT studies for cleavage of C-C and C-O bonds in surface species derived from ethanol on Pt (111).* Journal of Catalysis, 2003. **218**(1): p. 178-190.

154. Dancini-Pontes, I., et al., *Insights into ethanol decomposition over Pt: A DFT energy decomposition analysis for the reaction mechanism leading to C 2 H 6 and CH 4.* Applied Catalysis A: General, 2015. **491**: p. 86-93.

155. Gursahani, K.I., et al., *Reaction kinetics measurements and analysis of reaction pathways for conversions of acetic acid, ethanol, and ethyl acetate over silica-supported Pt.* Applied Catalysis A: General, 2001. **222**(1): p. 369-392.

156. Sutton, J.E., et al., *Combined DFT, microkinetic, and experimental study of ethanol steam reforming on Pt.* The Journal of Physical Chemistry C, 2013. **117**(9): p. 4691-4706.

157. Liu, B. and J. Greeley, *Density functional theory study of selectivity considerations for C–C versus C–O bond scission in glycerol decomposition on Pt (111).* Topics in Catalysis, 2012. **55**(5-6): p. 280-289.

158. Coslovich, G. and E. Vesselli, *Modelling of ethanol decomposition on Pt (111): a comparison with experiment and density functional theory.* Journal of physics: Condensed matter, 2005(39): p. 6139-6148.

159. Henderson, M.A., Y. Zhou, and J. White, *Polymerization and decomposition of acetaldehyde on rutherium (001).* Journal of the American Chemical Society, 1989. **111**(4): p. 1185-1193.

160. Ciambelli, P., V. Palma, and A. Ruggiero, *Low temperature catalytic steam reforming of ethanol. 2. Preliminary kinetic investigation of Pt/CeO 2 catalysts.* Applied Catalysis B: Environmental, 2010. **96**(1): p. 190-197.

161. Rossi, C., et al., *Thermodynamic analysis of steam reforming of ethanol and glycerine for hydrogen production.* international journal of hydrogen energy, 2009. **34**(1): p. 323-332.

162. Smith, R., M. Loganathan, and M.S. Shantha, *A review of the water gas shift reaction kinetics.* International Journal of Chemical Reactor Engineering, 2010. **8**(1).

163. Vannice, M., *The catalytic synthesis of hydrocarbons from H2CO mixtures over the Group VIII metals: V. The catalytic behavior of silica-supported metals.* Journal of Catalysis, 1977. **50**(2): p. 228-236.

164. Wei, W. and G. Jinlong, *Methanation of carbon dioxide: an overview.* Frontiers of Chemical Science and Engineering, 2011. **5**(1): p. 2-10.

165. Nozawa, T., et al., *Aqueous phase reforming of ethanol and acetic acid over TiO 2 supported Ru catalysts.* Applied Catalysis B: Environmental, 2014. **146**: p. 221-226.

166. Chen, Y. and D.G. Vlachos, *Hydrogenation of ethylene and dehydrogenation and hydrogenolysis of ethane on Pt (111) and Pt (211): a density functional theory study.* The Journal of Physical Chemistry C, 2010. **114**(11): p. 4973-4982.

167. Yang, M.-L., et al., *DFT study of propane dehydrogenation on Pt catalyst: effects of step sites.* Physical Chemistry Chemical Physics, 2011. **13**(8): p. 3257-3267.

168. Hou, T., et al., *Hydrogen production from ethanol reforming: Catalysts and reaction mechanism.* Renewable and Sustainable Energy Reviews, 2015. **44**: p. 132-148.

169. Garcia, E. and M. Laborde, *Hydrogen production by the steam reforming of ethanol: thermodynamic analysis.* International Journal of Hydrogen Energy, 1991. **16**(5): p. 307-312.

170. Liu, S., et al., *Thermodynamic analysis of hydrogen production from oxidative steam reforming of ethanol.* Energy & Fuels, 2008. **22**(2): p. 1365-1370.

171. Carballo, J.M.G., et al., *Catalytic effects of ruthenium particle size on the Fischer–Tropsch Synthesis.* Journal of Catalysis, 2011. **284**(1): p. 102-108.

172. Loveless, B., *CO Bond Activation and CC Bond Formation Paths in Catalytic CO Hydrogenation.* 2012.

173. Loveless, B.T., et al., *CO chemisorption and dissociation at high coverages during CO hydrogenation on Ru catalysts.* Journal of the American Chemical Society, 2013. **135**(16): p. 6107-6121.

174. Panagiotopoulou, P. and D.I. Kondarides, *Effect of morphological characteristics of TiO 2-supported noble metal catalysts on their activity for the water–gas shift reaction.* Journal of catalysis, 2004. **225**(2): p. 327-336.

175. Souza Monteiro, R., et al., *Modeling the Adsorption of CO on Small Pt, Fe and Co Clusters for the Fischer-Tropsch Synthesis.* Journal of cluster science, 2008. **19**(4): p. 601-614.

176. Cong, Y., V. Van Spaendonk, and R. Masel, *Low temperature C-C bond scission during ethanol decomposition on Pt (331).* Surface science, 1997. **385**(2): p. 246-258.

177. Ciftci, A., D. Michel, and E.J. Hensen, *Influence of Pt particle size and Re addition by catalytic reduction on aqueous phase reforming of glycerol for carbon-supported Pt (Re) catalysts.* Applied Catalysis B: Environmental, 2015. **174**: p. 126-135.

178. Wawrzetz, A., et al., *Towards understanding the bifunctional hydrodeoxygenation and aqueous phase reforming of glycerol.* Journal of Catalysis, 2010. **269**(2): p. 411-420.

179. Kalamaras, C.M., S. Americanou, and A.M. Efstathiou, *"Redox" vs "associative formate with–OH group regeneration" WGS reaction mechanism on Pt/CeO 2: Effect of platinum particle size.* Journal of Catalysis, 2011. **279**(2): p. 287-300.

180. Rasko, J., A. Hancz, and A. Erdőhelyi, *Surface species and gas phase products in steam reforming of ethanol on TiO 2 and Rh/TiO 2.* Applied Catalysis A: General, 2004. **269**(1): p. 13-25.

181. Jacobs, G., R.A. Keogh, and B.H. Davis, *Steam reforming of ethanol over Pt/ceria with co-fed hydrogen.* Journal of Catalysis, 2007. **245**(2): p. 326-337.

182. Guo, Y., et al., *Effect of support's basic properties on hydrogen production in aqueous-phase reforming of glycerol and correlation between WGS and APR.* Applied Energy, 2012. **92**: p. 218-223.

183. Chang, A.C.-C., et al., *Hydrogen production by aqueous-phase biomass reforming over carbon textile supported Pt–Ru bimetallic catalysts.* international journal of hydrogen energy, 2011. **36**(14): p. 8794-8799.

184. D'Angelo, M.N., et al., *Continuous hydrogen stripping during aqueous phase reforming of sorbitol in a washcoated microchannel reactor with a Pt–Ru bimetallic catalyst.* International Journal of Hydrogen Energy, 2014. **39**(31): p. 18069-18076.

Appendix

A. DFT calculations in Chapter 4*

A1. DFT calculations

All DFT calculations carried out in Chapter 4: Non-ideal Solvent Effect on Kinetics of Cyclohexene Hydrogenation over Pd/α-Al_2O_3 were conducted with the Vienna ab initio simulation package (VASP)[1, 2]. The GGA-PBE functional all-electron plane-wave basis sets with an energy cutoff of 400 eV was used for the exchange correlation energy[3]. The projector augmented wave (PAW) method were adopted to describe the electron-ion interactions[4].

The closed-packed 4x4 Pd (111) with four layers and 15 Å of vacuum separating the slabs in the z-direction were used to model the Pt catalyst. The top two metal layers were allowed to relax while the bottom two layers were fixed to the initial bulk positions. The Brillouin-zone was sampled by the 3×3×1 k-points using the Monkhorst-Pack scheme[5]. The convergence threshold was set 10^{-6} eV in total energy and 10^{-2} eV/Å in force on each atom. The energies of the adsorbates in vacuum were calculated in an 18x18x18 Å unit cell with the Γ only k-point mesh.

Transition state searches were performed using the dimer method [6] with the initial guesses for the transition state structure obtained through the nudged elastic band (NEB) method[7].

* DFT calculations were performed by Dr. Qiaohua Tan and Tong Mou

A2. Adsorption geometries

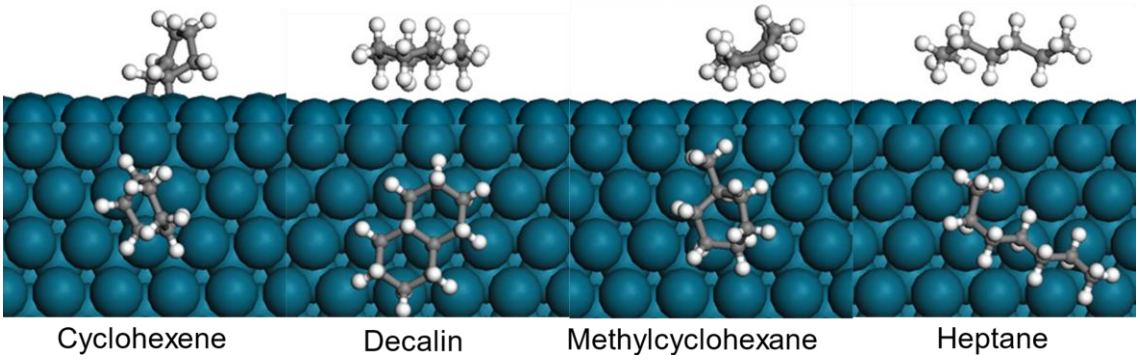

Figure A1. DFT optimized adsorption structure of cyclohexene, decalin, mythylcyclohexane and heptane.

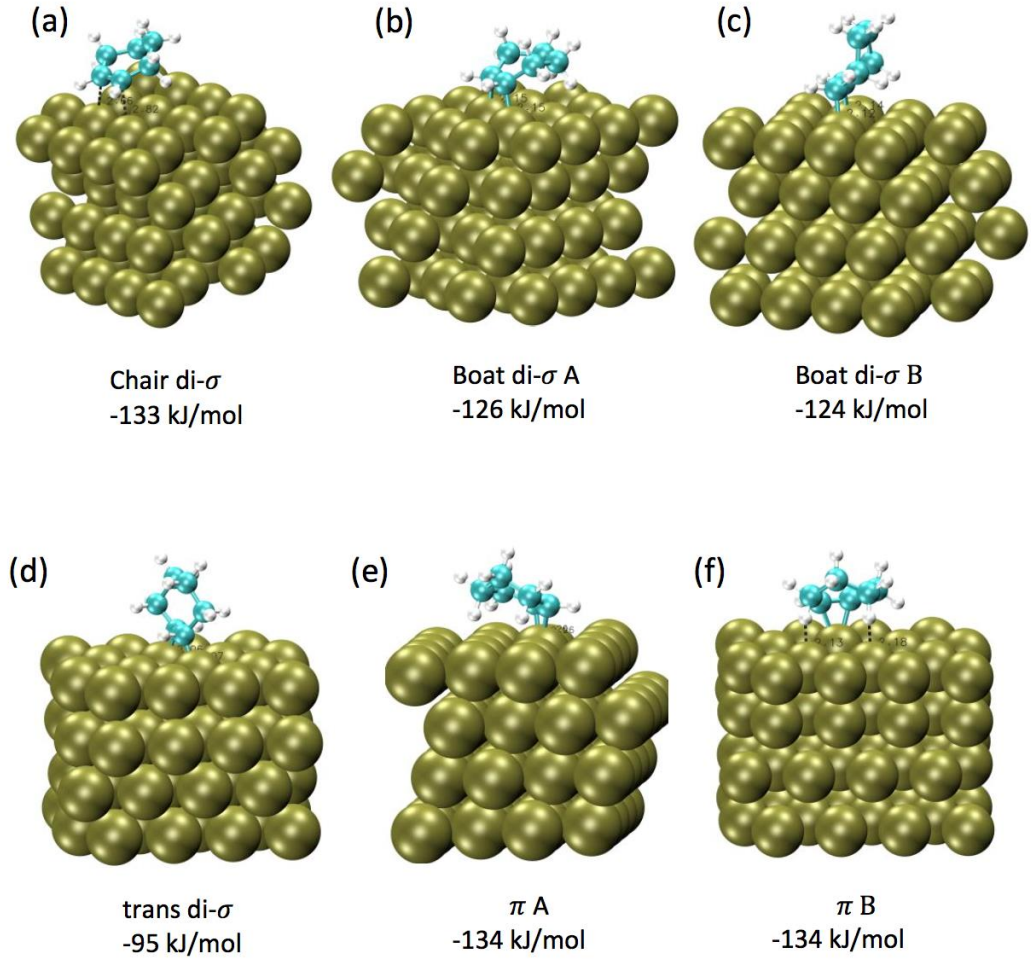

Figure A2. Adsorption geometries and energy of cyclohexene on clean Pd(111) surface with the consideration of vdw interactions.

B. Kinetic fitting effectiveness in Chapter 4

To acquire ΔS of adsorption/reaction, and ΔH of adsorption/reaction, more data for reaction rates were collected under different reaction temperature and reactant concentration, varying from 40 °C to 100 °C, 600 psi and 100 psi of H_2 pressures, 0.17 M and 0.42 M of cyclohexene in heptane. The experiment rates are compared with model rate using parameters from Table 10. As shown in Figure B 1, slope of those data is very close to 1, meaning a good fit of the model with experimental measurements.

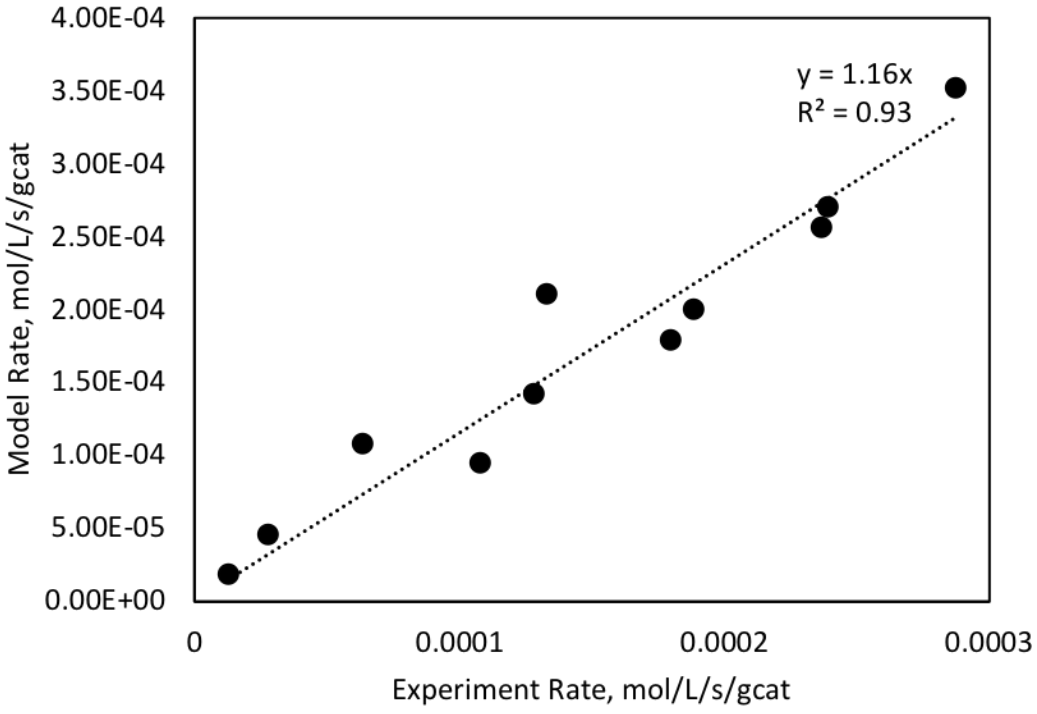

Figure B 1. Comparison between rates from experimental measurement and model prediction using parameters from Table 10.

C. DFT calculations in Chapter 5*

All DFT calculations performed in Chapter 5: Mechanistic Role of Water in Aqueous Phase Furfural Hydrogenation on Pd Catalysts was modeled using a (4×4) supercell on the Pd(111) surface. Each supercell contained repeated slabs with four metal layers separated by an 18 Å vacuum region. The bottom two layers of Pd have been fixed at their bulk positions while the top two layers were fully relaxed. A larger (6×6) supercell has been checked and no significant change has ben found. Number of water molecules was chosen to fill the vacuum region above the metal slab to make the density of water approximately the same as that of liquid water at the standard conditions.

The density functional theory (DFT) calculations and ab initio molecular dynamics (AIMD) simulations were carried out using the VASP package[8]. The Perdew-Burke-Ernzerhof generalized gradient approximation exchange-correlation potential (PBE-GGA)[3] was used, and the electron-core interactions were treated in the projector augmented wave (PAW) method [4, 9]. Structures have been optimized until the atomic forces were smaller than 0.02 eV $Å^{-1}$ with a kinetic cut off energy of 400 eV. The van der walls interactions were taken into account using DFT-D3 semi-empirical method[10]. Reaction pathways and the associated barriers were determined with the Nudged Elastic Band method[7, 11].

For simulations of the water-Pd(111) interface, AIMD simulations at finit temperatures (see below) were performed in canonical ensembles. The time step was set to

* DFT calculations were performed by Reda Bababrik and Dr. Wenhua Xue.

0.5 fs. The simulation time was typically 10 ps. After thermal equilibrium has been reached, multiple snapshots were taken and optimized for further DFT calculations.

D. Isotope study in Chapter 5

In order to experimentally observe the water assisted H-shuttling effect in Chapter 5: 5.3.3 Solvent effect, D_2O have been used as the solvent for furfural hydrogenation. Under same reaction conditions, 40 °C and 800 psi of H_2, the deuterated FOL was detected GC-MS. However, the H-D exchange reaction raises significant concerns since H can be exchanged into D through H-bonding network readily. The resulting deuterated FOL has to be differentiated whether it is produced via the shuttling effect or H/D exchange. Nevertheless, the isotope study fails to demonstrate the objectives. Here we provide analysis on regular furfuryl alcohol and deuterated furfuryl alcohol fragments from MS spectrum, as well as demonstrate that H-D reaches equilibrium instantly. Future isotope study should be conducted with caution.

To distinguish the reaction of furfural hydrogenation going through water shuttling mechanism from the observed H-D exchange reaction among furfuryl alcohol and D_2O mixture, furfuryl alcohol aqueous solution was prepared at room temperature in pure H_2O, pure D_2O and then analyzed by GC-MS right after the preparation. As shown in Figure D 1(A), deuterated furfuryl alcohol molecular ion, m/z = 99, appears in pure D_2O, indicating the H atom of hydroxyl group in furfuryl alcohol has been exchanged with D instantly after the introduction of D_2O under room temperature even without catalyst. –OH and D_2O form hydrogen bonding network that allows D atoms to exchange with H readily. Notably, the concentration of furfuryl alcohol was much lower than solvent D_2O. The H atoms are supposed to be replaced by D atoms completely, resulting the disappearance of furfuryl

alcohol molecular ion, which is m/z=98. On the contrary, the intensities of m/z=98 is as much as that of m/z=99 in pure D_2O after the exchange. The MS spectra indicate that both regular furfuryl alcohol and deuterated furfuryl alcohol exist in the mixture.

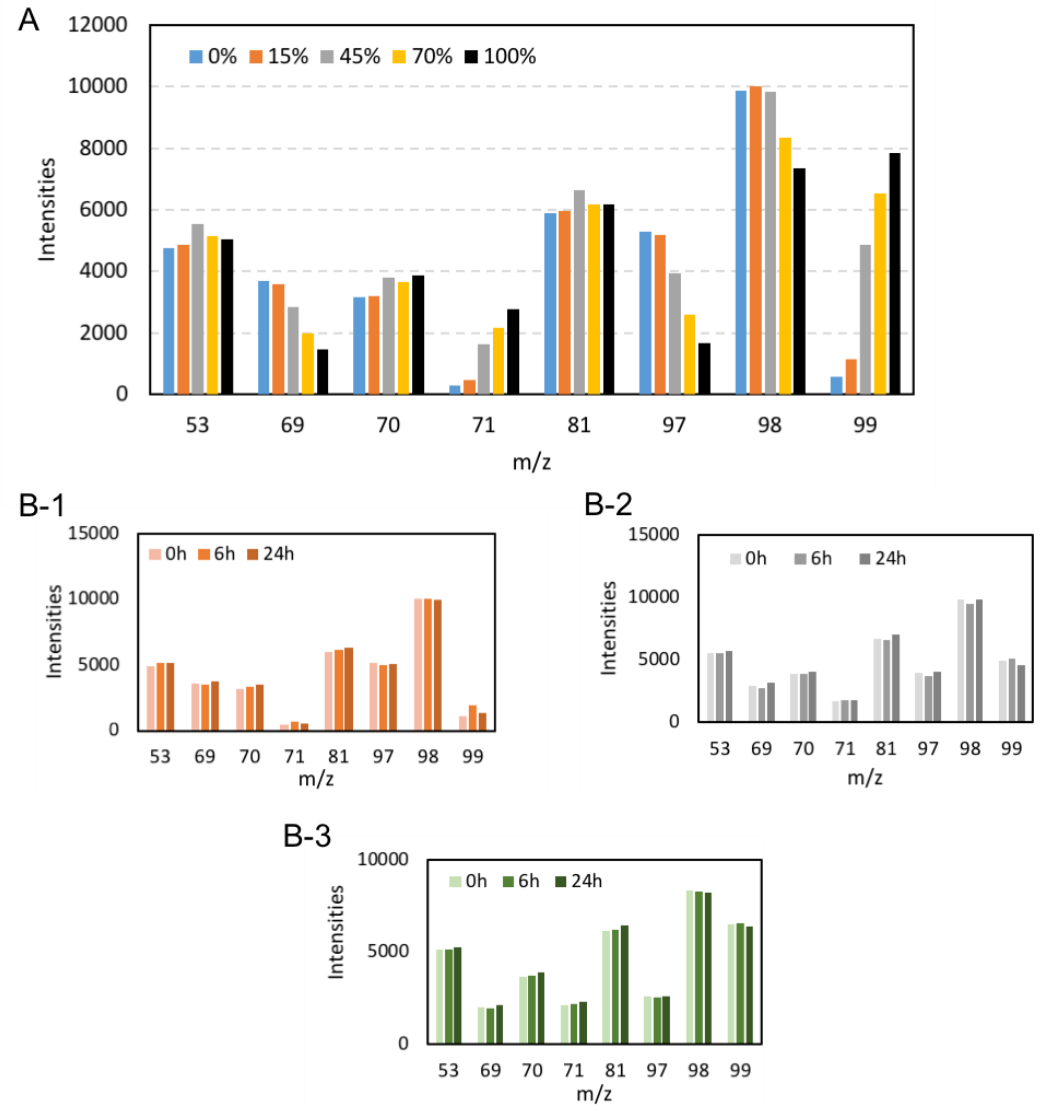

Figure D 1. (A) Mass spectroscopy of FOL in mixtures with different D_2O percentage: 0% represents pure H_2O and 100% represent pure D_2O. The FOL concentrations were 0.1 M for all prepared solutions under room temperature. (B-1,2,3) Mass spectroscopy of FOL in mixtures with different time intervals: from left to right under same m/z is the time increment. B-1 is FOL in 15% D_2O solution, B-2 is FOL in 45% D_2O solution and B-3 is FOL in 70% D_2O solution.

The H-D exchange reaction was then carried out with various amount of D_2O-H_2O mixture and at different time intervals. As D_2O volume percentage increases in the mixture presented in Figure D 1(A), m/z=69, 97 and 71, 99 decreases and increases respectively. Therefore, H-D exchange reaction illustrates an equilibrium with D_2O concentration. Higher percentage of D_2O yields more deuterated furfuryl alcohol in the mixture. To monitor the intensities evolution with time, the prepared solutions were later analyzed after 6 hours and 24 hours. However, the intensities as a function of time, plotted in Figure D 1 (B-1,2,3), remain constant for three mixtures. Therefore, the H-D exchange reaction happens drastically and reaches an equilibrium once furfuryl alcohol is mixed with D_2O.

Appendix References

1. Kresse, G. and J. Hafner, *Ab initio molecular dynamics for liquid metals.* Physical Review B, 1993. **47**(1): p. 558-561.

2. Kresse, G. and J. Hafner, *Ab initio molecular-dynamics simulation of the liquid-metal–amorphous-semiconductor transition in germanium.* Physical Review B, 1994. **49**(20): p. 14251-14269.

3. Perdew, J.P., K. Burke, and M. Ernzerhof, *Generalized Gradient Approximation Made Simple.* Physical Review Letters, 1996. **77**(18): p. 3865-3868.

4. Kresse, G. and D. Joubert, *From ultrasoft pseudopotentials to the projector augmented-wave method.* Physical Review B, 1999. **59**(3): p. 1758-1775.

5. Monkhorst, H.J. and J.D. Pack, *Special points for Brillouin-zone integrations.* Physical Review B, 1976. **13**(12): p. 5188-5192.

6. Henkelman, G. and H. Jónsson, *A dimer method for finding saddle points on high dimensional potential surfaces using only first derivatives.* The Journal of Chemical Physics, 1999. **111**(15): p. 7010-7022.

7. Henkelman, G. and H. Jónsson, *Improved tangent estimate in the nudged elastic band method for finding minimum energy paths and saddle points.* The Journal of Chemical Physics, 2000. **113**(22): p. 9978-9985.

8. Kresse, G. and J. Furthmuller, *Efficient iterative schemes for ab initio total-energy calculations using a plane-wave basis set.* Physical Review B, 1996. **54**(16): p. 11169-11186.

9. Blochl, P.E., *Projector Augmented-Wave Method.* Physical Review B, 1994. **50**(24): p. 17953-17979.

10. Grimme, S., et al., *A consistent and accurate ab initio parametrization of density functional dispersion correction (DFT-D) for the 94 elements H-Pu.* Journal of Chemical Physics, 2010. **132**(15).

11. Henkelman, G., B.P. Uberuaga, and H. Jonsson, *A climbing image nudged elastic band method for finding saddle points and minimum energy paths.* Journal of Chemical Physics, 2000. **113**(22): p. 9901-9904.